Multimodal Electron Microscopy of Mixed-Topology Solitons in Magnetic Thin Films

by

Jacques Reddinger

A dissertation accepted and approved in partial fulfillment of the

requirements for the degree of

Doctor of Philosophy

in Physics

Dissertation Committee:

Hailin Wang, Chair

Ben McMorran, Advisor

Jayson Paulose, Core Member

Leif Karlstrom, Institutional Representative

University of Oregon

Summer 2026

© 2026 Jacques Reddinger
This work is openly licensed via **CC BY 4.0**.



DISSERTATION ABSTRACT

Jacques Reddinger

Doctor of Philosophy in Physics

Title: Multimodal Electron Microscopy of Mixed-Topology Solitons in Magnetic Thin Films

Magnetic thin films host patterns in their magnetization whose structure and dynamics emerge from competition among exchange, anisotropy, Zeeman, interfacial, and dipolar energies. In Fe/Gd multilayers, this competition stabilizes room-temperature stripes and bubble domains with depth-varying structures. This dissertation combines Lorentz transmission electron microscopy (LTEM), scanning electron microscopy with polarization analysis (SEMPA), and micromagnetic simulation to probe these structures. LTEM measures thickness-projected in-plane magnetic induction, SEMPA maps surface vector magnetization, and simulation supplies complete three-dimensional magnetization. Together, these techniques form a model-informed, multimodal probe of the dynamics and depth-dependent structure of magnetic domains in Fe/Gd multilayers.

A LTEM survey identifies various magnetic phases consisting of parallel and labyrinthine stripes, and Type-I skyrmion, and Type-II trivial bubbles, and organizes their field-history-dependent transformations. Synthesis of LTEM and SEMPA domain ensembles support the twisted walls of dipole skyrmions and show that worm-domain observations are consistent with depth-dependent topologies. During parallel-stripe collapse, LTEM tracking reveals projected-induction signatures of candidate Type-III bubbles. Micromagnetic simulations identify a continuous pathway from Type-II bubbles to Type-I skyrmions through

a mixed-topology Type-III state with a Type-II-like interior and Type-I-like surface layers. Energy contribution analysis of these Type-III domains shows that the demagnetizing-energy reduction through surface closure competes against the high exchange energy cost at the partial-Bloch-line termini where the topology changes. Simultaneously, the Type-II-like interiors couple with the tilted Zeeman field. Depending on localized energetics, this competition selects a topological transition to Type-I or reversion to Type II.

In Fe/Gd multilayers containing Pt and Ir insertion layers, LTEM and SEMPA measurements of ensembles reveal complementary signatures consistent with antiskyrmions. Seeded simulations predict that thicker films relax into hybrid topologies with skyrmion-like surfaces and antiskyrmion-like interiors, whereas thinner films can retain depth-uniform antiskyrmions. Varying interfacial Dzyaloshinskii–Moriya interaction (DMI) shifts these depth-dependent boundaries. Balanced hybrid domains could reduce the thickness-integrated topological Hall response and the effective gyrovector that drives transverse motion.

Together, these results establish Fe/Gd as a tunable platform for mixed-topology solitons and show that depth-aware imaging and simulation informs advances in materials engineering.

This dissertation includes previously published, unpublished, and coauthored material.

CURRICULUM VITAE

NAME OF AUTHOR: Jacques Reddinger

GRADUATE AND UNDERGRADUATE SCHOOLS ATTENDED:

University of Oregon, Eugene, OR, USA
University of Maryland, College Park, MD, USA

DEGREES AWARDED:

Doctor of Philosophy, Physics, 2026, University of Oregon
Bachelor of Science, Physics, 2020, University of Maryland

AREAS OF SPECIAL INTEREST:

Electron Microscopy
Magnetic Materials
Micromagnetic Simulation

PROFESSIONAL EXPERIENCE:

Graduate Teaching Assistant, University of Oregon, 2020-2022
Physics Demonstration Room Assistant, University of Oregon, 2021-2022
Graduate Research Assistant, University of Oregon, 2023-2026
Science Graduate Student Researcher (DOE-SCGSR), Lawrence Berkeley National Laboratory, 2026

GRANTS, AWARDS AND HONORS:

Weiser Teaching Award, University of Oregon, 2022
Poster Award, Microscopy and Microanalysis, 2022
Travel Award, Microscopy and Microanalysis, 2025
Science Graduate Student Research Award, Department of Energy, 2025

PUBLICATIONS:

Parker, W. S., **Reddinger, J. A.**, Moraski, R., Fullerton, E.E., Montoya, S. A., & McMorran, B. J. (2024). Real space imaging of dipole-stabilized hybrid skyrmions in magnetic multilayer thin films. Physical Review B, 112(9), 094415.

Parker, W. S., **Reddinger, J. A.**, & McMorran, B. J. (2024). Hybrid skyrmions in magnetic multilayer thin films are half-integer hopfions. Physical Review B, 110(22), 224420.

Reddinger, J. A., Parker, W. S., Fullerton, E.E., Montoya, S. A., & McMorran, B. J. (2026). Experimental Evidence for Mixed-Topology Bubbles Mediating Dipole Skyrmion Formation in Fe/Gd Multilayers. Manuscript in preparation.

ACKNOWLEDGEMENTS

Many thanks to the various different people and organizations that made this dissertation possible. I thank Professor Ben McMorran for the support and direction and Eric Fullerton and Sergio Montoya for their magnetism expertise. I thank past McMorran group members Rich Moraski and Will Parker for their valuable introduction into electron microscopy and magnetism.

Work at the Molecular Foundry was supported by the Office of Science, Office of Basic Energy Sciences, of the U.S. Department of Energy under Contract No. DE-AC02-05CH11231, under user proposal No. MFP-10439. This work was also supported by the National Science Foundation under Grant No. 2105400 and by the Department of Energy Science Graduate Student Research program. The author acknowledges Research Advanced Computing Services (RACS) at the University of Oregon for providing computing resources that have contributed to the research results reported within this publication.

To my family, who always encouraged my questions, and to my friends, who kept me sane through graduate school.

TABLE OF CONTENTS

Chapter Page

I. INTRODUCTION 16
1.1. Moore's Law 16
1.2. A Return to Magnetic Media 17
1.3. Why Multimodal Electron Microscopy is Needed 19
1.4. Outline 20
1.5. Author Contributions 21
II. BACKGROUND 23
2.1. Origins of Magnetism 23
2.1.1. Bloch's Theorem and Electronic Band Structure 23
2.1.2. Ferromagnetism 24
2.1.3. Antiferromagnetism 26
2.1.4. Ferrimagnetism 26
2.1.5. Paramagnetism 27
2.2. Energetics in Magnetic Materials 27
2.2.1. Saturation Magnetization 28
2.2.2. Exchange energy 29
2.2.3. Anisotropy energy 29
2.2.4. Zeeman energy 30
2.2.5. Demagnetizing energy 31
2.2.6. Dzyaloshinskii-Moriya Interaction (DMI) 32
2.2.7. Characteristic lengths 32
2.2.7.1. Exchange length 32

Chapter Page

2.2.7.2. Domain wall width 32

2.2.8. Temperature effects 33

2.3. Landau-Lifshitz-Gilbert Equation and the Effective Field 33

2.4. Anatomy of Magnetic Domains 34

2.5. Current driven dynamics 38

2.5.1. The Thiele equation 39

2.5.2. Skyrmion Hall Effect (SkHE) and Topological charge 39

2.6. The Fe/Gd System 41

2.6.1. Fe/Gd bilayers 41

2.6.2. Fe/Gd multilayers 42

2.6.3. Existing characterization of Fe/Gd multilayers 43

2.6.4. Three-dimensional magnetic domains 45

2.6.5. Bloch points in Fe/Gd multilayers 46

2.6.6. Heavy metal interfaces 47

III. METHODS 48

3.1. Experimental Methods 48

3.1.1. Lorentz Transmission Electron Microscopy (LTEM) 48

3.1.2. Scanning Electron Microscopy with Polarization Analysis (SEMPA) 51

3.2. Computational Methods 52

3.2.1. Micromagnetic Simulation 52

3.2.2. Domain Tracker 53

IV. THE ZOO OF DOMAINS IN FE/GD MULTILAYERS 55

Publication and Contribution Note 55

4.1. Role of this Chapter 55

4.2. Why a Domain Zoo is Needed 57

Chapter Page

4.3. Stripe Domains 59
4.4. Worm Domains 62
4.5. Type-II Bubbles 64
4.6. Type-I Dipole Skyrmions 65
4.7. Field-History Pathways Through the Domain Zoo 70
4.8. Imaging Signatures and Three-Dimensional Structure 73
4.8.1. What LTEM Contributes 73
4.8.2. What SEMPA Adds 73
4.8.3. The Paired-Imaging Logic 74
4.9. Using the Zoo in the Following Chapters 74
4.10. Summary 75
V. STRIPE COLLAPSE IN FE/GD MULTILAYERS 77
Publication Note 77
Abstract 78
5.1. Introduction 79
5.2. Background 80
5.3. Methods 83
5.3.1. Experimental Methods 83
5.3.2. Computational Methods 85
5.4. Results 86
5.4.1. Experimental signatures of candidate mixed-topology bubbles 86
5.4.2. Projected-induction comparison with simulations 89
5.4.3. Simulated stripe collapse nucleates frustrated Type-II bubbles 94
5.4.4. Type-III bubbles mediate topology change 97

Chapter Page

5.4.5. Energetic signatures of the relaxation pathways 99

5.5. Discussion 102

5.6. Conclusion 104

Acknowledgments 105

VI. ANTISKYRMIONS IN FE/GD MULTILAYERS 106

6.1. Motivation: Antiskyrmions and Interface Engineering 106

6.2. Experimental Observation of Antiskyrmions 107

6.2.1. LTEM Signatures 107

6.2.2. Antiskyrmion Formation Process 108

6.2.3. SEMPA Surface Magnetization 108

6.3. Simulation-Supported Three-Dimensional Structure 113

6.3.1. Hybrid Antiskyrmions and Depth-Dependent Topology . . . 118

6.3.2. Transport Implications of Hybrid Topology 122

6.4. Outlook: Heavy-Metal Interfaces and DMI 122

6.5. Conclusion 124

VII. CONCLUSION 125

7.1. A Model-Informed Multimodal Probe 125

7.2. Depth-Dependent Topology 126

7.3. Type-III Relaxation During Stripe Collapse 127

7.4. Future Work 128

LIST OF FIGURES

Figure Page

1. Stoner model of itinerant ferromagnetism 26
2. Common magnetic order types 27
3. Micromagnetic energy terms 28
4. Domain-wall and skyrmion helicity 35
5. Bloch-line schematic 36
6. Current-driven skyrmion Hall motion 40
7. LTEM magnetic contrast 50
8. SITIE workflow for LTEM data 51
9. SEMPA microscope schematic 52
10. Domain Tracker analysis workflow 54
11. Representative Fe/Gd domain phases 57
12. Local Fe/Gd domain signatures 59
13. Wall chirality in LTEM and SEMPA domain images 63
14. LTEM, SEMPA, and simulation signatures of hybrid skyrmions 68
15. Layer-dependent helicity of simulated hybrid skyrmions 69
16. Field-history graph for Fe/Gd domain states 71
17. Bubble topology in Fe/Gd multilayers 82
18. LTEM evidence for mixed-topology bubbles 88
19. Projected induction signatures in experiment and simulation 90
20. Properties of Type-II and candidate Type-III bubbles 93
21. Simulated stripe-collapse pathways 96
22. Depth-resolved Bloch-line dynamics 98

Figure Page

23. Depth-dependent bubble energetics 101

24. LTEM signatures of antiskyrmions 109

25. Field evolution of antiskyrmion formation 110

26. SEMPA magnetometry of antiskyrmions 112

27. Seeded antiskyrmion basin stability 114

28. DMI-thickness final-state map for a seeded antiskyrmion 117

29. DMI- and thickness-dependent layer topology 119

30. Energy-depth decomposition of a 120-nm hybrid antiskyrmion 120

31. Representative simulated domain-wall surfaces 121

LIST OF TABLES

Table Page

1. Soliton configurations and terminology 38

2. Fe/Gd material parameters and characteristic lengths 43

3. Experimental and computational methods 49

4. Classification tips for Fe/Gd domains 60

CHAPTER I

INTRODUCTION

1.1 Moore's Law

Magnetic materials helped lay the foundation for the current "information age". Magnetic wire, drum, and core memories were important steps in computer engineering through the mid-20th century. These devices used magnetic domains, regions with uniform magnetic dipole moment density, as bits. Advances in magnetic materials increased the information density and processing speed of magnetic computer components while keeping them inexpensive and relatively easy to manufacture.

In the 1960s, Bell Labs developed the metal-oxide-semiconductor field-effect transistor (MOSFET). Since then, transistor density, and therefore bit density, has grown exponentially as described by Moore's Law. This growth produced a technological explosion in semiconductor devices, with transistors supplanting magnetic domains as the *lingua franca* of working memory. Magnetic materials have nevertheless remained viable for data storage; hard disk drives have continually improved since the 1980s. More recently, solid-state drives have challenged magnetic media in consumer and high-performance applications by offering faster access times, higher information density, and improving reliability and affordability. In the last half century, computer engineering has therefore shifted from magnetic-domain-based working memory toward transistor-based devices, while magnetic media have remained important for storage.

However, exponential growth in semiconductor performance is projected to be nearing its limit. Industry roadmaps increasingly frame post-CMOS and beyond-Moore technologies as necessary responses to the slowing benefits of

conventional dimensional scaling [1]. At the same time, AI-driven data-center growth has sharpened the energy-cost side of the problem. The Department of Energy's 2024 report estimates that U.S. data centers used 176 TWh in 2023 (4.4% of total U.S. electricity consumption) and projects 325–580 TWh (6.7–12%) by 2028 [2]. Rising demand for computing power strengthens the case for memory and logic devices that can store, move, and process information with lower energy cost. While they may not single-handedly solve this looming infrastructure problem, magnetic devices are well positioned to mitigate its impact.

1.2 A Return to Magnetic Media

Parkin et al. [3] developed a "Racetrack Memory" architecture that uses current pulses to shift trains of magnetic domains past read and write heads. This design removes the need for a spinning disk, reducing mechanical complexity and energy consumption. It also enables a three-dimensional magnetic memory device with exceptional bit density. In principle, bits in such a device would have improved density, stability, and energy efficiency. Early prototypes faced fabrication and materials challenges, but advances in condensed matter physics, thin-film growth, nanofabrication, and magnetic characterization have brought the field closer to practical devices.

Mühlbauer et al. [4] reported a lattice of nanoscopic circular magnetic domains with a whirling domain wall in MnSi. Yu et al. [5] later confirmed the structure of this domain using Lorentz transmission electron microscopy (LTEM). The spin texture observed in MnSi matched the two-dimensional topological structure introduced by Tony Skyrme in a model of mesons and baryons, and is therefore referred to as a magnetic skyrmion [6]. Its significance is not simply that it is small or circular, but that its magnetization wraps the unit sphere.

Such a topology cannot be smoothly deformed without passing through a high-energy singular configuration or destroying the surrounding magnetic order. This topological characteristic gives skyrmions enhanced stability and favorable transport properties [7–10]. Consequently, they are comparatively robust against thermal fluctuations and stray fields, and they can move at lower current densities than many conventional domain-wall objects. This makes the skyrmion an ideal candidate for the magnetic domain stored in a racetrack memory device.

The search for the ideal racetrack material has resulted in a wide variety of skyrmion-hosting materials and extensive exploration of their behavior [9, 11]. These materials can be broadly categorized by the interaction that stabilizes the skyrmion texture. MnSi belongs to the class of bulk chiral magnets, where broken crystal inversion symmetry produces a bulk Dzyaloshinskii-Moriya interaction (DMI) and stabilizes Bloch-type skyrmions [4, 12]. Certain multilayer stacks instead introduce interfacial DMI, which stabilizes Néel-type skyrmions [13, 14]. Other multilayer stacks do not feature significant DMI and instead rely on competition between short-range exchange and the long-range dipolar field. The resulting textures are often referred to as hybrid skyrmions because they feature Néel- and Bloch-like regions through their depth [15–17]. Such a structure introduces ambiguity in projective measurements like LTEM. The capability of multilayer stacks to host depth-varying structures motivates much of the work in this dissertation. Although other stabilizing mechanisms exist, most skyrmion-hosting materials fall into these categories.

Beyond their use as racetrack memory, skyrmion materials have been investigated for neuromorphic devices [9, 18, 19]. Neuromorphic computation does not depend on the historically dominant digital computing architecture. Instead,

these devices rely on the physical constraints of the system, magnetic domains and energies in this case, to process information directly. An input signal excites a network of magnetic domains electrically or magnetically, and the system's response is used as the output. This architecture is analogous to neural-network computation in machine learning [19, 20]. In the future, trained network functions could be written directly to skyrmion-hosting films, reducing overhead by offloading computational effort into the material itself.

1.3 Why Multimodal Electron Microscopy is Needed

The developmental history of skyrmion hosting materials makes the central methodological problem clear. The first real-space confirmation of the skyrmion relied on Lorentz TEM because the texture of interest was nanoscale, magnetic, and field dependent [5]. Since then, LTEM has remained one of the most useful tools for following skyrmion formation and domain evolution in thin specimens because it can image magnetic contrast over mesoscopic fields of view while external field and temperature are varied. However, LTEM records a projection of the magnetic induction along the electron-beam direction ($\mathbf{B}_{\perp}^{\mathrm{proj}}$). It is powerful precisely because it compresses a three-dimensional magnetic object into an experimentally accessible image, but that same projection can make distinct three-dimensional textures appear deceptively similar.

This limitation is especially important in Fe/Gd multilayers. These films are thick enough for long-range dipolar fields to twist the domain wall through the film thickness, producing Bloch-like interiors and more Néel-like surface closure domains [16, 17, 21]. A single projected image can therefore show the outline and projected circulation of a domain without uniquely determining the full magnetization. In Fe/Gd, textures with different layer-resolved topology can produce related LTEM

signatures, making it difficult to distinguish a skyrmion from a trivial bubble, a mixed-topology bubble, or an antiskyrmion-like texture from projection alone.

The supplementary methods used in this work address this limitation of LTEM: scanning electron microscopy with polarization analysis (SEMPA) supplies a complementary surface boundary condition by measuring surface vector magnetization ($\mathbf{M}$), and micromagnetic simulation provides the depth-resolved magnetization and energy density needed to connect the projected LTEM signal to the underlying topology. Together, these components form a model-informed multimodal probe of three-dimensional structure. Here, "model informed" is important. The experimental measurements constrain the surface and thickness projection, while micromagnetics can be directly compared to experiment by simulating LTEM and SEMPA images. Together, these methods turn the dissertation from a study of isolated magnetic images into a multimodal characterization program for identifying three-dimensional magnetic textures and their properties.

1.4 Outline

The promise of the magnetic skyrmion has resulted in a broad research effort enabled by a well-developed theory of magnetism (Ch. II) and highly specialized electron microscopy techniques (Ch. III). The central methodological contribution of this dissertation is the application of a model-informed multimodal probe of three-dimensional structure in Fe/Gd multilayer thin films. Ch. IV introduces the wide variety of magnetic phases and constituent bubble and stripe domains in amorphous Fe/Gd multilayers and discusses their structure and properties. Ch. V introduces evidence of Type-III bubbles in Fe/Gd and investigates their role in the formation process of dipole skyrmions during parallel

stripe collapse. The central physical result of this dissertation is a transition pathway from Type-II bubbles to Type-I dipole skyrmions mediated by a mixed-topology Type-III state, with depth-localized topological defects at partial-Bloch-line termini. Ch. VI collects simulation, SEMPA, and LTEM results on antiskyrmions in Fe/Gd multilayers with heavy-metal interface engineering and develops the outlook for a antiskyrmion-hosting system.

1.5 Author Contributions

This dissertation is based on electron microscopy techniques developed over decades. The application of complementary electron microscopy techniques has been an ongoing goal of the McMorran group. We study Fe/Gd samples provided by Eric Fullerton and Sergio Montoya at University of California San Diego's Center for Magnetic Memory and Recording. Several datasets analyzed in this dissertation were acquired prior to the author's involvement in the project. For the study of the three-dimensional structure of magnetic textures in Fe/Gd multilayers (Ch. IV and Ch. VI), some LTEM and SEMPA measurements were collected by previous group members Will Parker, Rich Moraski, and Jordan Chess, and collaborators from NIST.

For the investigation of stripe collapse and skyrmion nucleation in Fe/Gd multilayers (Ch. V), the author performed the LTEM experiments and carried out the associated micromagnetic simulations and data analysis. Fe/Gd samples were provided by Fullerton and Montoya. The author's work also included the development of new domain-tracking software used to analyze the evolution of magnetic domains (**domain-tracker on GitHub**).

For the investigation of antiskyrmions in Fe/Gd multilayers (Ch. VI), the author identified and analyzed antiskyrmion textures. For the study of a depth-

dependent hybrid-skyrmion-antiskyrmion structure and its implications for the emergent topological Hall effect, the author performed all work.

CHAPTER II

BACKGROUND

2.1 Origins of Magnetism

Classical statistical physics fails to account for spontaneous magnetization. In 1911 and 1919, respectively, Niels Bohr and Hendrika Johanna van Leeuwen showed that classical statistical mechanics predicts exactly zero magnetization at thermal equilibrium (the Bohr–van Leeuwen theorem). This result proved that ferromagnetism cannot be explained by purely classical physics [22]. This deficiency in classical mechanics was remedied by the emergence of quantum physics in the 1910s and 1920s. The key insight was that subatomic particles have an intrinsic magnetic moment arising from their angular momentum. In an isolated atom, the spin and orbital magnetic moments of the electron dominate the magnetic response. As a result, the magnetic behavior of a free atom is determined by its electron shell occupation and the associated spin and orbital quantum numbers. However, this free atom picture is insufficient for solids. When atoms bond, their electronic wavefunctions overlap. The Pauli exclusion principle lifts the atomic degeneracies, splitting them into a dense cluster of energy levels. In the many-body solid, these closely spaced levels merge into continuous energy bands, which are described using various band-structure approximations.

2.1.1 Bloch's Theorem and Electronic Band Structure. Bloch's theorem provides the fundamental framework to describe electron states in a periodic potential, such as a crystal lattice [23, 24]. It begins with the ansatz that the wavefunction of an electron in a periodic potential can be written as a plane wave modulated by a function matching the periodicity of the lattice:

$$\psi(\mathbf{r}) = e^{i\mathbf{k}\cdot\mathbf{r}} u(\mathbf{r}) \tag{2.1}$$

where $\mathbf{r}$ is the position vector and $\mathbf{k}$ is the crystal momentum. Because of translational symmetry, $\mathbf{k}$ is a conserved quasi-momentum; it differs from the canonical momentum but determines the group velocity of the electron wave packet.

Consequently, the allowed electron energies become continuous functions of $\mathbf{k}$, known as energy bands, $E_n(\mathbf{k})$. These bands originate from the combination and splitting of atomic orbitals due to the periodic potential of the lattice, recovering the expected behavior of a many-body system. These band structures determine how electrons propagate in different materials. Electrons in completely filled bands do not contribute to charge transport, while partially filled bands dominate the electrical, magnetic, and thermal response of metals. In this way, the crystal momentum provides the quantum number needed to describe both the occupancy and dynamics of electrons, setting the stage for ferromagnetism.

2.1.2 Ferromagnetism. Ferromagnetism arises from the exchange interaction, a quantum mechanical effect originating from the indistinguishability of electrons and the Pauli exclusion principle. Because electrons are fermions, the total many-electron wavefunction must be antisymmetric under particle exchange. This antisymmetry requirement can be met by either antisymmetric spatial and symmetric spin states or vice versa. These two configurations lead to different expectation values of the electron-electron distance. Coulomb repulsion causes energy splitting between otherwise degenerate parallel- and antiparallel-spin configurations. This energy difference between spin alignments is called the exchange energy. In the Heisenberg formalism, ferromagnetism emerges when localized spins prefer to align due to a positive exchange energy, J_{ex}. Gd has a half-filled $4f$ shell that is highly localized and orders ferromagnetically below its

Curie temperature $T_C \approx 293\,\mathrm{K}$. However, this localized-spin treatment breaks down when the electrons responsible for magnetism are delocalized. In this case, ferromagnetism is better understood using the framework of electronic bands.

In the itinerant (delocalized) electron picture, bands split into majority and minority branches with opposite spin, as shown schematically in Fig. 1. This behavior lowers the exchange energy because electrons with parallel spins avoid each other more effectively. However, transferring electrons from one spin band to the other forces some electrons to higher energy $\mathbf{k}$ states. Ferromagnetism occurs when the exchange energy gain exceeds this increase in the band's kinetic energy. This competition is modeled by the Stoner criterion for itinerant ferromagnetism [24–26]. If the product of the exchange interaction parameter I and the electronic density of states at the Fermi level $D(E_F)$ satisfies the Stoner criterion:

$$I \cdot D(E_F) > 1 \tag{2.2}$$

the system lowers its energy by developing a spontaneous spin polarization. Thus, materials with a high density of states near the Fermi level and sufficiently strong exchange interactions are prone to ferromagnetism. Iron, cobalt, and nickel are the canonical 3d itinerant ferromagnets. In bcc Fe, the broad $3d$ bands cross the Fermi level and exchange-split into majority and minority branches; in ultrathin films and at interfaces, reduced coordination can narrow bands and enhance local moments relative to bulk Fe [27, 28]. Gd represents the complementary rare-earth limit relevant to this dissertation: the $4f$ shell carries a nearly atomic local moment, while the more itinerant $5d/6s$ states mediate exchange and provide the bands probed by photoemission and spin-polarized reflectivity [29, 30]. Depending on the nature and sign of the interactions between moments or sublattices, other forms of magnetic order can occur.

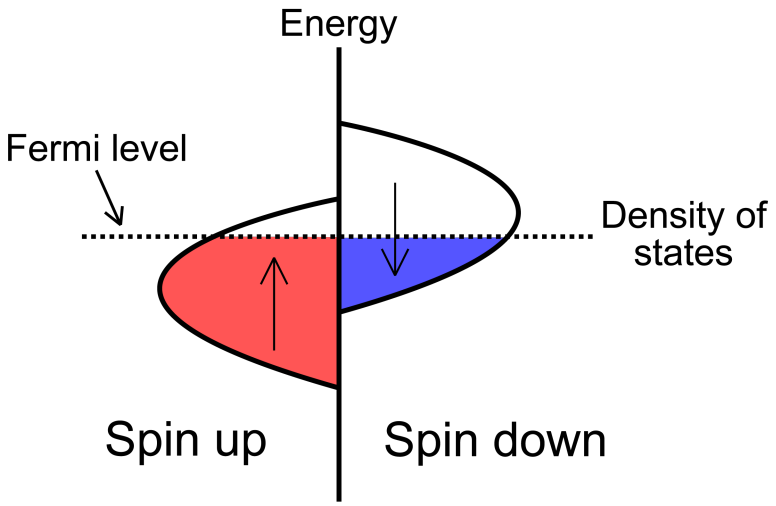

Figure 1. Stoner model of itinerant ferromagnetism. A ferromagnetic state features an exchange splitting between the two spin bands. Ferromagnetism is favored when the exchange-energy gain from spin polarization exceeds the kinetic-energy cost of redistributing electrons between the bands. Figure adapted from A13ean, own work, CC BY-SA 3.0, via Wikimedia Commons (curid: 16209709).

2.1.3 Antiferromagnetism. In antiferromagnets, neighboring magnetic moments align antiparallel, resulting in vanishing net magnetization. For localized systems, antiferromagnetism occurs when the exchange interaction favors antiparallel alignment. For itinerant systems, antiferromagnetism can arise from instabilities of the electronic structure, leading to a spin-density wave in which the spin polarization varies periodically in space. Despite the different microscopic origins, both cases produce alternating spin orientations and no macroscopic moment.

2.1.4 Ferrimagnetism. Ferrimagnetism occurs when magnetic moments on different sublattices align antiparallel but have unequal magnitudes, producing a nonzero net magnetization. This commonly occurs in sublattices with different atomic species, electronic configurations, or densities of states.

Ferrimagnetism may originate from localized moments or from unequal spin polarization of different bands or sublattices in delocalized systems. Many rare-earth/transition-metal alloys, particularly Fe/Gd multilayers, exhibit ferrimagnetic behavior between localized and delocalized regions.

2.1.5 Paramagnetism. Paramagnetism occurs when the exchange interaction is insufficient to produce spontaneous order. In itinerant systems, this corresponds to failure of the Stoner criterion, while localized systems behave as weakly interacting magnetic moments.

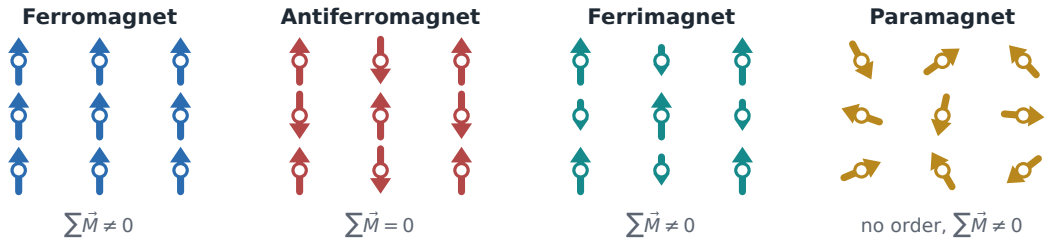

Figure 2. Schematic comparison of common magnetic order types. Ferromagnetic and ferrimagnetic configurations have a nonzero net magnetization, antiferromagnetic order cancels across sublattices, and paramagnetism lacks long-range order.

2.2 Energetics in Magnetic Materials

Although the exchange interaction is the primary driving mechanism behind ferro-, antiferro-, and ferrimagnetism, other energy terms greatly impact the magnetization of real systems.

$$E = E_{\text{exch}} + E_{\text{anis}} + E_{\text{Zeeman}} + E_{\text{demag}} + E_{\text{DMI}} \tag{2.3}$$

These contributions come from a wide variety of physical phenomena and thus have unique conditions for energy minimization. While most of these contributions have material-specific parameters and a large parameter space, their impact can be generalized within the micromagnetic framework [31].

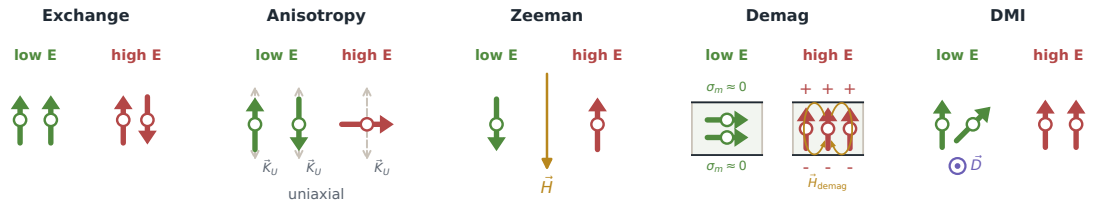

Figure 3. Low- and high-energy schematic configurations for the micromagnetic energy terms used throughout this dissertation: exchange, anisotropy, Zeeman, demagnetizing, and Dzyaloshinskii-Moriya energies.

2.2.1 Saturation Magnetization.

The magnitude of the magnetization describes the average magnetic moment per unit volume. However, as the magnetization in most materials will not be perfectly uniform, the magnitude of the magnetization vector is poorly defined and varies under different excitations. As such, the magnitude of the magnetization is often set by the saturation magnetization, M_s. This value is defined by the average magnetic moment density of the material under high magnetic fields (saturation), where the magnetization is expected to be as uniform as possible.

In the continuum model of micromagnetics, the magnetization is treated as a smoothly varying vector field [31]:

$$\mathbf{M} = M_s\mathbf{m} = M_s(m_x\hat{x} + m_y\hat{y} + m_z\hat{z}) \tag{2.4}$$

where M_s is the saturation magnetization and $\mathbf{m}$ is the reduced magnetization vector ($|\mathbf{m}| = 1$).

This approximation is valid when the characteristic magnetic length scales (see Secs. 2.2.7.1 and 2.2.7.2) are much larger than the atomic spacing. It therefore applies to most ferromagnetic and ferrimagnetic textures but breaks down where atomistic or sublattice-resolved physics becomes essential. In Fe/Gd multilayers, we use measured effective material parameters and treat the system as a single

effective continuum ferromagnet. This description is sufficient for most simulated magnetic structures, but it does not fully describe the atomic-scale core of a Bloch point (see 2.4), where the magnetization direction becomes singular and the fixed-magnitude approximation fails. In a discretized micromagnetic simulation, finite cell size smears out this core and generally underestimates the exchange energy associated with Bloch-point formation [32]. The implications of this result is discussed further in Sec. 2.6.5.

2.2.2 Exchange energy. As discussed in 2.1.2, the exchange energy is a manifestation of the Pauli exclusion principle and dominates the short-range magnetic order. In ferromagnets, where the exchange energy is negative, the local magnetization aligns parallel and manifests smooth, slowly varying magnetizations. In antiferromagnets, where the exchange energy is positive, the local magnetization aligns anti-parallel and manifests alternating, highly varying magnetizations. Here, the exchange energy is related to the magnetization by:

$$E_{\text{exch}} = A_{\text{ex}} \int_V dV \left(|\nabla m_x|^2 + |\nabla m_y|^2 + |\nabla m_z|^2 \right) \tag{2.5}$$

where A_{ex} is the exchange stiffness constant. This scales with the exchange constant, J_{ex}, and depends on the structure of the material. In a ferromagnet, and in the sublattices of ferri- and antiferromagnets, the exchange energy prefers a uniform magnetization.

2.2.3 Anisotropy energy. The magnetic anisotropy energy encapsulates material phenomena that result in energetically preferable directions (easy axes) for the orientation of the magnetic moment. Sources of anisotropies relevant to the Fe/Gd system include:

– Magneto-crystalline anisotropy: Arises from spin–orbit coupling, which links the electronic orbital structure to the crystal symmetry. The crystal structure

also introduces anisotropic coupling between magnetic moments, but this effect is weaker.

– Interfacial anisotropy: Coupling between interfaces in multilayer systems introduces an energetically preferable spin orientation.

Shape anisotropy arises from the geometry-dependent demagnetizing field and is therefore included in the demagnetizing-energy term below rather than in E_{anis}. In the continuum model, the energy associated with anisotropy is represented by:

$$E_{\text{anis}} = \int_V dV\, f_{\text{anis}}(\mathbf{m}) \tag{2.6}$$

where f_{anis} is the anisotropy energy density and depends on the orientation of the magnetization. The minima and maxima of the f_{anis} surface correspond to easy and hard magnetic axes. By defining preferred magnetization orientations, easy axes greatly influence the resulting structure of domains in magnets. In multilayer thin films, the easy axis is primarily uniaxial and normal to the plane of the film (perpendicular):

$$E_{\text{anis}} = -K_U \int_V dV\, (\mathbf{m} \cdot \hat{z})^2 \tag{2.7}$$

Where, K_U is the uniaxial anisotropy constant. The relative strength of the perpendicular magnetic anisotropy (PMA) determines whether its domains are in-plane or out-of-plane. The anisotropy energy also contributes to the stiffness and dynamics of domain walls.

2.2.4 Zeeman energy. The Zeeman energy describes the potential energy of a magnetized volume in an external magnetic field. This potential is minimized when the magnetization aligns parallel with the external magnetic field and is maximized when it aligns anti-parallel. Magnetic hysteresis loops rely on this effect to determine various other magnetic properties of a material by analyzing

the magnetization response. The Zeeman energy is the primary mechanism used for exciting and probing magnetic materials. In the continuum model, the Zeeman energy is simply:

$$E_{\text{Zeeman}} = -\mu_0 M_s \int dV \mathbf{m} \cdot \mathbf{H}_{\text{ext}} \tag{2.8}$$

where μ_0 is the vacuum permeability and H_{ext} is the external magnetic field.

2.2.5 Demagnetizing energy. Each magnetic moment generates a dipolar field that interacts with other moments, giving rise to the long-range demagnetizing energy. In the continuum model, this energy is:

$$E_{\text{demag}} = -\frac{\mu_0}{2} M_s \int dV \mathbf{m} \cdot \mathbf{H}_{\text{demag}} \tag{2.9}$$

where $\mathbf{H}_{\text{demag}}$ is the demagnetizing field. This field can be expressed as the gradient of a scalar potential, $\mathbf{H}_{\text{demag}} = -\nabla U$, which originates from surface and volume magnetic charges:

$$U(\mathbf{r}) = \frac{M_s}{4\pi} \left[-\int_V \frac{\nabla' \cdot \mathbf{m}(\mathbf{r}')}{|\mathbf{r} - \mathbf{r}'|} \, dV' + \oint_{\partial V} \frac{\hat{\mathbf{n}}' \cdot \mathbf{m}(\mathbf{r}')}{|\mathbf{r} - \mathbf{r}'|} \, dS' \right]. \tag{2.10}$$

Here, $\rho_m(\mathbf{r}') = -\nabla' \cdot \mathbf{m}(\mathbf{r}')$ is the volume magnetic charge density and $\sigma_m(\mathbf{r}') = \hat{\mathbf{n}}' \cdot \mathbf{m}(\mathbf{r}')$ is the surface magnetic charge density, where $\hat{\mathbf{n}}'$ is the outward surface normal.

The demagnetizing energy favors magnetization configurations that minimize both volume and surface magnetic charges, leading to uniform bulk magnetization and in-plane orientation near surfaces to reduce stray fields. However, in extended geometries, a uniform magnetization generates significant demagnetizing fields that oppose the magnetization. To reduce the total energy, the system often forms alternating domains such as spin helices, stripe domains, or bubble domains, maintaining short-range alignment preferred by exchange while minimizing long-range stray fields.

2.2.6 Dzyaloshinskii-Moriya Interaction (DMI).

The Dzyaloshinskii–Moriya interaction (DMI) arises from spin–orbit coupling in systems lacking inversion symmetry and favors chiral alignment between neighboring magnetic moments [33, 34]:

$$E_{\mathrm{DMI}} = \mathbf{D}_{ij} \cdot \mathbf{S}_i \times \mathbf{S}_j \tag{2.11}$$

where $\mathbf{D}_{ij}$ is the DMI vector and depends on the mechanism by which inversion symmetry is broken. In the continuum model:

$$E_{\mathrm{DMI}} = \int_V \mathcal{D} : (\nabla \mathbf{m} \times \mathbf{m}) \tag{2.12}$$

where $\mathcal{D}$ is the spiralization tensor, which again depends on the DMI mechanism. For an isotropic interface with $C_{\infty v}$ symmetry, in-plane rotational symmetry restricts the spiralization tensor to one independent antisymmetric coefficient, $\mathcal{D}_{\alpha\beta} = D_{\mathrm{ind}} \epsilon_{\alpha\beta}$, where $\alpha, \beta \in \{x, y\}$. The tensor contraction therefore reduces to the scalar interfacial-DMI form:

$$E_{\mathrm{DMI}} = \int_V D_{\mathrm{ind}} \left[m_z \left(\nabla \cdot \mathbf{m} \right) - \left(\mathbf{m} \cdot \nabla \right) m_z \right] dV. \tag{2.13}$$

Here D_{ind} has units of $\mathrm{J/m^2}$, and its sign selects the preferred Néel-wall chirality. For lower-symmetry interfaces, the spiralization generally cannot be reduced to a single scalar.

2.2.7 Characteristic lengths.

2.2.7.1 Exchange length.

The exchange length is the spacing below which the exchange energy dominates over the demagnetizing energy:

$$l_{\mathrm{ex}} = \sqrt{2A_{\mathrm{ex}}/\mu_0 {M_s}^2} \tag{2.14}$$

2.2.7.2 Domain wall width.

The domain wall width corresponds to the width of Bloch walls in materials with significant perpendicular magnetic anisotropy. It is defined by the exchange stiffness and the effective uniaxial

anisotropy energy:

$$\Delta = \sqrt{A_{\text{ex}}/K_{\text{eff}}} \tag{2.15}$$

2.2.8 Temperature effects. Temperature reflects the thermal energy available to microscopic degrees of freedom. In a magnetic solid, increasing temperature populates lattice vibrations, electronic excitations, and spin fluctuations, which together reduce magnetic order and introduce fluctuations in the local magnetization. MuMax3 represents this behavior with a stochastic thermal field whose strength increases with temperature [35]:

$$\mathbf{B}_{\text{therm}} \propto \boldsymbol{\eta}(\text{step})\sqrt{T}, \tag{2.16}$$

where $\boldsymbol{\eta}$ represents random fluctuations. This field perturbs the magnetization direction more strongly as temperature increases, but it does not itself change the material parameters. For Fe/Gd specifically, the measured saturation magnetization M_s and uniaxial anisotropy K_u also vary with temperature [15]. Consequently, ferromagnets and antiferromagnets lose long-range order above their Curie temperature, T_{C}, and Néel temperature, T_{N}, respectively. These parameters are material-dependent. Ferrimagnets can also feature a compensation point, T_{comp}, where opposing sublattice moments cancel, resulting in net zero magnetization.

2.3 Landau-Lifshitz-Gilbert Equation and the Effective Field

The dynamics of the magnetization field in a continuum ferromagnet are governed by the Landau-Lifshitz-Gilbert (LLG) equation, which provides a phenomenological description of spin precession and dissipation across length scales [31, 36]. In the micromagnetic framework, the continuous vector field $\mathbf{m}(r, t)$ evolves in time according to competition between various conservative torques and dissipative processes that relax the system toward equilibrium. The LLG equation

is written as:

$$\partial_t \mathbf{m} = -\gamma_{\text{gyro}} \mu_0 \mathbf{m} \times \mathbf{H}_{\text{eff}} + \alpha \mathbf{m} \times \partial_t \mathbf{m} \tag{2.17}$$

where γ_{gyro} is the gyromagnetic ratio, and α is the dimensionless Gilbert damping parameter. The first term describes the precessional motion of the magnetization about an effective magnetic field. The effective magnetic field is defined as the functional derivative of the total magnetic free energy with respect to the magnetization. The second term introduces damping, which reflects energy dissipation and evolves the system towards an energy minimum. Examples of dissipative effects include spin-lattice coupling, Stoner excitations, and spin pumping.

2.4 Anatomy of Magnetic Domains

Magnetic domains are regions of uniform magnetization. The *domain wall* (DW) refers to the boundary between two domains with oppositely oriented magnetization. In a magnetic material with perpendicular anisotropy, such as Fe/Gd multilayers, domains prefer to orient in $+\hat{z}$ or $-\hat{z}$ directions. The orientation of a domain is referred to as polarity, $p = \pm 1$. The walls between these domains have two degrees of freedom through which they can rotate 180° smoothly. Néel walls rotate cycloidally across the domain wall, while Bloch walls rotate helically across the domain wall. The handedness of this rotation defines the domain wall chirality. Whether a domain wall is Néel- or Bloch-like can be quantified by γ, the domain wall helicity. This value corresponds to the angle between the domain wall normal ($\hat{n} \parallel -\nabla m_z$) and the in-plane magnetization at the domain wall:

$$\gamma(x,y) = \arg\left[\left(m_x(x,y) + i m_y(x,y)\right) p \left(-\partial_x m_z(x,y) + i \partial_y m_z(x,y)\right)\right] \tag{2.18}$$

where $\arg\left[(a_x + ia_y)(b_x - ib_y)\right]$ returns the angle between two-vectors $\mathbf{a}$ and $\mathbf{b}$ and the factor of p eliminates the polarity ambiguity of the helicity. If $\gamma = 0, \pi$, the magnetization points out of or into the core, and is referred to as an outwards or inwards Néel-type wall. If $\gamma = \pm\pi/2$, the magnetization points counter-clockwise (CCW) or clockwise (CW) and are called CCW/CW Bloch-type walls. Domain walls are rarely perfectly Néel- or Bloch-type, instead having a helicity somewhere in between. The differences between these types are shown in Fig. 4.

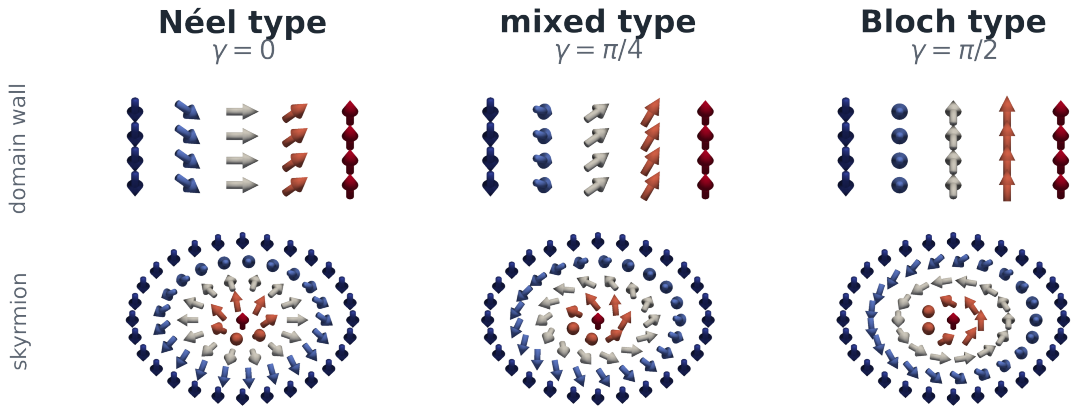

Figure 4. Schematic comparison of Néel, mixed, and Bloch helicity for straight domain walls and skyrmions. The helicity γ measures the in-plane magnetization angle relative to the local domain-wall normal or, equivalently for skyrmions, relative to the radial direction at the wall.

Domain walls can also contain defects internal to the wall. A Bloch line is a line defect where Bloch-wall segments with opposite rotation sense meet, so the domain-wall chirality changes along the wall rather than remaining uniform [31]. This defect can be nonsingular if the magnetization rotates smoothly through the meeting region, or singular if the rotation requires a localized point at which the continuum magnetization direction is not well defined. The corresponding three-dimensional singular defect is a Bloch point. Around a Bloch point, the magnetization spans all directions on a small enclosing surface, allowing the

winding of a domain wall or compact domain to change through a merger, collapse, or annihilation event [31, 37]. Since micromagnetic models usually assume a fixed magnetization magnitude, Bloch points should be understood as places where the continuum description requires an atomic-scale or otherwise regularized core. In thick dipolar multilayers, Bloch lines may extend through part of the film, reach a surface, or terminate on Bloch points, making them important for distinguishing trivial bubbles from continuously wound skyrmions in later chapters. Recent three-dimensional magnetic imaging makes this point concrete by resolving Bloch-point-mediated topology changes in hybrid skyrmion and antiskyrmion strings [38].

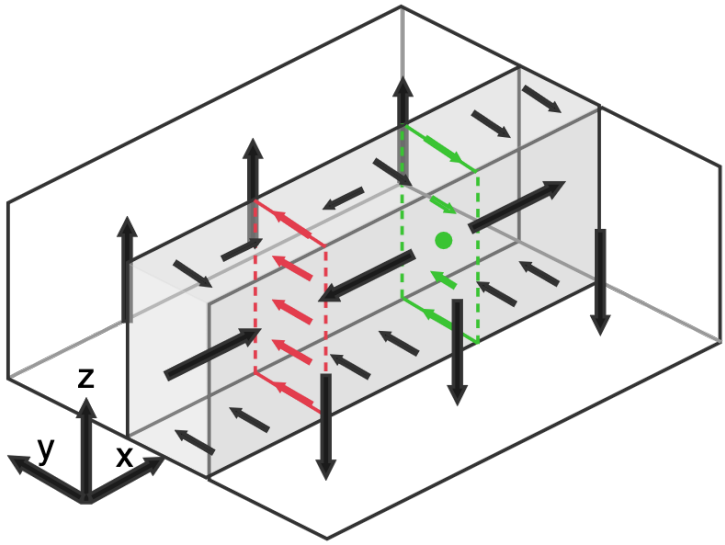

Figure 5. Schematic of Bloch-line formation at the meeting of Bloch walls with opposite rotation sense. Green marks a Bloch line with a singularity, while red marks a nonsingular meeting of oppositely rotating Bloch walls.

Magnetic solitons (e.g. skyrmions, antiskyrmions, and magnetic bubbles) are particle-like domain walls extended into two-dimensions by extruding a 1D domain wall onto itself. These domains can map to the unit sphere via a polar parameterization:

$$\mathbf{m}(r,\phi) = (\cos\Phi(\phi)\sin\Theta(r), \sin\Phi(\phi)\sin\Theta(r), \cos\Theta(r)) \tag{2.19}$$

Where the inclination of the magnetization, $\Theta(r)$, rotates from 0 at $r = 0$ to π at $r = \infty$, or vice versa depending on its polarity. This is often parameterized as:

$$\Theta(r) = -2 \arctan\left(e^{\frac{r-R}{p\Delta}}\right) \tag{2.20}$$

Where R is the skyrmion radius and Δ is the aforementioned domain wall width. Additionally, the azimuth of the magnetization, $\Phi(\phi)$ can be parameterized:

$$\Phi(\phi) = W\phi + \gamma \tag{2.21}$$

W, the vorticity or winding number, corresponds to the integer number of rotations completed by the in-plane magnetization after one loop around the domain wall. Positive W corresponds to a counter-clockwise rotation of the in-plane magnetization along the $\hat{\phi}$ direction.

Solitons are typically categorized by their topological charge or skyrmion number:

$$N_{\text{Sk}} = \frac{1}{4\pi} \int dxdy\ \mathbf{m} \cdot (\partial_x \mathbf{m} \times \partial_y \mathbf{m}) \tag{2.22}$$

which describes how many times $\mathbf{m}$ wraps the unit sphere [39, 40]. The resulting quantity strongly correlates with the stability and transport properties of the domain. In metallic magnets, the same spin Berry phase can act as an emergent magnetic field for conduction electrons and produce a topological Hall contribution [11, 41, 42]. Converting to polar coordinates simplifies this integral [11]:

$$N_{\text{Sk}} = \frac{1}{4\pi} \int_0^{\infty} d\rho \int_0^{2\pi} d\phi \frac{d\Theta(\rho)}{d\rho} \frac{d\Phi(\phi)}{d\phi} \sin\Theta(\rho) \tag{2.23}$$

Separating the radial and azimuthal integrals gives:

$$N_{\text{Sk}} = \frac{W}{2} \left[\cos\Theta(0) - \cos\Theta(\infty)\right] = pW \tag{2.24}$$

where the last equality holds for a regular texture whose core and far-field magnetization reach opposite poles of the unit sphere. The domain-wall profile

above is an asymptotic wall ansatz; if it is extended to $r = 0$ at finite R/Δ, it does not exactly satisfy the saturated-core boundary condition and can produce an apparent noninteger correction. That correction is an artifact of the ansatz, not a reduction of the topological invariant by a wide wall. For a closed, saturated soliton, the skyrmion number depends on its polarity and wall winding as $N_{\mathrm{Sk}} = pW$. Similarly, helicity can be extended to classify skyrmions as Néel/Bloch type, following the same domain-wall convention shown in Fig. 4. Common combinations of these classifiers and the resulting solitons are listed in Table 1.

N_{Sk}	W	p	γ	Description
1	1	1	$\pi/2$	Bloch Skyrmion, Right Handed, $+\hat{z}$ core
-1	1	-1	$-\pi/2$	Bloch Skyrmion, Right Handed, $-\hat{z}$ core
1	1	1	$-\pi/2$	Bloch Skyrmion, Left Handed, $+\hat{z}$ core
-1	1	-1	$\pi/2$	Bloch Skyrmion, Left Handed, $-\hat{z}$ core
1	1	1	0	Néel Skyrmion, Outwards, $+\hat{z}$ core
-1	1	-1	0	Néel Skyrmion, Outwards, $-\hat{z}$ core
1	1	1	π	Néel Skyrmion, Inwards, $+\hat{z}$ core
-1	1	-1	π	Néel Skyrmion, Inwards, $-\hat{z}$ core
-1	-1	1	N/A	Antiskyrmion $+\hat{z}$ core
1	-1	-1	N/A	Antiskyrmion $-\hat{z}$ core
0	0	1	N/A	Trivial bubble, $+\hat{z}$ core
0	0	-1	N/A	Trivial bubble, $-\hat{z}$ core

Table 1. Possible soliton configurations and corresponding lexicon.

2.5 Current driven dynamics

Having established the topological classification of magnetic solitons, I turn to their distinct responses to applied currents [9, 11].

In systems well described by localized spins, conduction electrons act as a bath that transfers angular momentum to a well-defined spin field. In contrast, in itinerant magnets the magnetic texture itself arises from the electronic structure, and current-driven dynamics emerge from changes in the electronic free energy and

spin-dependent Berry curvature of the bands. While the mechanisms of the driving torque differ, in both cases, the dynamics of rigidly translating magnetic domains can be described by a collective coordinate, $\mathbf{R}(t)$.

2.5.1 The Thiele equation. A phenomenological view of rigid domain dynamics yields the Thiele equation, which is widely used to describe the collective-coordinate motion of skyrmions and related solitons [9, 11, 31]:

$$\mathbf{G} \times \mathbf{v} + \alpha \mathcal{D} \mathbf{v} = \mathbf{F}_{\text{drive}} \tag{2.25}$$

Here $\mathbf{v} = d\mathbf{R}/dt$, α is the Gilbert damping parameter, and $\mathcal{D}$ is the scalar dissipative coefficient obtained in the isotropic limit of the dissipative tensor, $\mathsf{D} = \mathcal{D}\mathsf{I}$. The driving term, $\mathbf{F}_{\text{drive}}$, depends on the microscopic origin of the current-induced coupling. In a localized system, the coupling arises from spin-transfer and spin-orbit torques generated by conduction electrons exchanging angular momentum with the local magnetization. In itinerant magnets, the coupling emerges from the current-induced modification of the electronic free energy, expressed through the spin-Berry curvature and spin-orbit-coupled transport coefficients. Again, in the long wavelength limit, both systems reduce to an effective force proportional to the applied current density.

2.5.2 Skyrmion Hall Effect (SkHE) and Topological charge. The transverse dynamics are introduced by the gyrovector $\mathbf{G} = (0, 0, G_z)$, which is dependent on the local skyrmion charge density:

$$G_z = -\frac{M_s}{\gamma_{\text{gyro}}} \int dz \int dxdy \; \mathbf{m} \cdot (\partial_x \mathbf{m} \times \partial_y \mathbf{m}) \tag{2.26}$$

For the discussion in Ch. VI, this can be extended into three dimensions:

$$G_z = -\frac{4\pi M_s}{\gamma_{\text{gyro}}} \int dz \; N_{\text{Sk}}(z) \tag{2.27}$$

Thus, the gyrotropic response is determined by the depth-integrated topological charge. This allows contributions from different layers to partially cancel.

For a driving force applied along $\hat{x}$, the Thiele equation yields transverse and longitudinal velocities whose ratio defines the skyrmion Hall angle:

$$\theta_{\mathrm{SkHE}} = -\arctan\left(\frac{G_z}{\alpha \mathcal{D}}\right) \tag{2.28}$$

Any texture with nonzero integrated topological charge exhibits a transverse response under current. The sign of the Hall angle is set by the sign of the integrated charge, while its magnitude is controlled by the competition between gyrotropic and dissipative forces. In systems with depth-dependent structure, opposite-sign contributions to $N_{\mathrm{Sk}}(z)$ could reduce or even cancel the net deflection. Recent current-driven skyrmion experiments also show that the observed Hall response can evolve across dynamic regimes, rather than behaving as a single fixed material constant [43, 44].

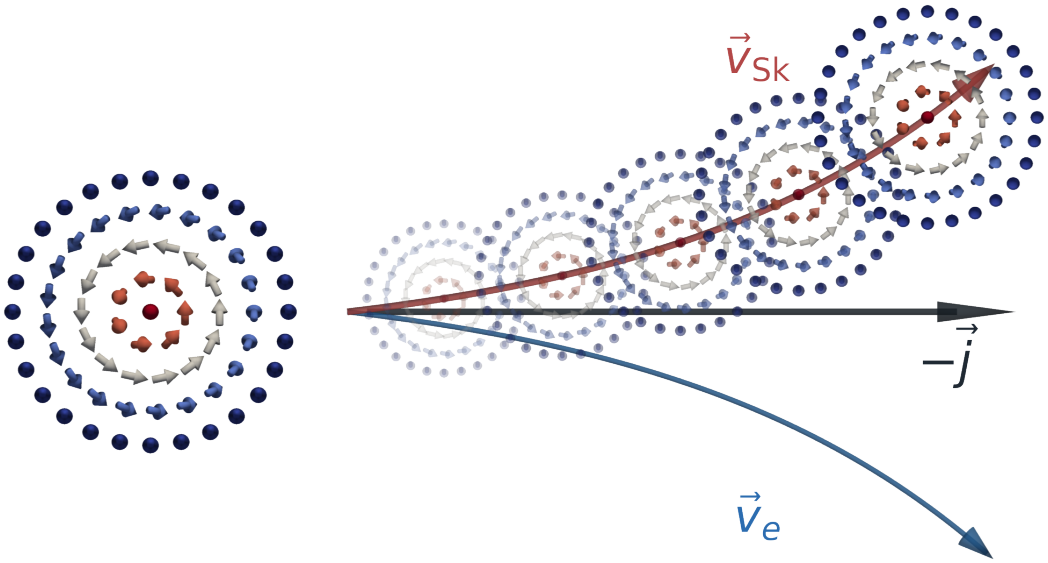

Figure 6. Schematic of current-driven skyrmion Hall motion. A current density along $-\vec{j}$ produces longitudinal motion and, for a texture with nonzero integrated topological charge, a transverse skyrmion Hall response. Faded skyrmion copies indicate the resulting deflected trajectory.

2.6 The Fe/Gd System

Fe/Gd thin films are rare-earth/transition-metal ferrimagnets in which the localized $4f$ moments of Gd couple to the more itinerant $3d$ moments of Fe. This material family is central to the remainder of this dissertation because it combines ferrimagnetic compensation, perpendicular magnetic anisotropy, low saturation magnetization, and strong dipolar effects in a film geometry that can be characterized with both electron and x-ray probes. Those ingredients place Fe/Gd in a useful regime for stabilizing three-dimensional stripe, bubble, and skyrmion textures.

2.6.1 Fe/Gd bilayers. The basic building block is an Fe/Gd bilayer. Fe and Gd each order ferromagnetically in isolation, but at the Fe/Gd interface their moments couple antiferromagnetically. A bilayer therefore behaves as a ferrimagnetic unit whose net moment is set by the relative Fe and Gd thicknesses, the temperature-dependent sublattice magnetizations, and the strength of the interfacial exchange. Previous work on Gd/Fe bilayers and related multilayers has shown that this balance produces tunable magnetization compensation, interface-sensitive anisotropy, and thermally dependent reversal behavior [45, 46].

Energetically, the antiferromagnetic interfacial exchange penalizes parallel Fe/Gd alignment and favors antiparallel sublattices across the interface. This coupling reduces the net saturation magnetization relative to either constituent ferromagnet and introduces a compensation point, T_{comp}, where the opposing sublattice moments cancel. The same interface also contributes to the effective anisotropy of the film. Thus, even before many repeats are added, the Fe/Gd bilayer must be understood through the competition among exchange, Zeeman, anisotropy, and demagnetizing energies, with the antiferromagnetic interface

determining how the Fe and Gd moments act as a coupled ferrimagnet rather than independent layers.

2.6.2 Fe/Gd multilayers. Fe/Gd multilayers repeat this bilayer motif many times, commonly using amorphous [Fe(0.34 nm)/Gd(0.40 nm)] bilayers fabricated by DC magnetron sputtering. Montoya, Fullerton, and collaborators showed that the number of repeats and the layer thicknesses tune the magnetization, anisotropy, domain period, and field range over which stripe and skyrmion phases are stabilized at room temperature [15, 47]. In this multilayer limit, the repeated antiferromagnetically coupled bilayers form an effective ferrimagnetic medium with reduced M_s and an amplified interfacial contribution to the perpendicular magnetic anisotropy.

The emergence of perpendicular domains in these stacks follows from this repeated-interface energetics. The antiferromagnetic Fe/Gd interfaces reduce the effective moment while the large number of repeats increases the interface-derived anisotropy contribution. When the effective perpendicular anisotropy overcomes the in-plane preference imposed by shape anisotropy, the multilayer develops perpendicular magnetic anisotropy. Because typical optimized stacks contain tens to hundreds of repeats, their total thickness is large enough that long-range dipolar interactions remain important. Fe/Gd multilayers therefore occupy a regime where exchange favors smooth walls, anisotropy favors out-of-plane domains, Zeeman energy tunes the field-dependent phase, and demagnetizing energy drives domain formation and depth-dependent wall structure.

This balance stabilizes skyrmions without relying on large intrinsic Dzyaloshinskii–Moriya interaction. The amorphous Fe/Gd system is statistically inversion symmetric, so its intrinsic DMI is negligible. Instead, the skyrmions

discussed throughout this dissertation are primarily dipolar skyrmions: their stability comes from the competition among exchange, perpendicular anisotropy, Zeeman energy, and magnetostatic fields. The material parameters used for representative micromagnetic modeling of these films are listed in Table 2.

For Fe/Gd multilayers, the quality factor

$$Q = \frac{2K_u}{\mu_0 M_s^2} \tag{2.29}$$

is less than unity. In this case, the uniform-film effective anisotropy, $K_{\text{eff}} = K_u - \mu_0 M_s^2/2$, is negative, and the usual local domain wall estimate $\sqrt{A_{\text{ex}}/K_{\text{eff}}}$ is not applicable. The actual domain-wall width in the thick multilayer is determined by the full three-dimensional balance, including nonlocal demagnetizing fields. The quantity $\Delta_u = \sqrt{A_{\text{ex}}/K_u}$ is therefore quoted as a characteristic material length rather than as the fully relaxed wall width.

Material Parameter	Value	Units
M_s	4×10^5	A/m
A_{ex}	5×10^{-12}	J/m
D_{ind}	0	J/m^2
K_u	4×10^4	J/m^3
l_{ex}	7	nm
Δ_u	11	nm

Table 2. Material parameters and characteristic lengths of $[\text{Fe}(0.34\,\text{nm})/\text{Gd}(0.40\,\text{nm})]_{\times 120}$ at room temperature.

2.6.3 Existing characterization of Fe/Gd multilayers. The Fe/Gd multilayer platform has been developed through a combination of magnetometry, reciprocal-space scattering, real-space magnetic imaging, transport, and micromagnetic simulation. SQUID and vibrating sample magnetometry establish the net moment, compensation behavior, hysteresis, and effective anisotropy used to place individual films within the Fe/Gd phase space [15, 48].

These measurements are especially important because the ferrimagnetic moment is strongly temperature and composition dependent.

Scattering measurements provide ensemble-averaged information about domain periodicity and three-dimensional order. Resonant soft x-ray scattering and polarized neutron scattering have been used to characterize stripe, bubble, and skyrmion phases, including the depth-dependent character of hybrid skyrmions in Fe/Gd multilayers [21, 48, 49]. Because these methods average over many domains, they are particularly useful for determining periodicity, phase boundaries, and the statistical structure of ordered skyrmion lattices.

Spin-transport measurements provide a complementary characterization channel because they couple magnetic morphology to electrical response. Spin-orbit-torque experiments demonstrated current-driven motion of room-temperature Fe/Gd dipole skyrmions, while longitudinal and Hall transport measurements connected field-dependent transport features to stripe, mixed stripe-skyrmion, skyrmion-lattice, and disordered skyrmion phases [47, 49, 50]. These measurements are especially useful when real-space images alone cannot determine how chirality, domain morphology, and emergent-field physics contribute to the measured device response.

Real-space imaging provides the complementary local view. Lorentz transmission electron microscopy (LTEM) images in-plane magnetic induction through phase contrast, while scanning electron microscopy with polarization analysis (SEMPA) images the near-surface magnetization vector. Together with micromagnetic simulation, these techniques have been used to identify the hybrid three-dimensional structure of Fe/Gd skyrmions and to connect surface helicity to the domain-wall structure through the film thickness [17, 47, 51]. Recent electron

holography and Lorentz scanning TEM holography have provided further routes for reconstructing projected induction fields in related Fe/Gd textures [52].

Emerging three-dimensional imaging methods now extend this picture beyond projected or surface-sensitive measurements. Vector ptycho-tomography has recently reconstructed the full three-dimensional magnetization of Fe/Gd multilayers, providing a direct experimental view of twisted domain walls and depth-dependent soliton structure [53]. These developments motivate the analysis in later chapters, where LTEM, SEMPA, and simulation are treated as a practical multimodal route to interpret three-dimensional Fe/Gd domains.

2.6.4 Three-dimensional magnetic domains. This section is based on recent work on the three-dimensional topology and real-space imaging of hybrid skyrmions in Fe/Gd multilayers, where I contributed to the application of the Hopf index, analysis of SEMPA and LTEM data, and simulation [17, 54].

In Fe/Gd multilayers, like many others, dipole skyrmions feature a depth-dependent structure. In the center of the multilayer, dipole skyrmions have large cross-sectional area while their domain-wall width is at a minimum. The domain wall here is Bloch-like. Towards either surface, the dipole skyrmion cross-sectional area shrinks while the domain-wall width grows. The domain wall helicity twists to become nearly Néel-type, with mixed helicity appearing between these limiting cases as in Fig. 4 [16, 17, 21]. This three-dimensional structure is not reflected by the two-dimensional skyrmion number. Instead, the Hopf index, its three-dimensional analog, can describe how the magnetization field links through the full volume [54]. For the axisymmetric hybrid-skyrmion geometry, boundary conditions, and inverse-tangent branch convention used in Ref. [54], the general Hopf invariant

reduces to a surface-helicity expression:

$$H = \frac{1}{\pi} \tan^{-1} [\cot \gamma_s] \tag{2.30}$$

For the dipole skyrmions studied there, this special-case expression gives $0.25 < H < 0.50$; it is not a general definition of the Hopf index for arbitrary three-dimensional textures.

2.6.5 Bloch points in Fe/Gd multilayers. Thiaville et al. [32] show that the leading continuum exchange cost of a Bloch point scales with exchange stiffness. The relatively low effective exchange stiffness of Fe/Gd therefore suggests a lower Bloch-point exchange cost than in higher-stiffness ferromagnets [15]. Its ferrimagnetic structure provides additional microscopic relaxation pathways: the antiparallel Fe and Gd sublattices can cant independently and undergo unequal longitudinal fluctuations, suppressing the net magnetization at the topological transition without requiring simultaneous loss of local order on both sublattices. Atomistic modeling shows that intersublattice exchange and magnetic compensation modify both exchange stiffness and reversal barriers in ferrimagnets [55]. The amorphous structure may further lower the accessible formation barrier by allowing the core to nucleate in locally weak exchange regions. Bloch-point cores experience an exchange-scale potential from the underlying atomic structure, so a disordered exchange landscape can plausibly provide locally favorable nucleation sites [56]. These effects can make Bloch-point-like termini less costly than in a homogeneous, rigid ferromagnet. Ultimately, the quantitative contribution is not captured by the effective single-sublattice micromagnetic model, but the qualitative expectation is that Bloch points are more accessible in Fe/Gd than in higher-stiffness ferromagnets.

2.6.6 Heavy metal interfaces.

The Fe/Gd multilayer system lacks large intrinsic DMI because of its amorphous, approximately centrosymmetric structure. However, spin-orbit coupling can be enhanced and inversion symmetry can be broken by introducing heavy-metal interfaces into the multilayer stack. Depending on the element chosen, these heavy metals can generate interfacial DMI at Fe/heavy-metal or Gd/heavy-metal interfaces, modifying the preferred wall chirality and shifting the balance between dipolar and chiral stabilization mechanisms [57, 58].

CHAPTER III

METHODS

Magnetism sits at the crossroads of well-developed theory and achievable experiment. Advances in nanofabrication, instrumentation, and characterization have made it possible to prepare and image magnetic textures directly. At the same time, growth in computational power has made large micromagnetic simulations practical enough to connect theory and experiment.

3.1 Experimental Methods

In Fe/Gd multilayers, the structures of interest are nanoscale, three-dimensional magnetic domains that cannot be imaged reliably with optical magnetic microscopy techniques. Most magnetic imaging in this dissertation therefore relies on electron microscopy, which can reach the length scales needed to resolve magnetic textures directly. However, electron-based magnetic imaging techniques each have inherent limitations. Transmission techniques such as LTEM integrate through the sample thickness and primarily measure projected in-plane induction. Surface-sensitive techniques such as SEMPA measure near-surface vector magnetization, but they sacrifice depth information and generally have lower spatial resolution than many transmission methods. As a result, any single imaging technique gives an incomplete picture of the magnetic texture. Used together with micromagnetic simulation, these methods form a model-informed multimodal probe of three-dimensional structure.

3.1.1 Lorentz Transmission Electron Microscopy (LTEM).

LTEM relies on the magnetic interaction between the electron beam and a magnetic sample. The sample imparts the Aharonov-Bohm phase on the plane

Method	Measured quantity	Sensitivity	Dissertation role
LTEM	Projected induction	Through-film	Field evolution
SEMPA	Surface vector magnetization	Top few Å	Boundary condition
MuMax3	3D magnetization and energy density	Full volume	Model testing
Domain Tracker	Objects, properties, and transitions	Simulation output	Dynamics and energetics analysis

Table 3. Summary and roles of experimental and computational methods used in this work.

wave of a coherent electron beam,

$$\Delta\phi = C_E \int dz V(\mathbf{r}_\perp, z) - \frac{\pi}{\Phi_0} \int_L d\mathbf{r} \cdot \mathbf{A}(\mathbf{r}_\perp, z) \equiv \phi_e + \phi_m \tag{3.1}$$

with an electrostatic term, ϕ_e, which depends on an interaction parameter, C_E, and a magnetic term, ϕ_m, which depends on the magnetic flux quantum, Φ_0. Spatial variations in image intensity correspond to nonuniform electrostatic and magnetic potentials in the sample. The resulting phase-contrast image encodes magnetic information. Assuming a uniform thin film, which is a good approximation for the Fe/Gd system, the magnetic phase can be recovered using the Single Image Transport of Intensity Equation (SITIE):

$$\nabla_\perp^2 \phi_m(\mathbf{r}_\perp) \approx \frac{2\pi}{\lambda \Delta f} \left(1 - \frac{I(\mathbf{r}_\perp, \Delta f)}{I_0}\right) \tag{3.2}$$

where λ is the electron wavelength and Δf is the image defocus. In summary, a single phase contrast image, $\mathbf{I}(\mathbf{r}_\perp, \Delta f)$, normalized by its average intensity, I_0 and assuming a uniform electrostatic phase, can recover the spatially-varying magnetic

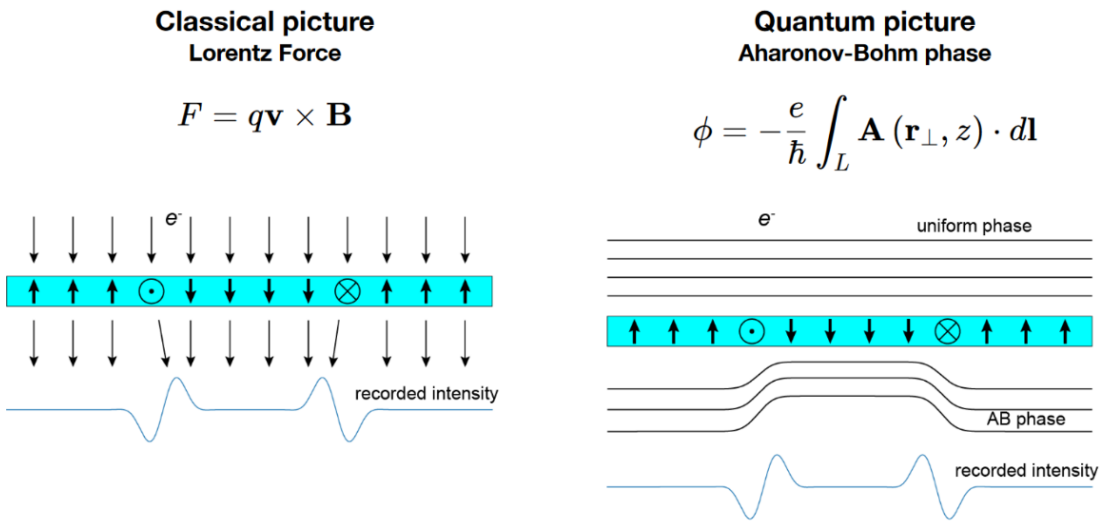

Figure 7. Classical and quantum pictures of LTEM magnetic contrast. In the classical picture, the Lorentz force deflects electrons as they pass through in-plane magnetic induction. In the quantum picture, the magnetic vector potential modifies the Aharonov-Bohm phase of the electron wave, which is converted into phase contrast upon propagation.

phase [59]. By defining the depth-integrated in-plane induction as

$$\mathbf{B}_\perp^{\mathrm{proj}}(\mathbf{r}_\perp) = \int \mathbf{B}_\perp(\mathbf{r}_\perp, z)\, dz. \tag{3.3}$$

The magnetic phase then satisfies:

$$\nabla_\perp \phi_m(\mathbf{r}_\perp) = -\frac{e}{\hbar}\mathbf{B}_\perp^{\mathrm{proj}}(\mathbf{r}_\perp) \times \hat{\mathbf{e}}_z \tag{3.4}$$

For a film of thickness τ, the effective thickness-averaged induction reported by the reconstruction is $\bar{\mathbf{B}}_\perp = \mathbf{B}_\perp^{\mathrm{proj}}/\tau$, so equivalently:

$$\nabla_\perp \phi_m = -\frac{e\tau}{\hbar}\bar{\mathbf{B}}_\perp \times \hat{\mathbf{e}}_z \tag{3.5}$$

Throughout this dissertation, magnetic images are displayed looking toward $-\hat{z}$; negative out-of-plane field points into the image plane along $-\hat{z}$. Will Parker's `ltempy` Python package was used throughout this dissertation to process and visualize LTEM data, SPLEEM/SEMPA vector maps, and simulated magnetization fields; for LTEM analysis, it implements SITIE to produce in-plane magnetic

induction maps from phase-contrast images [60]. Related LTEM/SITIE workflows have been used to map induction and domain-wall chirality in skyrmionic materials [59, 61].

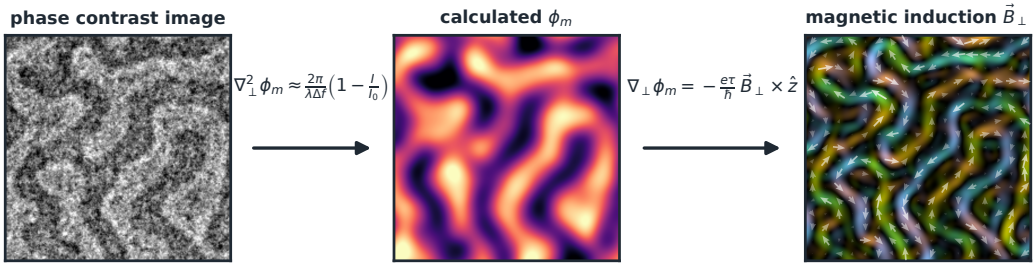

Figure 8. SITIE workflow applied to LTEM data. A phase-contrast image is converted into magnetic phase, ϕ_m, using the single-image transport-of-intensity equation; spatial gradients of ϕ_m then give the projected in-plane magnetic induction, shown using a CIELAB-style color representation with white arrows indicating the local induction direction.

3.1.2 Scanning Electron Microscopy with Polarization Analysis (SEMPA).

SEMPA is a JEOL JAMP-7830F Auger microprobe modified to perform surface-sensitive real-space vector magnetometry by the addition of two Mott detectors [62, 63]. As the electron beam scans across the sample, primary electrons strike the sample and free secondary electrons in the interaction volume, a teardrop-shaped region within the top few angstroms of the material. The optics along the SEMPA column capture and accelerate these secondary electrons, selecting for energies with representative magnetic polarization. At the end of the column, pre-detection optics guide these electrons to one of two Mott detectors where the electrons Mott scatter off of a gold target. The scattered electrons are binned and counted to determine the net polarization along those two axes. This process is repeated with the other Mott detector to measure the polarization along

the third axis while the redundant axis is used for alignment. Software is used to align the scans and reconstruct the three components of the surface magnetization.

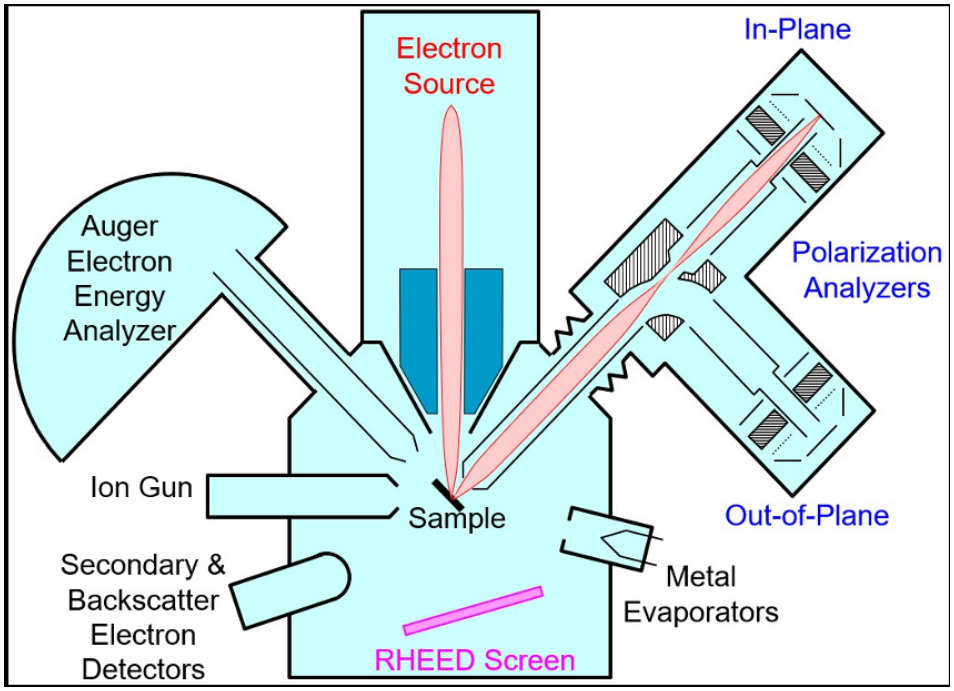

Figure 9. SEMPA microscope schematic. Secondary electrons emitted from the sample are collected and sent to polarization analyzers that measure orthogonal components of the surface magnetization.

3.2 Computational Methods

To connect theory and experiment throughout this work, I performed micromagnetic simulations and developed a domain-tracking package built on image analysis and computer-vision techniques.

3.2.1 Micromagnetic Simulation. Micromagnetic simulations were performed using MuMax3 [35], which can numerically minimize total energy or handle full dynamics by solving the LLG equation (see Sec. 2.3). MuMax3 handles three-dimensional simulated geometry and returns arrays of magnetization components and contribution-specific energy densities. Additional features include temperature effects and current-driven dynamics.

3.2.2 Domain Tracker. To analyze domain evolution, we developed a custom Python package ("Domain Tracker") that processes MuMax3 output and extracts structural and energetic information. The source is available at `https://github.com/jareddi/domain-tracker`. The package is not treated here as a new physical theory; its role is to make the simulation analysis reproducible, object-based, and scalable across many time steps. In practice, this means that domain boundaries, matching thresholds, classification rules, and transition labels are applied consistently to each simulation frame rather than selected by manual inspection of individual snapshots.

Each simulation frame consists of magnetization and energy `.ovf` files. For each frame, the m_z slices were processed with OpenCV's `findContours()` function to identify perpendicular domains [64], which were then stitched into three-dimensional Domain objects. The contour surface is referred to as the domain wall, and the contour surface plus enclosed volume is referred to as the domain core or total domain. Each Domain object stores local properties, including contour shape, center of mass, and energetics. These objects are further processed into a Frame object containing all domains for a given time step.

To track domains across time, Domain objects from consecutive frames were compared using center-of-mass proximity and intersection-over-union (IoU) metrics. Domain objects satisfying the matching thresholds were linked into DomainChron objects, which provide chronological records of domain evolution. This step also assigns global domain IDs and records splitting or merging events. The output is a dictionary of DomainChron objects, each containing the time-resolved history of a magnetic domain. Domain-classification algorithms then sort domains into categories and identify transitions. This chronological sorting

enables rapid extraction of structural and energetic information during dynamic processes and provides an auditable route from simulated magnetization arrays to the population statistics reported in later chapters.

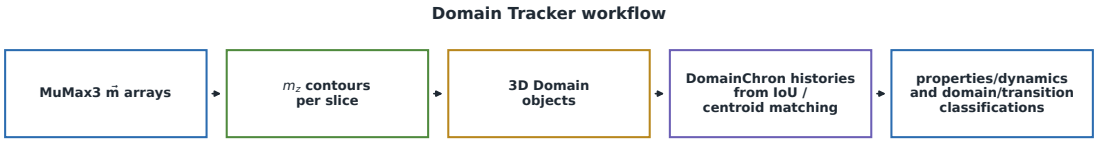

Figure 10. Domain Tracker analysis workflow. MuMax3 $\mathbf{m}$ arrays are segmented into m_z contours in each slice, stitched into three-dimensional Domain objects, linked into DomainChron histories using intersection-over-union and centroid matching, and then harvested for properties, dynamics, domain classifications, and transition classifications.

CHAPTER IV

THE ZOO OF DOMAINS IN FE/GD MULTILAYERS

Publication and Contribution Note

This chapter summarizes magnetic textures in Fe/Gd multilayers that have been established through prior work by both the author and by past group members and collaborators. The LTEM and SEMPA datasets presented here were acquired by the author as well as previous group members and collaborators. Specifically, the results from the use of LTEM and SEMPA on skyrmions builds on the author's previous collaborative work: "Real space imaging of dipole-stabilized hybrid skyrmions in magnetic multilayer thin films" [17]. The author extends this LTEM/SEMPA analysis stack to worm domains using LTEM data acquired by Will Parker. This chapter also summarizes domain phase characterization and interpretations used in later chapters. The various images of different domain phases come from Jordan Chess, Will Parker, and the author; the discussion of the various transitions between these phases is original.

4.1 Role of this Chapter

Fe/Gd multilayers commonly host a variety of extended stripes and compact circular 'bubble' domains. These domain types have been reported in earlier Fe/Gd studies using real-space imaging, reciprocal-space scattering, transport, and micromagnetic simulation [15, 17, 21, 47, 51]. This chapter therefore serves as a bridge between the general magnetic background of Ch. II and the more specific results of Chs. V and VI as well as a showcase of the multimodal methods used to image and analyze magnetic structures in Fe/Gd multilayers.

Magnetic domains are emergent mesoscale structures that arise from the collective minimization of magnetic energies. For that reason, much of magnetic-

materials research treats domains phenomenologically: experiments identify the textures that actually appear under given fields, temperatures, and sample histories, while simulations test which magnetic configurations can reproduce those observations and explain their stability. This phenomenological approach is especially useful in Fe/Gd, where several domain types are close in energy and can coexist within the same material platform.

The central problem is that a domain is rarely determined by its outline alone. In a perpendicularly magnetized film, a stripe, bubble, or skyrmion can all appear as bright and dark magnetic contrast in a projected image. The important distinctions often live in the domain wall: its helicity, its winding number, the presence or absence of Bloch lines, and the way those quantities vary through the film thickness. Fe/Gd is especially sensitive to this issue because the films are thick enough for dipolar fields to twist the domain walls through the multilayer. A two-dimensional morphological picture is useful, but it is incomplete.

This chapter introduces the practical "zoo" of Fe/Gd domains in that spirit. Rather than repeating the full energetics discussion from Sec. 2.6, I use the energy terms only where they help interpret the observed textures. The main emphasis is experimental: what LTEM sees, what SEMPA adds, and why the pairing of those techniques, together with simulation, provides a useful route to three-dimensional interpretation. The paired LTEM/SEMPA workflow has already been demonstrated in Fe/Gd [17]; here it is treated as an established framework that can be reused and extended.

Figure 11 gives a representative visual overview of the domain phases discussed in this chapter. The panels are not meant to define a phase diagram with sharp thermodynamic boundaries. Instead, they show the experimentally

useful morphology classes that recur during Fe/Gd field sweeps: Type-II bubble lattices, ordered and labyrinthine stripe states, stripe collapse, skyrmion-rich bubble lattices, mixed skyrmion/Type-II populations, isolated domains, and remanent worm/skyrmion states. This is intended as a practical reference for preparing future investigations.

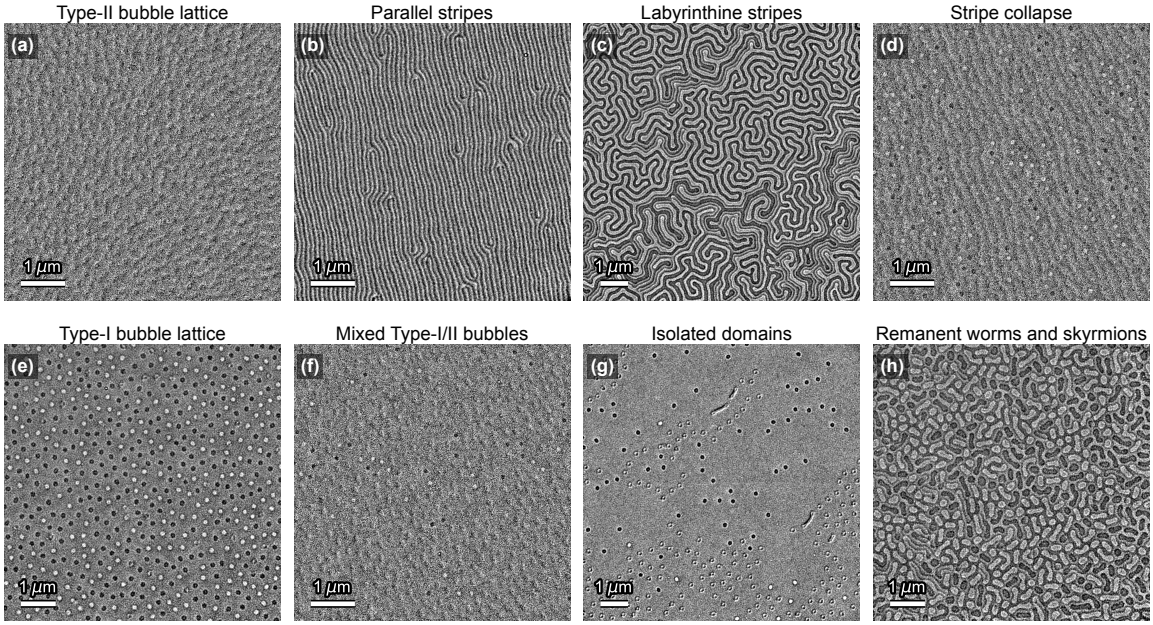

Figure 11. Representative LTEM images of the common Fe/Gd domain phases discussed in this chapter. The same sample, under different field histories can produce Type-II bubble lattices, parallel stripes, labyrinthine stripes, stripe collapse, skyrmion lattices, mixed skyrmion/Type-II bubble states, isolated domains, and remanent worms and skyrmions.

4.2 Why a Domain Zoo is Needed

The phrase "domain zoo" is informal, but it captures a real classification problem. Fe/Gd does not present a single isolated texture. Instead, small changes in applied field, temperature, sample thickness, anisotropy, or local disorder can drive transitions between extended stripes, dense skyrmion lattices, disordered skyrmion phases, isolated bubbles, and mixed populations. These states are

connected by field history. A skyrmion lattice, for example, is commonly reached by first forming parallel stripes and then increasing the out-of-plane field until the stripes pinch off into bubbles or skyrmions.

The classification is further complicated by the centrosymmetric character of amorphous Fe/Gd. In chiral multilayers with strong interfacial DMI, the domain-wall helicity is often fixed by the material properties. In Fe/Gd, the DMI is negligible, so clockwise and counter-clockwise Bloch-like walls are equally likely, excluding field-history. The domain-wall helicity can then be chosen by local dipolar fields, geometry, defects, and magnetic history. This near-degeneracy is what makes Fe/Gd a flexible skyrmion platform, but it also means that multiple textures with similar projected morphology can coexist.

For the purposes of this chapter, it is useful to distinguish achiral, chiral, and mixed-chirality stripe states. Chiral domains have a uniform wall chirality along their length and have a winding number of +1. Achiral domains can be understood as domains with exactly two chirality reversals and have a winding number of 0. Mixed chirality domains are worm or stripe domains which contain four or more chirality reversals such that isolated regions of the domain may appear chiral and others achiral.

For the rest of the dissertation, the useful classification is not simply "stripe" versus "bubble." The relevant questions are:

- Does the domain-wall magnetization wind once around the object, producing a Type-I dipole skyrmion?
- Does the wall contain Bloch lines? Is the domain chiral, achiral, or mixed chirality?

– Does the topology or helicity vary with depth, refining the three-dimensional description of the object?

– Which parts of this classification can be inferred from LTEM or SEMPA alone, and which require simulation?

Figure 12 shows the same classification ambiguity at a more local scale.

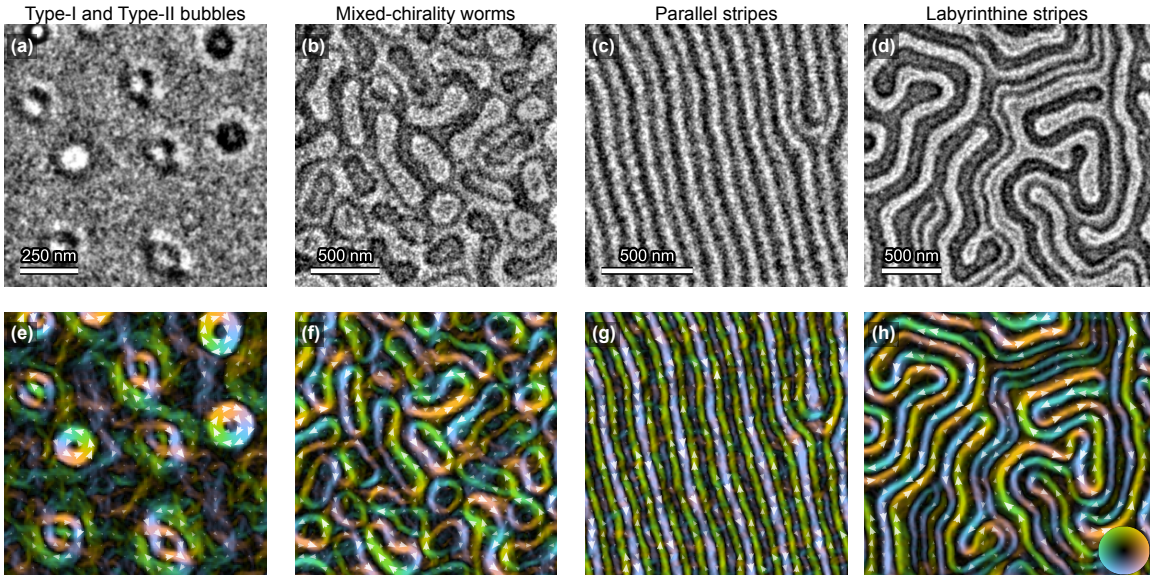

Figure 12. LTEM close-ups of representative Fe/Gd domain signatures. The top row shows phase-contrast images, and the bottom row shows the corresponding projected in-plane magnetic induction.

4.3 Stripe Domains

At low applied out-of-plane field, Fe/Gd multilayers commonly form extended stripe domains: long, narrow regions of uniform magnetization separated by domain walls. In stripe phases, the magnetization forms periodic, alternating $+\hat{z}$ and $-\hat{z}$ domains over long lateral distances. Overall, this arrangement balances $+\hat{z}$ and $-\hat{z}$ regions. Energetically, this minimizes the competition between perpendicular anisotropy and dipolar energy. The periodicity of the stripes

Texture	Domain-wall/topological structure	Imaging signature	Role in this dissertation
Type-I dipole skyrmion	Compact bubble with continuous wall winding and uniform layer-resolved skyrmion number; in Fe/Gd the wall twists through the thickness.	Bloch-like circulation in LTEM; Néel-like circulation in SEMPA.	Desired domain in spintronics applications. The goal of Ch. V is to investigate its formation.
Type-II bubble	Compact topologically trivial bubble with a Bloch-line pair and zero net winding.	Bubble-like morphology with an achiral domain wall associated with a pair of Bloch lines.	Immediate collapse product and competing final state in Ch. V.
Worm domain	Remanent elongated domain formed when Type-I skyrmions or Type-II bubbles expand, merge, or extend into noncompact objects; wall chirality can be chiral, achiral, or mixed.	LTEM contrast with local compact-domain ancestry often visible. Chiral Néel caps in the SEMPA dataset shown here.	Remanent bridge between compact bubbles/skyrmions and extended stripe textures.
Stripe domain	Extended wall separating alternating perpendicular domains; morphology may be parallel, labyrinthine, or branched, and wall chirality can vary along the stripe.	Long-range LTEM Fresnel/SITIE contrast; alignment and connectivity reflect tilt, field history, and merger geometry.	Parallel form is the parent state for field-driven collapse in Ch. V.

Table 4. The Fe/Gd domain zoo. The table emphasizes that domain identity depends on wall winding, Bloch-line structure, depth dependence, and measurement modality rather than on outline alone.

corresponds to an equilibrium where the dipole field from one domain minimizes the magnetostatic energy of the antialigned domain. The wall length is costly

because of exchange and anisotropy, but the alternating pattern reduces the magnetostatic cost compared to a uniformly magnetized film. Characteristic of a centrosymmetric multilayer, a stripe may consist of many chirality reversals (Bloch-lines). While these Bloch-lines are energetically unfavorable by the exchange energy, they are largely a consequence of local domain history and the phase transition that formed the stripes. Stripes may also branch, where two stripe domains merge into a fork. Such branches may be produced by defects, local stray fields, or as a consequence of the mismatch between the stripe periodicity and sample size.

In LTEM, stripe phases are usually the easiest Fe/Gd texture to identify but distinguishing their structure is rather deceptive. Their elongated domain walls produce extended bright and dark contrast in Fresnel images, and consequently SITIE reconstructions clearly reproduce the in-plane induction along their walls. However, depending on whether the Bloch wall on the opposite side has the same chirality (chiral, aligned antiparallel) or the opposite chirality (achiral, aligned parallel) the stripe appears differently. In the classical picture, if the domain is chiral, both domain walls deflect electrons away or towards the core. Generally, this maximizes contrast. If the domain is achiral, one domain wall deflects electrons away from the core while the other deflects them towards the core. This results in a more complex contrast pattern, where the stripe periodicity can appear to double depending on imaging conditions. Depending on the number of Bloch-lines, a stripe domain may have multiple regions of mixed chirality. Additionally, the magnetization at a Bloch-line points radially inwards or outwards, so Fresnel contrast vanishes. Since LTEM is not sensitive to out-of-plane magnetization, distinguishing the outline of a stripe with a Bloch-line is challenging. With all of

these factors in play, phase contrast images of stripe domains are often difficult to interpret. It is best practice to consider the field-sweep history that produced the resulting domain state. For these reasons, stripe domains are much easier to resolve in SEMPA, where the cores are easily identifiable by the z component of the magnetization. However, any chirality switches cannot be resolved as a consequence of the surface sensitivity and the domain's Néel cap structure.

4.4 Worm Domains

Worm domains resemble fully developed stripes but occur at a different stage of the field history. They appear when an external out-of-plane field is reduced *after* stripe collapse has nucleated compact bubble domains. As the field is lowered, the bubble cores, which are antialigned with the field, expand. A worm can form when neighboring Type-I skyrmions or Type-II bubbles merge, or when an individual bubble extends without fully joining a long stripe network. This remanent origin means that worms can inherit chiral, achiral, or mixed-chirality wall segments from the bubbles or skyrmions that produced them.

In SEMPA, worm domains reveal the near-surface closure structure. The surface wall magnetization twists to acquire a radial component that reduces stray field. Figure 13 compares this near-surface view with the projected induction measured by LTEM. In the LTEM field of view, many walls reverse between clockwise (CW) and counter-clockwise (CCW) chirality along a single contour. These reversals directly identify achiral or mixed-chirality domains, whereas contours with one color retain a uniform projected chirality. By contrast, the SEMPA field of view contains only uniformly CW or CCW contours, with no comparable chirality reversals.

This contrast is consistent with a depth-dependent wall structure in at least some worm domains: LTEM integrates the induction through the film, while SEMPA is sensitive to the near-surface magnetization. It is not, by itself, proof of depth-dependent topology. The two measurements do not image the same field of view or necessarily the same domain population, and a remanent state prepared from a predominantly Type-I bubble lattice could naturally contain mostly chiral worms. This comparison therefore suggests a three-dimensional interpretation without confidently declaring one.

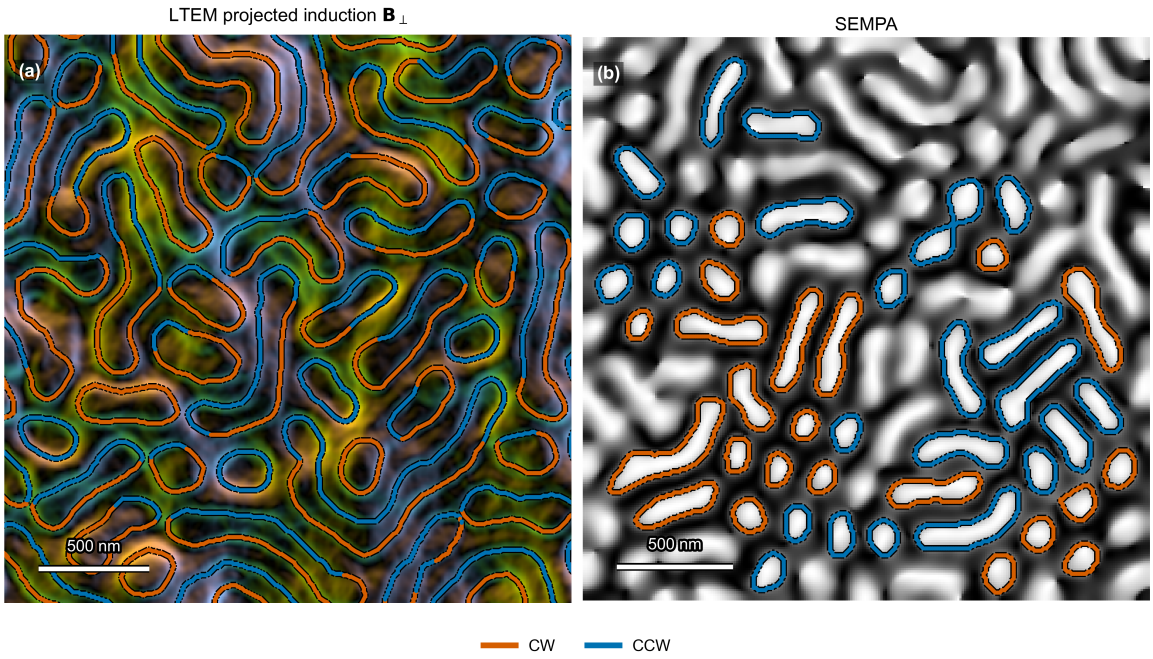

Figure 13. Comparison of domain-wall chirality measured by LTEM and SEMPA at remanence. Orange and blue denote clockwise (CW) and counter-clockwise (CCW) chirality, respectively. A uniformly colored contour is chiral in the corresponding measurement, whereas a color reversal along one contour marks a chirality reversal associated with a Bloch line and therefore identifies an achiral or mixed-chirality wall. The LTEM field of view contains numerous chirality reversals, while the SEMPA field of view contains only uniformly CW or CCW contours.

4.5 Type-II Bubbles

When an out-of-plane field favors one domain polarity, stripes can contract and pinch off into isolated bubble domains. The simplest topologically trivial bubble in this system is commonly called a Type-II bubble. It contains a pair of Bloch lines along the domain wall, so the in-plane magnetization does not complete a single continuous winding around the bubble. In the two-dimensional classification of Sec. 2.4, this corresponds to zero net skyrmion number. When an in-plane field component is present, the Bloch-line pair tends to align with that field direction. This alignment provides a simple way for field tilt to bias later merging and collapse pathways.

Type-II bubbles are important because they may appear wildly different in projection. The two Bloch lines produce a characteristic asymmetry in the projected induction, and under tilt or through-thickness twisting this contrast can resemble biskyrmion-like images. Loudon et al. [65] emphasized this problem in the broader context of LTEM interpretation, showing that projected induction can be misleading if it is treated as a direct map of the underlying magnetization. In Fe/Gd, the same caution applies. A Type-II assignment should be based on the wall winding and Bloch-line structure, not merely on the bubble outline. However, Ch. V posits that this variety in projected appearance may reflect a mixed depth topology.

From the energetic point of view, Type-II bubbles are natural in centrosymmetric, dipolar films. The Bloch-line pair structure paired with an elliptical morphology minimizes the exchange energy by minimizing gradients in the magnetization. Since Type-II bubbles form as the external field is lowered from saturation, these easily form to minimize the demagnetizing energy without

significantly increasing the exchange energy. Their achiral structure matches the lack of a globally fixed chirality in a centrosymmetric material. As shown in Ch. V, Type-II bubbles can also act as immediate products of stripe collapse before relaxing into other textures.

4.6 Type-I Dipole Skyrmions

The Type-I bubble, or dipole skyrmion, is the central topological texture in Fe/Gd. In each two-dimensional layer, the domain-wall magnetization winds once around the bubble, giving a nonzero skyrmion number whose sign depends on polarity and vorticity. Unlike DMI-stabilized skyrmions, Fe/Gd dipole skyrmions are stabilized primarily by the competition between exchange, anisotropy, Zeeman energy, and dipolar fields [15]. They form at room temperature and can be organized into dense skyrmion phases over suitable field and temperature ranges.

In LTEM, a Type-I dipole skyrmion produces a circular or near-circular projected induction pattern with continuous circulation around the wall. SITIE reconstructions can therefore separate many Type-I domains from Type-II bubbles by the absence of a Bloch-line-pair signature. However, LTEM still gives a projection. It can identify the projected circulation, but it cannot tell whether the helicity is constant through the film.

SEMPA and simulation show that the helicity is not constant. The Fe/Gd Type-I dipole skyrmion has a hybrid three-dimensional wall structure: the wall is more Bloch-like near the film midplane and more Neel-like near the surfaces [17]. Neutron scattering and recent three-dimensional imaging work support the same physical picture of depth-dependent skyrmion structure in Fe/Gd multilayers [21, 53]. The surface twist reduces magnetostatic energy by forming flux-closure caps, while the Bloch-like interior preserves the dipolar skyrmion character. This is

why a Type-I skyrmion in Fe/Gd should be thought of as a three-dimensional tube with a twisted wall, not as a perfectly uniform two-dimensional texture extruded through the film.

This hybrid structure is not a separate domain type; it is the rigorous three-dimensional description of the Type-I dipole skyrmion in a thick dipolar multilayer. It also changes the topological language. A two-dimensional skyrmion number can be evaluated layer by layer, but it does not describe how the wall helicity twists through the full three-dimensional volume. Parker et al. [54] showed that Fe/Gd Type-I dipole skyrmions can be interpreted as fractional or half-integer Hopfion-like textures, with the Hopf index connected to the amount of helicity twist between the film center and the surfaces. This interpretation does not replace the layer-resolved skyrmion number. Instead, it adds a three-dimensional descriptor for the topology of the full magnetization field.

For this dissertation, the practical lesson is simple: surface-sensitive and projected images are not redundant. The surface wall direction measured by SEMPA helps determine how much the texture twists through the film, while LTEM constrains the projected induction. In hybrid Fe/Gd walls, the opposing radial contributions of the two Néel caps largely cancel in the thickness projection, so the circulating LTEM signal retains substantial sensitivity to the Bloch-like interior or core even though it is not layer resolved. Reproducible state preparation then permits class-level comparison between LTEM and SEMPA datasets without implying that the same individual object was measured. Together with simulation, these measurements form a model-informed constraint on the three-dimensional topology that later chapters analyze more directly [17].

The paired-imaging logic is shown explicitly in Figs. 14 and 15. LTEM and SEMPA assign different effective helicities to the same class of dipole-stabilized skyrmions because the two measurements sample different projections of the three-dimensional wall. Simulations then provide the missing depth coordinate, showing how the wall rotates from Bloch-like character in the film interior toward Neel-like closure caps at the surfaces.

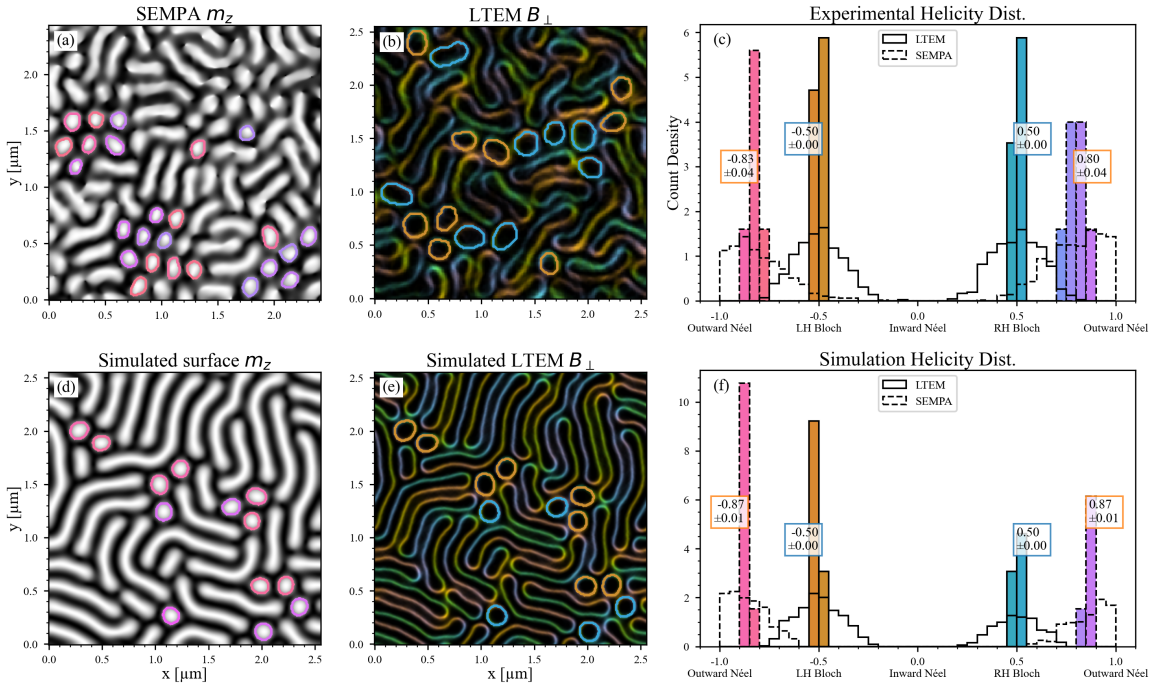

Figure 14. LTEM, SEMPA, and micromagnetic-simulation signatures used to identify the three-dimensional hybrid structure of dipole-stabilized Fe/Gd skyrmions. SEMPA measures the near-surface magnetization, while LTEM measures the projected in-plane induction through the sample thickness. The experimental helicity distributions and the corresponding simulated distributions show that the surface-sensitive and projected measurements select different helicity components of the same three-dimensional object. Reproduced from the coauthored work in Ref. [17].

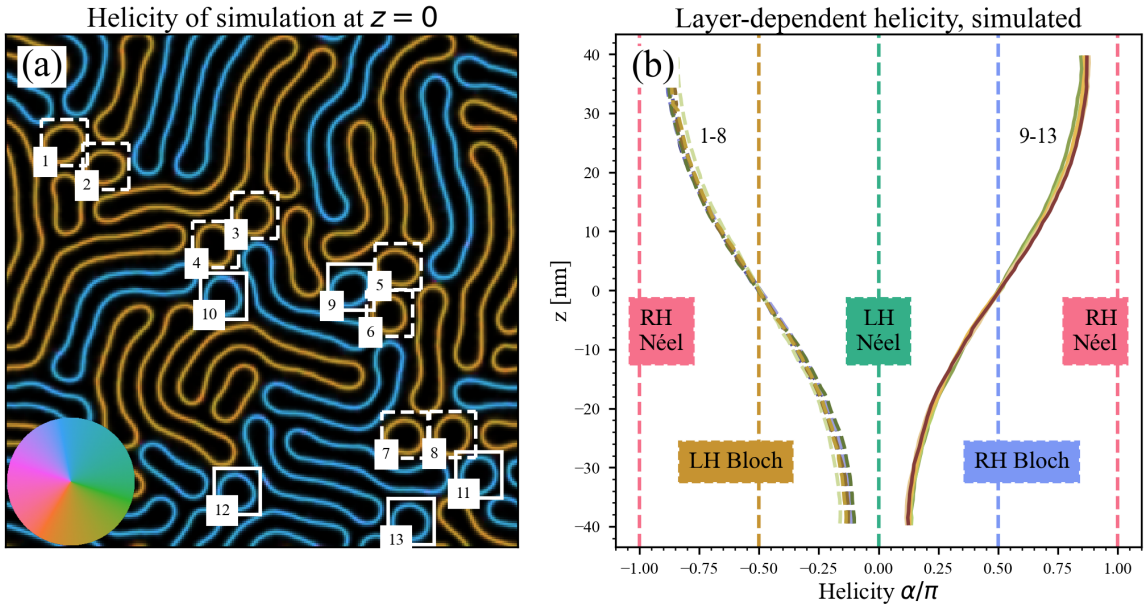

Figure 15. Simulated layer-dependent helicity for the same hybrid-skyrmion interpretation. The midplane helicity map identifies representative skyrmions, and the depth-resolved helicity curves show the wall twisting from Bloch-like character near the film center toward Neel-like closure caps near the surfaces. This depth dependence is the three-dimensional structure that LTEM and SEMPA infer indirectly when interpreted together with micromagnetic simulation. Reproduced from the coauthored work in Ref. [17].

4.7 Field-History Pathways Through the Domain Zoo

This section is intended as a phenomenological guide for new researchers, based on accumulated experimental experience rather than a quantitative thermodynamic phase diagram. The text and Fig. 16 distinguish experimentally observed transitions from phenomenologically inferred connections. The domain types described above are connected by field history. Figure 16 summarizes these connections as a directed graph rather than as a single linear hysteresis loop. The horizontal placement roughly follows progression through external field from one saturated polarity to the opposite saturated polarity, while the vertical placement separates pathways favored by different tilt histories. A saturated Fe/Gd multilayer first forms compact reversed domains as the out-of-plane field is reduced. In the common achiral pathway, these compact domains are Type-II bubble lattices containing Bloch-line pairs. If the sample is tilted, the resulting in-plane field component biases the orientation of those Bloch lines.

Further reduction of the out-of-plane field allows Type-II bubbles to expand and merge. This produces the first major branch in the domain pathway. With finite tilt, Type-II bubbles can merge into parallel stripes; reversing the sweep can return those stripes to the Type-II bubble lattice, so this is a reversible transition. At zero tilt, there is no preferred in-plane direction for merge events, and Type-II bubbles assemble into labyrinthine stripe domains. Thus labyrinthine and parallel stripes are not separate entries in the zoo; they are different morphologies produced by related Type-II-bubble merge events under different tilt conditions.

The distinction revealed in Fig. 16 is that not every geometrically plausible transition is physically equivalent. Some transitions are only allowed after the domain core polarity has inverted. This is especially important for the labyrinthine-

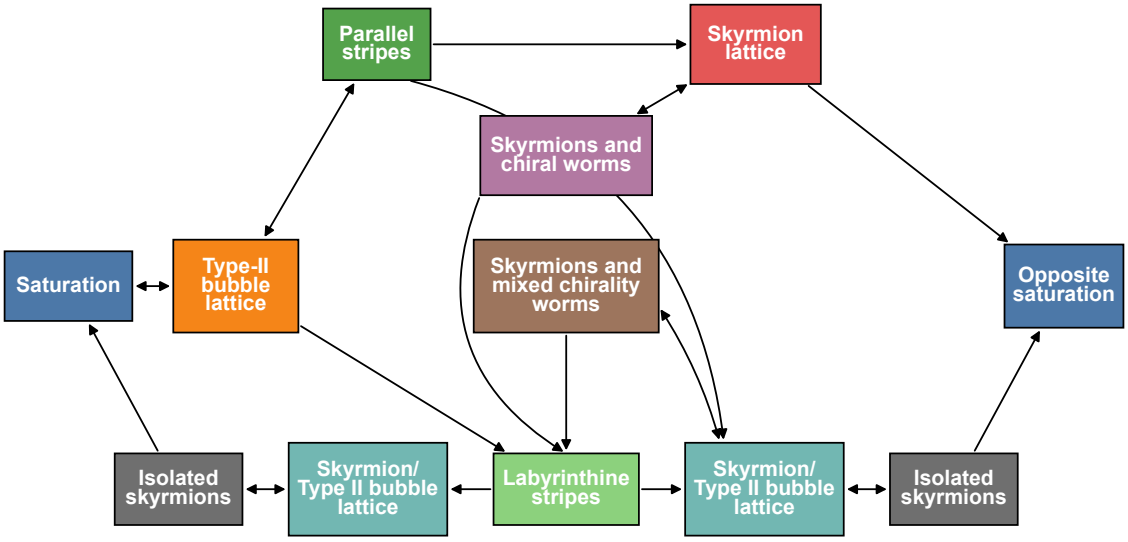

Figure 16. Field-history graph connecting the common Fe/Gd domain states discussed in this chapter. Arrows indicate experimentally observed or phenomenologically inferred field-sweep transitions. Double-headed arrows denote reversible transformations that do not require a change in topological charge, such as Type-II bubble generation/annihilation or field-driven expansion and contraction of skyrmions and worm domains. The duplicated skyrmion/Type-II bubble lattice and isolated-skyrmion nodes represent analogous states on opposite sides of the labyrinthine-stripe branch.

stripe branch: every transition connected to the labyrinthine-stripe state in this graph should be read as involving a core-polarity inversion or the negative-space reinterpretation that follows such an inversion. The transitions from skyrmions with chiral worms or mixed-chirality worms back into labyrinthine stripes therefore do not simply redraw the same walls; they require the field history to pass through the polarity-inverted state. Likewise, collapse of labyrinthine stripes into the left-hand skyrmion/Type-II bubble lattice is only available after the same polarity inversion has selected the appropriate core polarity.

On the tilted-field branch, parallel stripes can collapse into a skyrmion lattice or into a mixed skyrmion/Type-II bubble lattice. The former is less common in the field histories emphasized here, but it is the clean topological outcome: chiral stripe segments preserve a coherent wall winding and can pinch off into skyrmions. The mixed skyrmion/Type-II bubble lattice reflects local competition between continuous winding and Bloch-line-bearing trivial bubbles. Returning toward remanence can expand skyrmions into chiral worms or mixed-chirality worm states without changing their underlying topological charge.

This is why the reversible links in Fig. 16 should not be interpreted as topology-changing events. Type-II bubble generation and annihilation involve topologically trivial objects with zero net skyrmion charge, so creating or removing them does not require changing a nonzero topological invariant. Similarly, field-driven expansion and contraction between a skyrmion lattice and skyrmions or chiral worms changes domain size and connectivity, but it does not by itself change the skyrmion charge of the continuously wound objects. Topology-changing events enter when stripe collapse selects between a continuously wound skyrmion and a Bloch-line-bearing Type-II bubble, or when a polarity-inverted labyrinthine state redirects the system into a different compact-domain branch.

At still higher field, the compact domains annihilate. In experiments, Type-II bubbles generally annihilate before Type-I dipole skyrmions. The higher field required to annihilate skyrmions is a phenomenological signature of their topological stability: although both objects are stabilized by the same micromagnetic energy terms, the continuously wound wall of the Type-I skyrmion makes its annihilation pathway more constrained than that of a topologically trivial Type-II bubble.

4.8 Imaging Signatures and Three-Dimensional Structure

4.8.1 What LTEM Contributes. Lorentz transmission electron microscopy is well suited to Fe/Gd because it images magnetic textures in transmission while allowing an applied magnetic field along the beam direction. In the Fresnel imaging mode, domain walls produce bright and dark contrast because the magnetic induction deflects the electron beam. With SITIE reconstruction, a single defocused image can be converted into a projected in-plane magnetic induction map for a sufficiently uniform thin film [59]. This makes LTEM a powerful tool for following field-driven domain evolution in real time.

The strength of LTEM is also its limitation. It is a projection technique. It measures the in-plane magnetic induction integrated through the film thickness, not the full three-dimensional magnetization. As a result, LTEM can identify the outline of a domain and the projected circulation of its wall, but it cannot uniquely determine how the magnetization changes with depth. This ambiguity is not a technical footnote; it is central to Fe/Gd. A Type-II bubble viewed in projection can resemble a more exotic compact texture if the Bloch-line structure and through-thickness wall twist are not known [65].

4.8.2 What SEMPA Adds. Scanning electron microscopy with polarization analysis provides a complementary view. SEMPA measures the vector magnetization near the surface of the sample. In the Fe/Gd multilayers considered here, that surface sensitivity is valuable because dipolar fields are expected to drive the wall toward a Neel-like cap at the top and bottom surfaces, while the interior remains more Bloch-like [16]. SEMPA therefore samples exactly the part of the texture where the three-dimensional twisting is most visible.

By itself, SEMPA is also incomplete. It does not image through the film thickness, and it generally cannot follow the same in situ field sequence as LTEM. It is also sensitive to the domain state that exists near remanence or after sample preparation. Since isolated Type-II bubbles often merge into achiral worm domains near remanence, SEMPA is especially useful for imaging the surface structure of worm and stripe states, while LTEM more naturally follows isolated Type-II bubbles during in situ field sweeps. The value of SEMPA in this chapter is therefore not that it replaces LTEM, but that it anchors the surface boundary condition.

4.8.3 The Paired-Imaging Logic. Skyrmions in Fe/Gd have been imaged with both LTEM and SEMPA. The paired LTEM/SEMPA approach has already been used to identify the hybrid three-dimensional structure of dipole-stabilized skyrmions in Fe/Gd [17]. In that work, LTEM images established the projected induction structure of the domains, SEMPA measured the surface magnetization, and micromagnetic simulations supplied the depth-resolved interpretation. The same logic motivates the rest of this dissertation: if a projected image is ambiguous, compare it with a surface-sensitive vector measurement and with simulations that preserve the full three-dimensional magnetization.

This chapter treats that paired-imaging workflow as precedent for the later analyses. The following chapters apply the same logic to more specific formation pathways and interface-engineering questions, while the baseline classification begins with the common Fe/Gd domains introduced here.

4.9 Using the Zoo in the Following Chapters

The rest of the dissertation uses this baseline taxonomy as a practical guide rather than as a fixed list of idealized states. Ch. V starts from the stripe

and bubble entries in Table 4 and asks how field-driven stripe collapse selects between common compact-domain outcomes. The central issue there is dynamical: nominally similar collapse events can produce different final topologies because the inherited Bloch-line structure, local demagnetizing field, and tilted Zeeman field compete during relaxation.

Later chapters move from this baseline Fe/Gd phenomenology toward less common transition states and interface-engineered textures. Those cases require additional definitions and evidence, so they are introduced in their own chapters rather than folded into the present survey of commonly observed Fe/Gd domains.

4.10 Summary

The Fe/Gd domain zoo, as used in this chapter, is not a list of unrelated magnetic curiosities. It is a compact set of commonly observed textures produced by the same competing energy terms: exchange, perpendicular anisotropy, Zeeman coupling, and long-range dipolar fields. Labyrinthine stripes provide the parent state for field-driven bubble formation. Type-II bubbles preserve a Bloch-line pair and are topologically trivial in two dimensions. Type-I dipole skyrmions have continuous winding and nonzero layer-resolved skyrmion number, while their hybrid wall structure and fractional Hopf-like character describe how that same Type-I object twists through the multilayer thickness.

The experimental lesson is equally important. LTEM, SEMPA, and micromagnetic simulation each answer a different part of the classification problem. LTEM gives projected induction and field-dependent evolution. SEMPA gives surface vector magnetization. Simulation supplies the depth-resolved magnetization needed to connect those measurements. The paired LTEM/SEMPA approach has already demonstrated this logic for the hybrid wall structure of Type-I dipole

skyrmions in Fe/Gd [17]; the remainder of the dissertation uses that established framework as a foundation for studying stripe-collapse pathways, topology selection, and interface-controlled textures.

CHAPTER V

STRIPE COLLAPSE IN FE/GD MULTILAYERS

Publication Note

This chapter is adapted from the manuscript "Experimental Evidence for Mixed-Topology Bubbles Mediating Dipole Skyrmion Formation in Fe/Gd Multilayers." At the time of dissertation preparation, this manuscript was in preparation for publication. J. A. Reddinger performed the LTEM experiments, micromagnetic simulations, domain-tracking analysis (**domain-tracker on GitHub**), and manuscript preparation. W. S. Parker generated initial simulations of stripe collapse. Fe/Gd multilayer sample fabrication was performed by E. E. Fullerton and S. A. Montoya at UCSD Center for Magnetic Memory and Recording. B. J. McMorran supervised the project. The manuscript has been reformatted for inclusion in this dissertation.

Experimental Evidence for Mixed-Topology Bubbles Mediating Dipole Skyrmion Formation in Fe/Gd Multilayers

J. A. Reddinger[1,*], W. S. Parker[1], E. E. Fullerton[2], S. A. Montoya[2], and B. J. McMorran[1]

[1]Department of Physics, University of Oregon, Eugene, OR 97403, USA

[2]Center for Memory and Recording Research, University of California, San Diego, La Jolla, CA 92093, USA

Abstract

Centrosymmetric multilayers provide a route to dipole-stabilized skyrmions whose topology arises from competition among exchange, anisotropy, and long-range dipolar fields rather than from the Dzyaloshinskii-Moriya interaction. In Fe/Gd multilayers, skyrmion lattices are commonly nucleated by collapsing stripe domains, but this process produces a mixture of Type-I dipole skyrmions and Type-II topologically trivial bubbles, indicating that topology selection during collapse is not yet deterministic. Here we combine room-temperature Lorentz transmission electron microscopy (LTEM), single-image transport-of-intensity-equation (SITIE) magnetic induction reconstruction, micromagnetic simulations, and domain tracking to identify the transition pathways that connect stripe collapse to final bubble topology. Experimentally, we observe candidate bubble domains whose projected induction patterns are inconsistent with purely Type-I or Type-II textures and are instead consistent with mixed-topology Type-III bubbles. Simulations show that stripe collapse initially nucleates Type-II bubbles, which subsequently relax either by Bloch-line rotation or through a Type-III intermediate containing a topologically trivial interior and skyrmion-like Néel-cap surface layers. Depth-resolved energetic analysis shows that demagnetizing fields favor Néel-cap expansion, while coupling between Bloch lines and the tilted Zeeman field can stabilize the Type-II-like core or reverse the transition. These results support a mechanism in which mixed-topology bubbles mediate dipole skyrmion formation in Fe/Gd and suggest routes for controlling topology selection in centrosymmetric magnetic multilayers.

5.1 Introduction

Magnetic bubbles were first reported by Bobeck et al. in rare-earth iron garnet films with strong perpendicular magnetic anisotropy [66]. These domains are stabilized by a balance of exchange, anisotropy, and dipolar interactions and can host several distinct domain-wall chirality configurations. The discovery of magnetic skyrmions in bulk MnSi renewed interest in small, circular magnetic domains with nontrivial topology [4]. Their particle-like dynamics and proposed use in racetrack-style devices have made skyrmions a central target for spintronic materials design [7]. Although skyrmions are often associated with chiral magnets in which the Dzyaloshinskii-Moriya interaction fixes the domain-wall handedness, related topological textures can also be stabilized in centrosymmetric systems by dipolar interactions and depth-dependent domain-wall structure.

Achiral centrosymmetric magnets therefore allow skyrmion bubbles and topologically trivial bubbles to coexist under ambient conditions. Fe/Gd multilayers are a model centrosymmetric system capable of hosting stripe domains, Type-I dipole skyrmion bubbles, skyrmion bound pairs, and Type-II topologically trivial bubbles [15, 51]. In this material family, dipole skyrmions can be stabilized at room temperature, driven by spin-orbit torques, and detected through transport signatures associated with field-dependent stripe and skyrmion phases [15, 47, 50]. These textures nucleate from similar parent stripe states and can coexist across broad field ranges, yet nominally similar stripe-collapse events may produce different final bubble topologies [67, 68]. Prior work established Fe/Gd as a platform for dipolar skyrmions and skyrmion lattices, but the intermediate states that determine topology selection during collapse remain less well resolved.

Understanding these intermediate states is essential for deterministic skyrmion generation.

Here we report LTEM evidence for bubble domains in Fe/Gd whose projected magnetic induction is consistent with mixed topology. Because SITIE reconstructs projected in-plane induction rather than layer-resolved magnetization, this evidence must be interpreted together with simulations capable of resolving depth-dependent topology. We therefore place the experimental signatures first and use micromagnetic simulations to identify compatible topology and energetic signatures.

We identify a continuous transition pathway from Type-II trivial bubbles to Type-I dipole skyrmions mediated by a mixed-topology Type-III state, with depth-localized topology change at partial-Bloch-line termini. Simulations reveal two relaxation pathways for frustrated Type-II bubbles: Bloch-line rotation or transition through a metastable Type-III state. The pathway-dependent energy profiles support an interpretation in which competition between local demagnetizing fields and Bloch-line coupling to the tilted Zeeman field favors either continued conversion to Type-I or reversion toward Type-II topology.

5.2 Background

In multilayer materials, out-of-plane magnetic domains are usefully described by their domain walls, where the magnetization reverses between neighboring domains. The domain-wall helicity is the orientation of the in-plane magnetization relative to the domain-wall normal. In multilayer films this helicity is depth dependent: domain walls are approximately Bloch-like near the midplane and acquire Néel caps at the top and bottom surfaces to reduce magnetostatic energy [16, 31]. Neutron scattering measurements in Fe/Gd have directly confirmed that

dipolar skyrmions in this system have hybrid three-dimensional structure with depth-dependent domain-wall character [21]. In the absence of appreciable DMI, clockwise and counterclockwise Bloch walls are nearly degenerate, so helicity can be selected dynamically by local fields and defects rather than fixed by interfacial chirality.

A Bloch line is a topological defect along a domain wall where the Bloch-wall chirality reverses. Type-I bubbles [Fig. 17(a)] have domain-wall magnetization that winds once around the bubble without Bloch lines and therefore carry nonzero skyrmion number in each layer. Type-II bubbles [Fig. 17(b)] contain two Bloch lines and have zero net winding [69]. Both Type-I and Type-II bubbles can possess depth-dependent Néel caps, but their two-dimensional topology remains the same through the film thickness: Type-I remains skyrmion-like in every layer, whereas Type-II remains topologically trivial in every layer.

We reserve the term Type-III bubble [Fig. 17(c)] for a more general condition: mixed topology through the film thickness. In this state, interior layers are Type-II-like and topologically trivial, while one or both surface layers have skyrmion-like in-plane winding. The transition between these regions is bounded by partial Bloch lines whose termini are Bloch-point-like regions; the continuum model resolves the extended wall structure but not an atomic singular core. Thus, an ordinary Type-II bubble with flux-closure Néel caps is not automatically Type-III; the defining feature is a layer-resolved change in winding/topological character. Type-III and related mixed-depth bubble structures have been predicted in simulations and observed in other materials, but their role during stripe collapse in Fe/Gd multilayers has not been established [17, 54, 70, 71].

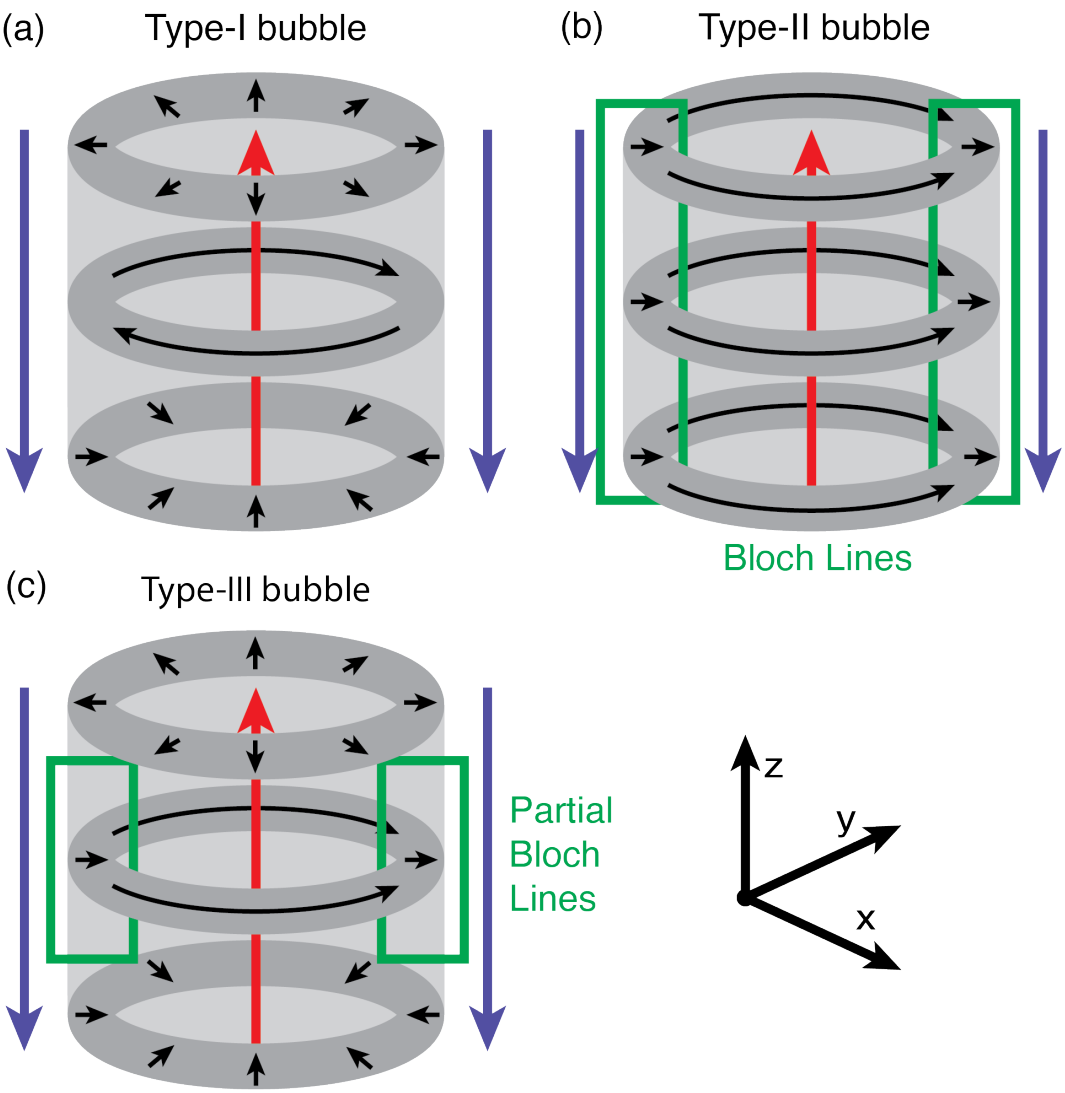

Figure 17. Bubble topology and domain-wall structure in centrosymmetric Fe/Gd multilayers. (a) Type-I dipole skyrmion bubble with continuous in-plane winding through the film thickness. (b) Type-II topologically trivial bubble containing a pair of Bloch lines. (c) Mixed-topology Type-III bubble with a Type-II-like interior and skyrmion-like Néel-cap surface layers. Red and blue indicate opposite out-of-plane magnetization directions.

This distinction is closely related to the biskyrmion/Type-II-bubble debate in LTEM. Loudon et al. [65] showed that projected LTEM images previously identified as biskyrmions in centrosymmetric magnets can be reproduced by tilted Type-II bubbles and emphasized that TIE reconstructs projected magnetic flux density rather than the three-dimensional magnetization. Their simulations also showed strong through-thickness variation, including Type-II-like structure near the midplane and radial flux-closure structure near the surfaces. This precedent identifies the central ambiguity addressed here: projected induction can make a conventional Type-II bubble, a mixed-depth Type-III bubble, or a biskyrmion-like projection appear similar unless the projection is compared with layer-resolved simulations and with the formation pathway.

LTEM is sensitive to the projected in-plane induction of the film. It encodes induction patterns associated with Bloch-line structure and domain-wall winding, but it does not by itself reconstruct the full three-dimensional magnetization. This ambiguity motivates the combined experimental-simulation approach used here. The experimental identification of mixed-topology bubbles in this work is therefore cautious: SITIE identifies projected signatures consistent with a Type-III state, and micromagnetic simulations provide the depth-resolved interpretation.

5.3 Methods

5.3.1 Experimental Methods. Room-temperature LTEM measurements were performed using an FEI ThemIS at the National Center for Electron Microscopy. The sample was a [Fe(0.34 nm)/Gd(0.40 nm)] $\times$ 120 multilayer film, corresponding to a nominal magnetic thickness of 88.8 nm based on calibrated growth rates. Phase-contrast Fresnel images were acquired with a defocus of 500 μm while sweeping the objective-lens excitation from +5% to -

5%, corresponding to an estimated out-of-plane field on the order of 1 kOe at the sample.

The sample holder was tilted by 4° from the electron-beam direction to introduce an in-plane field component and frustrate parallel stripe domains. The field sweep drove transitions from positive saturation, through stripe states, and into negative-field bubble states. Fresnel images were processed with a bandpass filter to reduce shot noise and background. Magnetic induction vector fields were reconstructed from the processed Fresnel images using the single-image transport-of-intensity equation, following prior LTEM/SITIE approaches for skyrmionic materials and domain-wall chirality mapping [59, 61].

Regions of interest containing closed bubbles with projected winding number $W = 0$ were extracted from the magnetic-induction images using a multi-scale ridge-detection implementation based on curvilinear-structure detection [72, 73]. Only bubbles that could be traced to a stripe at, or immediately adjacent to, the same position before nucleation were included in the analyzed population. Gaps between detected ridge segments were closed by projecting from the segment endpoints.

Within this eligible $W = 0$ population, bubble categorization was performed manually using a single projected-induction criterion. Bubbles without a discernible core induction stream between the two Bloch-lines were classified as Type-II, whereas bubbles containing a discernible stream connecting those vertices were classified as candidate Type-III. Projected area, eccentricity, overall induction magnitude, and helicity profile were not used to assign the classifications and were evaluated only after classification.

Some candidate Type-III bubbles had weak contrast relative to the surrounding magnetic texture, which is physically consistent with a mixed-depth wall: LTEM phase contrast is governed by the projected in-plane induction, and replacing part of a through-thickness Bloch-like wall with skyrmion-like surface winding reduces the effective Bloch-wall contribution to the projection [16, 59, 61, 65, 74]. Because LTEM/SITIE measures projected magnetic induction, the core-stream classification is treated as an experimental signature consistent with mixed topology rather than as a direct measurement of three-dimensional topology.

Accordingly, the experimental classifications are used as projected signatures and are interpreted through comparison with simulated Type-I, Type-II, and Type-III induction maps rather than as standalone measurements of layer-resolved skyrmion number.

5.3.2 Computational Methods. Micromagnetic simulations were performed using MuMax3, which numerically solves the Landau-Lifshitz-Gilbert equation [35]. Material parameters were taken from Montoya et al. [15] and are representative of Fe/Gd multilayer thin films. The simulated geometry was a 2.048 μm $\times$ 2.048 μm $\times$ 80 nm slab formed from 3.2nm $\times$ 3.2nm $\times$ 3.2nm voxels with periodic boundary conditions in the film plane and random initial magnetization. Stripe collapse was induced by sweeping an external magnetic field from 330 mT to -300 mT, tilted 4° from the film normal. To prepare the stripe state, the field was swept from 330 mT to -200 mT in 5 mT increments using energy minimization, followed by 20 ns of LLG evolution at -200 mT. From this state, a time-dependent field sweep from -200 mT to -300 mT was applied over 100 ns. Magnetization and energy components were recorded every 0.25 ns. The damping was set to

$\alpha = 1$ to suppress precessional ringing and approximate quasi-static relaxation during the field sweep. The same simulation protocol was run with MuMax3's `Temp` parameter set to 0 K and 300 K. The finite-temperature simulations showed the same qualitative pathway structure observed at 0 K, which was subsequently analyzed with the domain-tracking algorithm.

A custom Python Domain Tracker package processed the MuMax3 output and extracted structural and energetic information for each domain. Contours from individual z slices were stitched into three-dimensional Domain objects, linked across time by center-of-mass proximity and intersection-over-union metrics, and classified as stripe domains or Type-I, Type-II, or Type-III bubbles. The resulting domain histories enabled event counting, topology tracking, and depth-resolved energy analysis.

These data provide the temporal and energetic resolution needed to interpret experimentally observed projected induction signatures and to resolve topology changes that are inaccessible to LTEM/SITIE alone.

5.4 Results

5.4.1 Experimental signatures of candidate mixed-topology bubbles.

LTEM Fresnel images acquired during the tilted field sweep show stripe collapse followed by the appearance of isolated bubble domains [Fig. 18(a)]. SITIE reconstruction of the projected induction [Fig. 18(b)] reveals that most bubbles are consistent with conventional Type-I or Type-II textures. Within the stripe-derived $W = 0$ population, however, a subset contains a discernible core induction stream connecting two Bloch-lines. This core stream is the projected criterion used to assign candidate Type-III bubbles. One such domain is marked in Fig. 18(b), and its evolution during stripe collapse is shown in Fig. 18(c)-(f). The montage

shows a frustrated stripe collapsing into an atypical bubble-like structure with two joined vertices, resembling the projected biskyrmion-like contrast discussed in prior LTEM work. The domain wall also exhibits relatively weak projected induction compared with neighboring bubbles, although induction magnitude was not used for classification.

The key experimental observation is therefore not a direct measurement of three-dimensional topological charge, but the appearance of projected induction patterns that cannot be explained cleanly by a purely Type-I or Type-II projected texture. This motivates comparison with simulated projected induction from Type-III bubbles, in which skyrmion-like surface layers coexist with a Type-II-like interior.

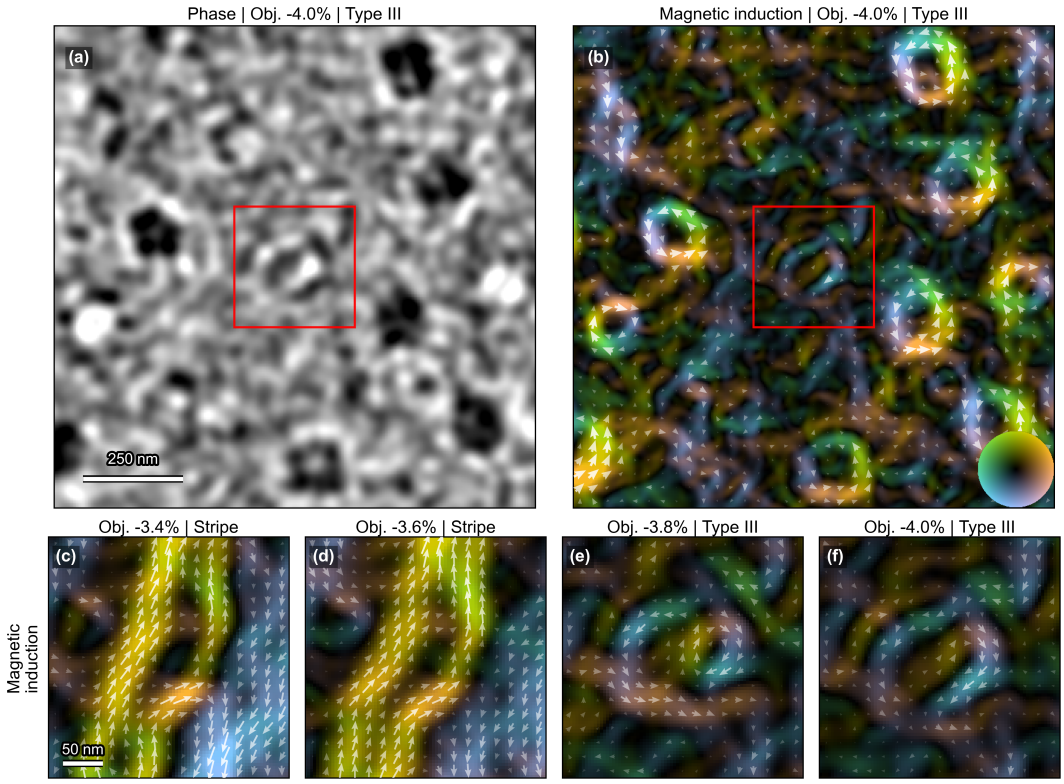

Figure 18. Experimental LTEM/SITIE evidence for candidate mixed-topology bubbles after stripe collapse. (a) Reconstructed phase image and (b) SITIE-reconstructed projected magnetic induction map of magnetic domains after collapse; the red box marks a candidate mixed-topology bubble surrounded by Type-I- and Type-II-like domains. (c)-(f) SITIE induction image series of the boxed region during an objective-lens sweep. The candidate bubble develops a skyrmion-like morphology while preserving a Type-II-like projected induction signature, consistent with a mixed-topology intermediate.

5.4.2 Projected-induction comparison with simulations. In Fig. 19, projected magnetic induction maps of Type-I, Type-II, and candidate Type-III bubbles are compared between experiment and simulation. The Type-I pair shows continuous circulation around the domain wall, while the Type-II pair shows the characteristic projected asymmetry associated with a Bloch-line pair. Within the experimental population of stripe-derived $W = 0$ bubbles, candidate Type-III assignments were based solely on a discernible core induction stream connecting the two Bloch-lines; the corresponding feature is reproduced by simulated Type-III projections. This projected signature does not by itself determine the three-dimensional topology, but it provides the experimental criterion used for comparison with the depth-resolved simulations.

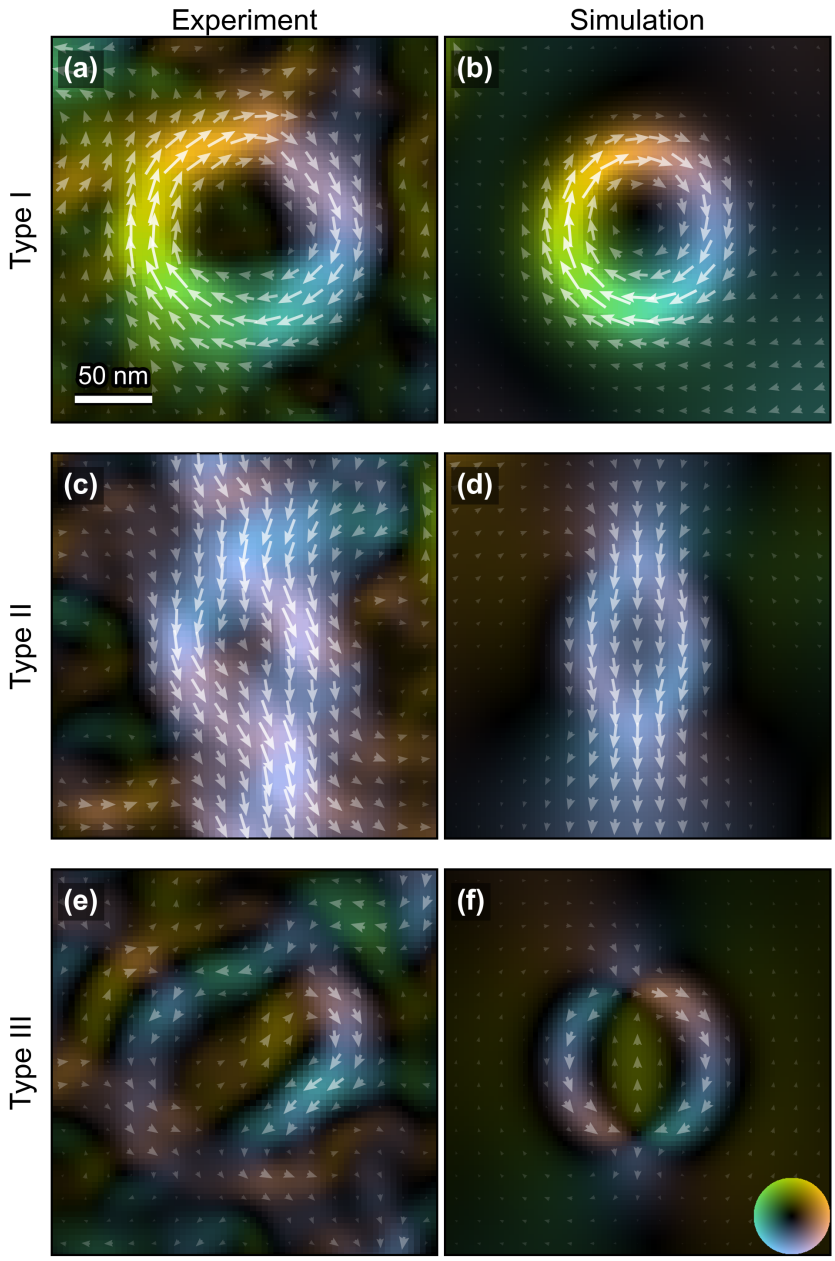

Figure 19. Experimental-simulation comparison of projected induction signatures. Left column: SITIE-reconstructed projected magnetic induction maps assigned to (a) Type-I, (c) Type-II, and (e) candidate Type-III bubbles. Right column: simulated projected magnetic induction for (b) Type-I, (d) Type-II, and (f) Type-III bubbles. The comparison supports interpreting the experimental candidate as consistent with a mixed-topology bubble, while the depth-resolved topology is inferred from simulation.

To determine whether the core-stream-defined populations also differ in other projected properties, we compared the Type-II and candidate Type-III populations using domain-level morphology, projected-induction statistics, and binned helicity profiles. The two populations differ across these properties, and the same relative trends appear in the simulated projected-induction data. These post-classification differences characterize the two experimental populations; the precursor-stripe evolution and comparison with simulated projections provide the model-informed basis for interpreting the core-stream signature as consistent with Type-III topology.

Aggregating over the filtered bubble populations makes these trends clearer. The domain-level histograms contain 14 experimental Type-II and 11 experimental candidate Type-III bubbles, together with 16 simulated Type-II and 7 simulated Type-III bubbles. The pixel- or ridge-point-level histograms contain 1486 experimental Type-II and 1657 experimental candidate Type-III points, together with 1959 simulated Type-II and 945 simulated Type-III points. Fig. 20 shows histograms of ridge and induction properties from experiment and simulation. Although the absolute values differ between experiment and simulation, the relative trends agree: candidate Type-III bubbles are generally larger, less eccentric, and have weaker projected induction than Type-II bubbles. The weaker projected induction is physically consistent with a reduced effective Bloch-wall depth in Type-III bubbles, because LTEM/SITIE measures the through-thickness projected in-plane induction rather than the full three-dimensional magnetization [16, 59, 61, 65, 74].

Treating each unique experimental bubble as one statistical observation, Type-II and candidate Type-III bubbles form distinct populations. Type-II bubbles

had a median projected area of 7.92×10^3 nm^2, median radial distance of 45.5 nm, median eccentricity of 0.736, and a median projected magnetic induction of 0.43 T. Candidate Type-III bubbles had a median projected area of 1.40×10^4 nm^2, median radial distance of 63.7 nm, median eccentricity of 0.678, and a median projected magnetic induction of 0.34 T. Using Mann–Whitney U tests [75] with Benjamini–Hochberg correction [76], the two populations were compared over these four properties. The results confirmed the two populations differ significantly in projected area ($q = 0.003$), radial distance ($q = 3.62 \times 10^{-4}$), and projected magnetic induction ($q = 0.003$). While there was a difference in eccentricity, it was not significant ($q = 0.163$). The joint distributions of projected area, eccentricity, radial distance, and magnetic-induction magnitude also differed significantly between Type-II and candidate Type-III bubbles (energy-distance permutation test on standardized features, $E = 2.36$, $p_{\mathrm{perm}} = 1.0 \times 10^{-4}$; 10,000 permutations) [77]. The domain-wall helicity profiles also differ. The candidate Type-III helicity profile changes more sharply near the Bloch-line position ($\theta = 0$) and remains flatter away from it, like Bloch-type skyrmions. Alternatively, Type-II bubbles are closer to a linearly decreasing helicity, like a uniform magnetization.

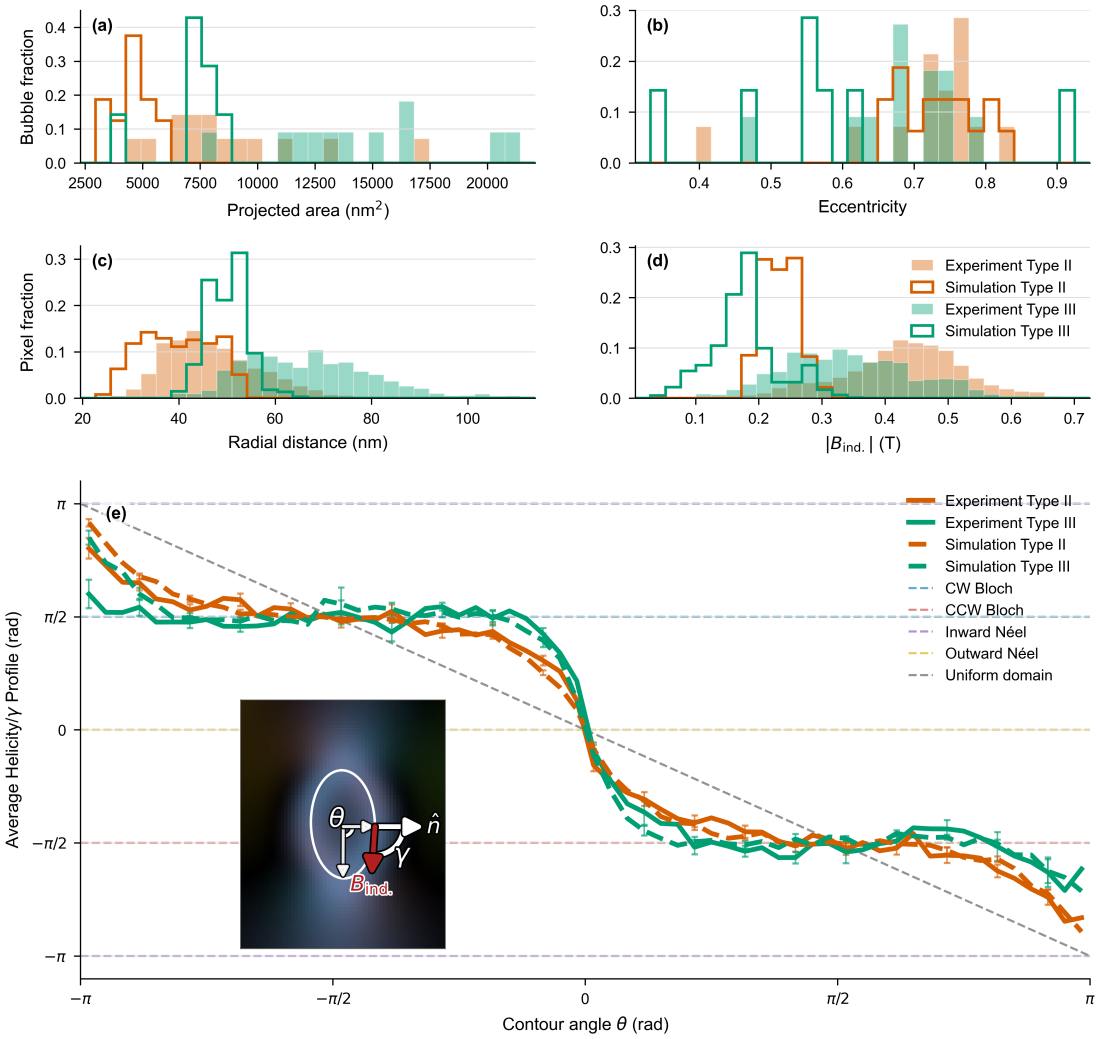

Figure 20. Experimental-simulation property comparison of Type-II and candidate Type-III domains. Domain-level distributions of (a) projected area and (b) eccentricity compare experimental and simulated bubbles. Pixel-level distributions of (c) radial position and (d) projected magnetic induction magnitude characterize the internal induction structure. (e) Binned domain-wall helicity as a function of contour angle for Type-II and candidate Type-III bubbles. The inset defines contour angle as the angle relative to the -y axis and helicity as the angle between the outward domain-wall normal and the local projected magnetic induction.

With the experimental candidates defined by their projected induction signatures, we next ask how such states arise during stripe collapse. The simulations provide the time resolution needed to connect the observed post-collapse textures to the underlying topology-changing pathways.

5.4.3 Simulated stripe collapse nucleates frustrated Type-II bubbles.

In Fig. 21, representative simulated domains are followed after stripe collapse. In the simulations, stripe domains shrink gradually under increasing out-of-plane field until a critical field causes pinch-off. Bloch-line pairs form naturally at the pinch-off points, so the immediate products of stripe collapse are Type-II bubbles that preserve the topology and Bloch-line orientation of the parent stripe. These newly nucleated Type-II bubbles inherit a frustrated orientation relative to the in-plane component of the tilted Zeeman field.

The projected-induction sequences in Fig. 21(a)-(j) show two representative outcomes for frustrated Type-II bubbles. In both cases, a stripe pinches off into a Type-II bubble and then accesses a Type-III state. In one trajectory the Bloch-line pair rotates toward alignment with the tilted field and the bubble returns to Type-II topology; in the other, the surface layers collapse and the bubble converts to a Type-I dipole skyrmion.

The ensemble statistics in Fig. 21(k) and (l) place these representative trajectories in context. Across 48 tracked post-collapse bubbles and 96 classified transition events, Type-II bubbles appear immediately after stripe collapse and are followed by the emergence of Type-III and Type-I states. No direct Type-I/Type-II transitions were observed within the simulated ensemble; topological conversion proceeded through Type-III states.

This sequence is consistent with the experimental observation that anti-aligned stripe collapse produces a mixture of Type-I bubbles, field-aligned Type-II bubbles, and candidate Type-III bubbles. The simulations suggest that the frustrated Bloch-line geometry created at pinch-off is resolved by two competing responses: rotation of the Bloch-line pair or topological transition through a Type-III intermediate.

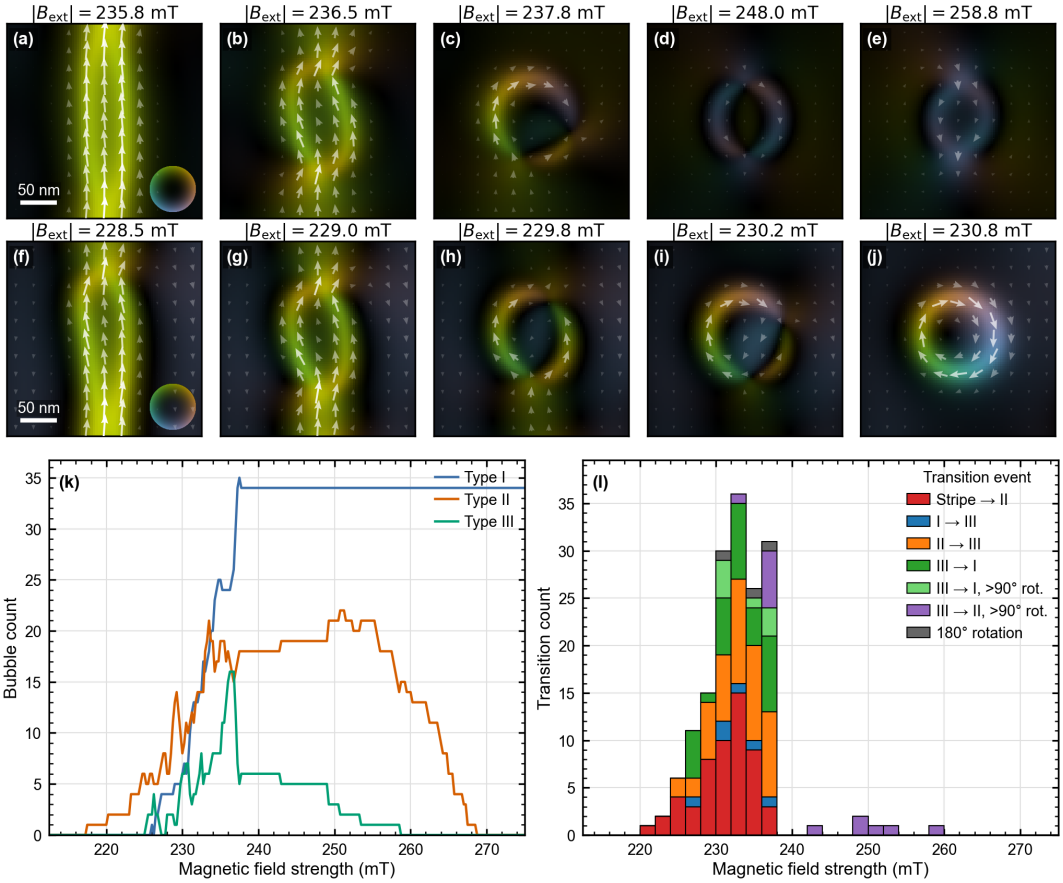

Figure 21. Simulated stripe collapse and transition statistics under a tilted field sweep. (a)-(j) Simulated projected magnetic induction for two representative stripe-collapse trajectories. In both cases, stripe-domain pinch-off nucleates a Type-II bubble that passes through a Type-III state; the upper sequence relaxes back toward Type-II topology after Bloch-line rotation, whereas the lower sequence converts to a Type-I bubble. Field values label each frame. (k) Bubble populations versus applied field show that stripe collapse initially produces Type-II bubbles before Type-III and Type-I states appear. (l) Transition counts between bubble types show no direct Type-I/Type-II conversion, indicating that Type-III bubbles mediate topological transitions in the simulated ensemble.

5.4.4 Type-III bubbles mediate topology change. Figure 22 resolves the Bloch-line dynamics underlying those transition counts. All Type-I-forming events pass through Type-III states, whereas bubbles that remain Type-II either rotate directly or briefly enter Type-III before returning to Type-II topology. The distinction is therefore not whether a Bloch-line pair forms at nucleation, but whether that pair rotates apart or collapses through the surface layers.

Figure 22(a)-(d) shows the three-dimensional Bloch-line structure of a tracked domain that undergoes a 180° rotation. The Bloch-line extent shrinks to a single layer before recovering to approximately half the sample thickness, while the two Bloch lines rotate around the bubble core with different timing. This trajectory approaches, but avoids, the merging event that would annihilate the Bloch lines and complete a Type-I transition. Fig. 22(e) shows the angular displacement between the two Bloch lines: in Type-I-forming trajectories the Bloch lines rapidly merge and annihilate, whereas in trajectories that remain Type-II or Type-III this merging event is avoided. Fig. 22(f) shows the Bloch-line extent after nucleation. Every domain that converts to Type-I undergoes collapse of the surface layers into Néel-closure domains.

These dynamics identify the local competition that controls the relaxation pathway: Bloch-line reorientation preserves a Type-II-like core, whereas Néel-closure-domain expansion drives the system toward mixed topology and, in some cases, Type-I skyrmion formation.

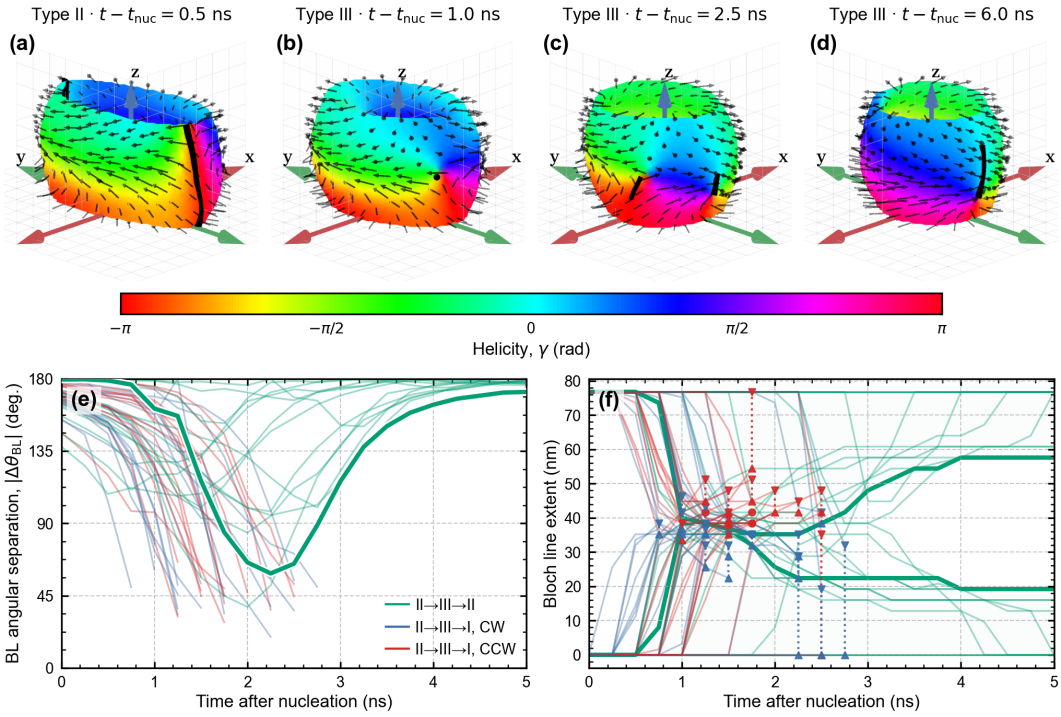

Figure 22. Depth-resolved topology and Bloch-line dynamics during simulated Type-II to Type-III to Type-I relaxation. (a)-(d) Three-dimensional domain-wall renderings of a tracked bubble with Bloch lines marked by black lines and partial-Bloch-line termini (Bloch-point-like regions) marked by dots. After beginning as a Bloch-line-bearing Type-II state, the top and bottom surfaces collapse, reducing the Bloch lines to single-layer points. These points rotate about the bubble core to align with the external magnetic field, after which the Bloch lines partially expand. (e) Bloch-line angular displacement versus time after nucleation. Type-II bubbles avoided transition by realigning before their Bloch lines meet. (f) Bloch-line extent versus time after nucleation, showing partial collapse during Type-III formation. Triangles and dashed lines indicate the final Bloch-line extent at transition to Type-I; circles indicate cases in which the final Bloch-line extent at transition was a single layer.

5.4.5 Energetic signatures of the relaxation pathways. Depth-resolved energy profiles in Fig. 23 probe the energetic competition among exchange, Zeeman, and demagnetizing contributions for bubbles grouped by relaxation pathway. Each bubble's domain-wall energy profile is evaluated 4 ns after nucleation. This snapshot does not by itself give a transition barrier; instead, it provides a layer-resolved comparison of the energetic tendencies that favor persistent Type-II structure, transient Type-III formation, or conversion to Type-I topology after relaxation begins.

Fig. 23(a) shows the Zeeman contribution. Bubbles that retain or recover Type-II-like Bloch-line structure have reduced Zeeman energy where the Bloch lines align favorably with the tilted field. Bubbles that proceed toward Type-I topology lose this favorable Bloch-line contribution as the surface layers collapse and the Bloch lines annihilate.

Fig. 23(b) shows the exchange contribution. Type-II-like domain walls have reduced exchange energy near their Bloch lines, where the domain-wall curvature is reduced. Pathways that access Type-III topology exhibit exchange-energy peaks near the film surfaces, consistent with the rapid magnetization variation at the ends of partial Bloch lines and near Bloch-point-like singularities. Type-I-forming pathways vary more smoothly once the Bloch lines collapse, but they retain higher exchange energy in the Bloch-like core where the domain-wall width is smaller.

Fig. 23(c) shows the demagnetizing contribution. Pathways that access Type-III or Type-I topology lower the demagnetizing energy in the surface layers by forming Néel caps and improving flux closure. Bubbles that remain Type-II retain less favorable surface demagnetizing energy, while Type-II-like and Type-III-

like interiors both carry a demagnetizing-energy cost associated with the Bloch-line-bearing core.

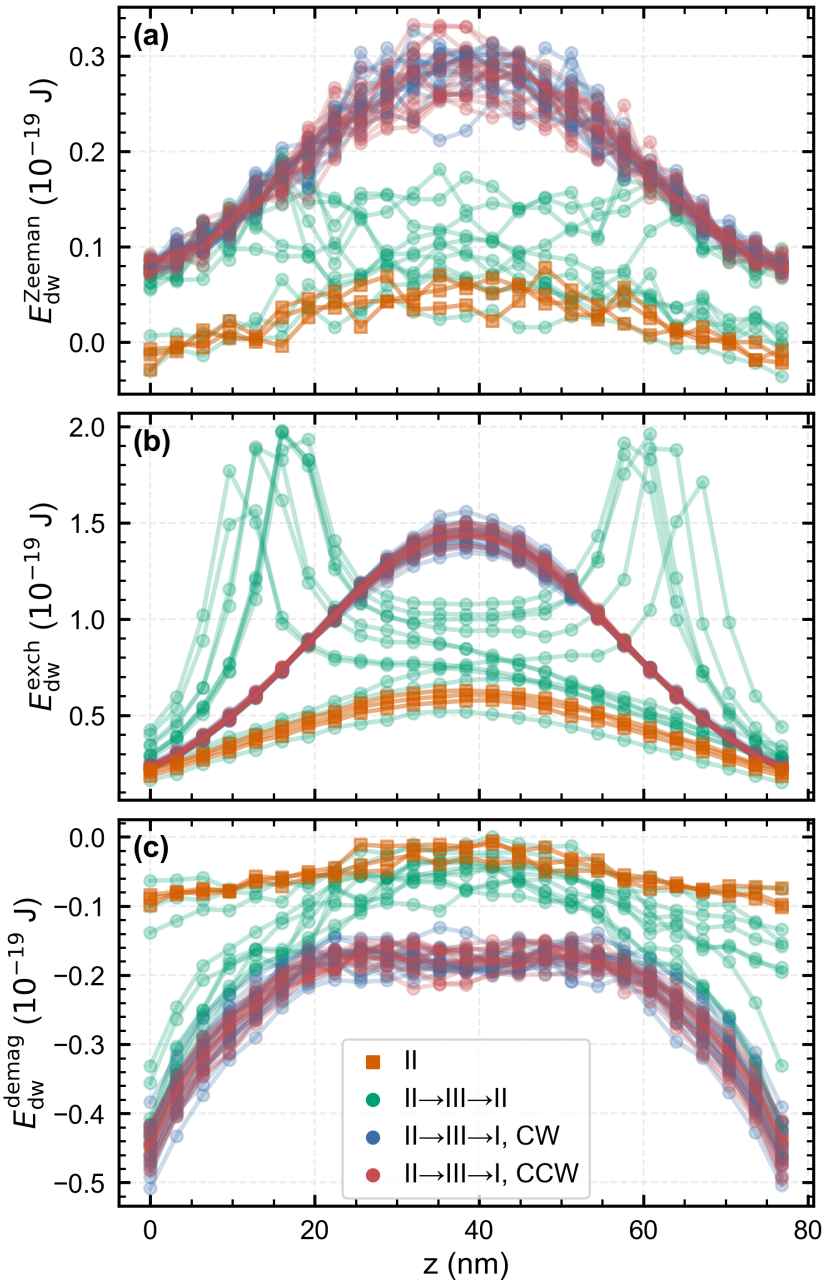

Figure 23. Depth-dependent energetics and topology of simulated bubble domain walls after nucleation. Layer-resolved differences in (a) Zeeman, (b) exchange, and (c) demagnetizing energy are shown for bubbles grouped by relaxation pathway: Type-II bubbles that remain Type-II, Type-II bubbles that become Type-III and return to Type-II, and Type-II bubbles that become Type-III and continue to Type-I with either final chirality. Type-III-forming pathways occupy an energetic middle ground: skyrmion-like surface layers have reduced demagnetizing energy, while the Bloch-line-bearing interior retains favorable coupling to the tilted field. This depth-dependent correlation supports the interpretation of mixed-topology bubbles as intermediates during dipole skyrmion formation.

Together, these trends are consistent with Type-III formation during relaxation. Reduced surface demagnetizing energy accompanies Néel-cap expansion, while exchange-energy peaks accompany the partial-Bloch-line termini required to connect skyrmion-like surface layers to a Type-II-like interior. The mixed topology combines lower surface magnetostatic energy with retained Bloch-line structure in the core. Bubbles that do not access the Type-III pathway instead rotate and exhibit lower Zeeman energy associated with the initially unfavorable Bloch-line orientation. Thus, the energetic correlations connect the projected Type-III-like signatures observed experimentally to the topology-changing pathways resolved in simulation.

The pathway-dependent profiles support a competition between Néel-cap expansion and Bloch-line stabilization. In trajectories where the demagnetizing-energy reduction precedes Bloch-line reorientation, the Bloch lines collapse and the bubble becomes a Type-I dipole skyrmion. Where Bloch-line rotation occurs first, favorable Zeeman coupling accompanies retention of the Type-II-like core and reversion toward Type-II topology.

5.5 Discussion

These results clarify the role of mixed-topology bubbles in Fe/Gd. LTEM/SITIE provides projected induction evidence for bubbles that are not well described as purely Type-I or Type-II textures. Simulations show that such projected signatures are naturally produced by Type-III bubbles, whose surfaces and core carry different two-dimensional topology.

This interpretation also explains why topology selection during stripe collapse appears stochastic in imaging experiments. The relevant control parameters are local and depth dependent: neighboring domains alter the

demagnetizing field, while the tilted external field couples to Bloch-line orientation. Small differences in the local environment can therefore determine whether a newly nucleated Type-II bubble rotates, becomes a Type-I skyrmion through Type-III collapse, or returns to a Type-II state.

Stripe collapse occurs at different nominal applied-field values in experiment and simulation. Plausible sources include finite temperature, uncertainty in material parameters, disorder and pinning, idealized boundary conditions, and uncertainty in the objective-lens field calibration. This offset does not enter the central comparison, which uses the experimental and simulated projected-induction scales and relative topology-dependent trends rather than treating nominal external field as quantitatively matched. It is, however, one possible explanation for the absolute bubble-size discrepancy: because bubble size decreases with increasing out-of-plane field, a higher effective collapse field can produce smaller domains at nucleation without changing the relative distinction between Type-II and candidate Type-III populations.

The biskyrmion/Type-II-bubble debate provides useful context for this interpretation. Loudon et al. [65] showed that counter-rotating projected induction vortices can arise from Type-II bubbles viewed at an angle and that the projected B field need not trace the underlying magnetization. Our results build on that point by separating the projected signature from the depth-resolved topology and from the formation pathway. A Type-III bubble can retain a Type-II-like projected induction component while containing skyrmion-like surface winding and a Type-II-like interior. Thus, projected LTEM/SITIE contrast alone can obscure the distinction between conventional Type-II bubbles and mixed-topology bubbles,

but the ambiguity can be reduced by combining projection comparisons, population statistics, and layer-resolved simulations.

The experimental evidence must be stated cautiously because projected induction does not uniquely determine the full three-dimensional magnetization. Nevertheless, the agreement among SITIE signatures, statistical ridge properties, simulated Type-III projections, and the energetic pathway resolved in simulation supports mixed-topology bubbles as physical intermediates rather than artifacts of a particular simulation protocol.

5.6 Conclusion

We have shown that stripe collapse in Fe/Gd multilayers produces projected induction signatures consistent with mixed-topology Type-III bubbles and that micromagnetic simulations identify a continuous transition pathway from Type-II bubbles to Type-I dipole skyrmions mediated by a mixed-topology Type-III state, with depth-localized topology change at partial-Bloch-line termini. The experimental reconstructions reveal bubble-domain induction signatures that are not well described by purely Type-I or Type-II textures. Simulations show that these states form naturally when Type-II bubbles develop skyrmion-like Néel caps while retaining a topologically trivial core. The pathway-dependent energy profiles support an interpretation in which competition between local demagnetizing fields and Bloch-line Zeeman coupling favors either continued conversion to Type-I or relaxation back toward Type-II topology. These results identify mixed-topology bubbles as experimentally supported intermediates in dipole skyrmion formation and suggest routes for deterministic topology control in centrosymmetric magnetic multilayers.

Acknowledgments

The authors acknowledge Research Advanced Computing Services (RACS) at the University of Oregon for providing computing resources that contributed to the results reported in this chapter. Work performed at the Molecular Foundry was supported by the Office of Science, Office of Basic Energy Sciences, of the U.S. Department of Energy under Contract No. DE-AC02-05CH11231, under user proposal No. MFP-10439. This work was also supported by the National Science Foundation under Grant No. 2105400.

CHAPTER VI

ANTISKYRMIONS IN FE/GD MULTILAYERS

6.1 Motivation: Antiskyrmions and Interface Engineering

The preceding chapters establish a model-informed multimodal probe of three-dimensional structure in multilayer thin films. When applied to centrosymmetric Fe/Gd, it identifies stripe domains, Type-I dipole skyrmions, Type-II bubbles, and a continuous transition pathway mediated by a mixed-topology Type-III state, with depth-localized topology change at partial-Bloch-line termini. The next question is whether the same materials family can also host antiskyrmions: topological solitons whose in-plane winding is opposite that of the skyrmion. Antiskyrmions are usually associated with non-centrosymmetric materials whose crystal symmetry selects anisotropic Dzyaloshinskii-Moriya interaction (DMI), but recent work has shown that dipolar, anisotropy, and interface engineering can also produce antiskyrmion-like textures in multilayer thin films [58, 78].

This chapter combines LTEM, SEMPA, and micromagnetic simulation to identify antiskyrmions and determine how their stability and depth dependence change with material parameters. Heavy-metal insertion layers such as Pt and Ir modify anisotropy, saturation magnetization, spin-orbit coupling, and interfacial DMI, opening a regime in which antiskyrmions coexist with skyrmions and topologically trivial bubbles [58]. The resulting problem is both interpretive and practical: complementary measurements are required to establish topology, while interface engineering is required to select one texture reproducibly. To begin, we apply the established multimodal technique to $[\mathrm{Fe}(0.34\,\mathrm{nm})/\mathrm{Gd}(0.40\,\mathrm{nm})/\mathrm{Pt}(0.05\,\mathrm{nm})/\mathrm{Ir}(0.05\,\mathrm{nm})]_{160}$ samples provided by Eric

Fullerton and Sergio Montoya. The nominal repeated-stack thickness is 134.4 nm, calculated from calibrated growth rates. Micromagnetic simulations then test whether compatible three-dimensional antiskyrmion structures are locally stable across representative material-parameter ranges; they are not used to fit a unique parameter set to the experiment.

6.2 Experimental Observation of Antiskyrmions

6.2.1 LTEM Signatures. Lorentz transmission electron microscopy provides the first experimental evidence. Figure 24 shows representative LTEM images from the Fe/Gd multilayer stack. The top row gives the large-area context: at 0.9% objective-lens excitation, corresponding to an out-of-plane field magnitude of approximately 27.9 mT, stripe domains have collapsed into a population of compact magnetic bubbles. The field points into the image plane ($-\hat{z}$); all images in this chapter are shown looking toward $-\hat{z}$. The red boxes mark regions selected for closer inspection. The middle row shows the corresponding high-magnification Fresnel contrast, while the bottom row shows SITIE-reconstructed projected induction maps.

Localized Fresnel contrast alone does not clearly distinguish Type-I skyrmions, Type-II bubbles, and antiskyrmions. The projected induction does: the candidates contain four Bloch-line features around the wall, two with magnetization directed toward and two away from the core, separated by Bloch-like segments of alternating chirality. This is the characteristic projected signature of an antiskyrmion. LTEM remains depth integrated, but the opposing radial contributions of the surface Néel caps largely cancel in projection, leaving substantial sensitivity to the Bloch-like interior or core. As in Ch. V, LTEM does

not uniquely determine the three-dimensional magnetization, so the assignment is tested below against surface vector magnetometry and simulation.

6.2.2 Antiskyrmion Formation Process. Figure 25 follows a selected region through objective-lens excitations of 0.0%, 0.4%, 0.5%, and 0.9%. Using the calibration of 3100 Oe per 10% excitation and 1 Oe = 0.1 mT in vacuum, these settings correspond to out-of-plane field magnitudes of approximately 0, 12.4, 15.5, and 27.9 mT. Increasing the magnitude of the field into the image plane narrows and fragments the stripes, leaving a mixed population of compact objects that includes antiskyrmions. This behavior extends the collapse phenomenology of Ch. V: local wall orientation and Bloch-line content influence which topology survives pinch-off, while the heavy-metal interfaces enlarge the set of accessible final states.

6.2.3 SEMPA Surface Magnetization. SEMPA provides the complementary measurement needed to move beyond projected induction. For these measurements, the 5-nm Pt cap was removed by Ar-ion milling until Auger spectroscopy detected Fe or Gd, exposing the magnetic multilayer. SEMPA was then acquired at room temperature and remanence in a skyrmion/worm phase. SEMPA is surface-sensitive and directly measures the vector magnetization components at the exposed surface. Figure 26 shows the reconstructed SEMPA magnetization for a region containing antiskyrmions. In the overview map, color encodes the out-of-plane magnetization and arrows indicate the in-plane component. The boxed regions are then decomposed into m_x, m_y, and m_z, followed by a reconstructed vector map.

This representation makes the antiskyrmion assignment more direct. The vector field contains the alternating Bloch-line orientation and associated

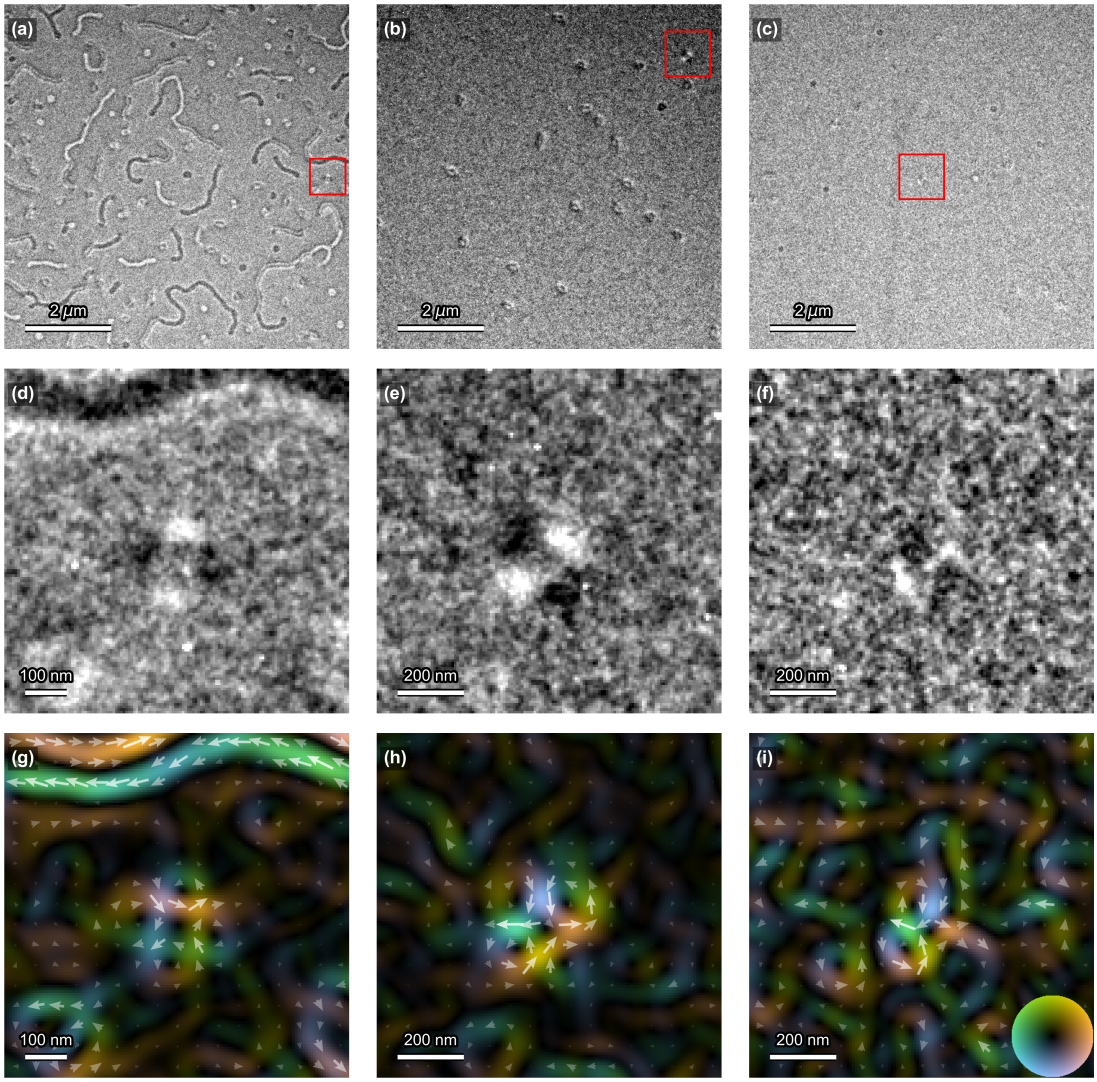

Figure 24. LTEM signatures of antiskyrmions in Fe/Gd-based multilayers. (a)-(c) Fresnel images acquired at 0.9% objective-lens excitation (approximately 27.9 mT, directed into the image plane) and −73.15°C; red boxes mark regions selected for detailed analysis. (d)-(f) Magnified Fresnel contrast from the boxed regions. (g)-(i) SITIE-reconstructed projected induction maps of the same regions. The induction maps reveal localized textures with anisotropic winding, motivating their assignment as antiskyrmions.

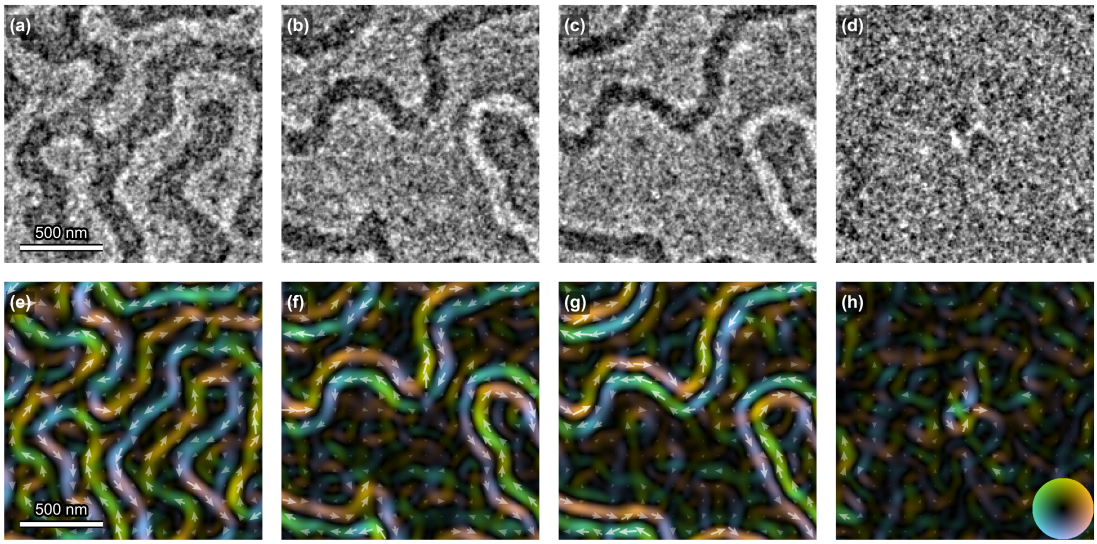

Figure 25. Field evolution of antiskyrmion formation in LTEM. (a)-(d) Fresnel images of the same region at objective-lens excitations of 0.0%, 0.4%, 0.5%, and 0.9%, corresponding to calibrated field magnitudes of approximately 0, 12.4, 15.5, and 27.9 mT, respectively. The nonzero field is directed into the image plane ($-\hat{z}$). (e)-(h) Corresponding SITIE-reconstructed projected induction maps. Increasing field magnitude drives stripe fragmentation and the appearance of localized textures whose induction winding is consistent with antiskyrmions.

winding number expected for an antiskyrmion. In the analysis workflow used to generate Fig. 26, selected domains were cross-checked by two surface-sensitive quantities: the winding of the in-plane magnetization along the domain ridge and the skyrmion number N_{Sk}, obtained by integrating the topological charge density of the reconstructed SEMPA magnetization over the domain. Domains with nonzero N_{Sk} and the expected ridge winding were retained as antiskyrmions. Here, N_{Sk} describes the measured two-dimensional surface texture; it is not a thickness-averaged or layer-resolved value.

The two modalities also reveal a potentially meaningful difference. The LTEM induction maps are approximately circular, whereas the SEMPA domains are more elliptical and devote a larger fraction of the surface wall to radial, Néel-like magnetization. Such a surface reconstruction is consistent with magnetostatic flux closure constrained by exchange continuity. The modalities probe reproducibly prepared ensembles under different conditions: LTEM was acquired under an objective-lens field after cooling, whereas SEMPA was acquired at room temperature and remanence in the skyrmion/worm phase. An isolated compact domain can expand toward remanence without changing its winding provided that it does not merge or annihilate, and the expected demagnetizing-field reconstruction is reproduced by simulation. Repeatable preparation and this understood field evolution therefore support a class-level comparison, but not an assertion that the same object was imaged or that either measurement is layer resolved. The simulations test whether the observed surface/projection difference is plausible in the modeled multilayer.

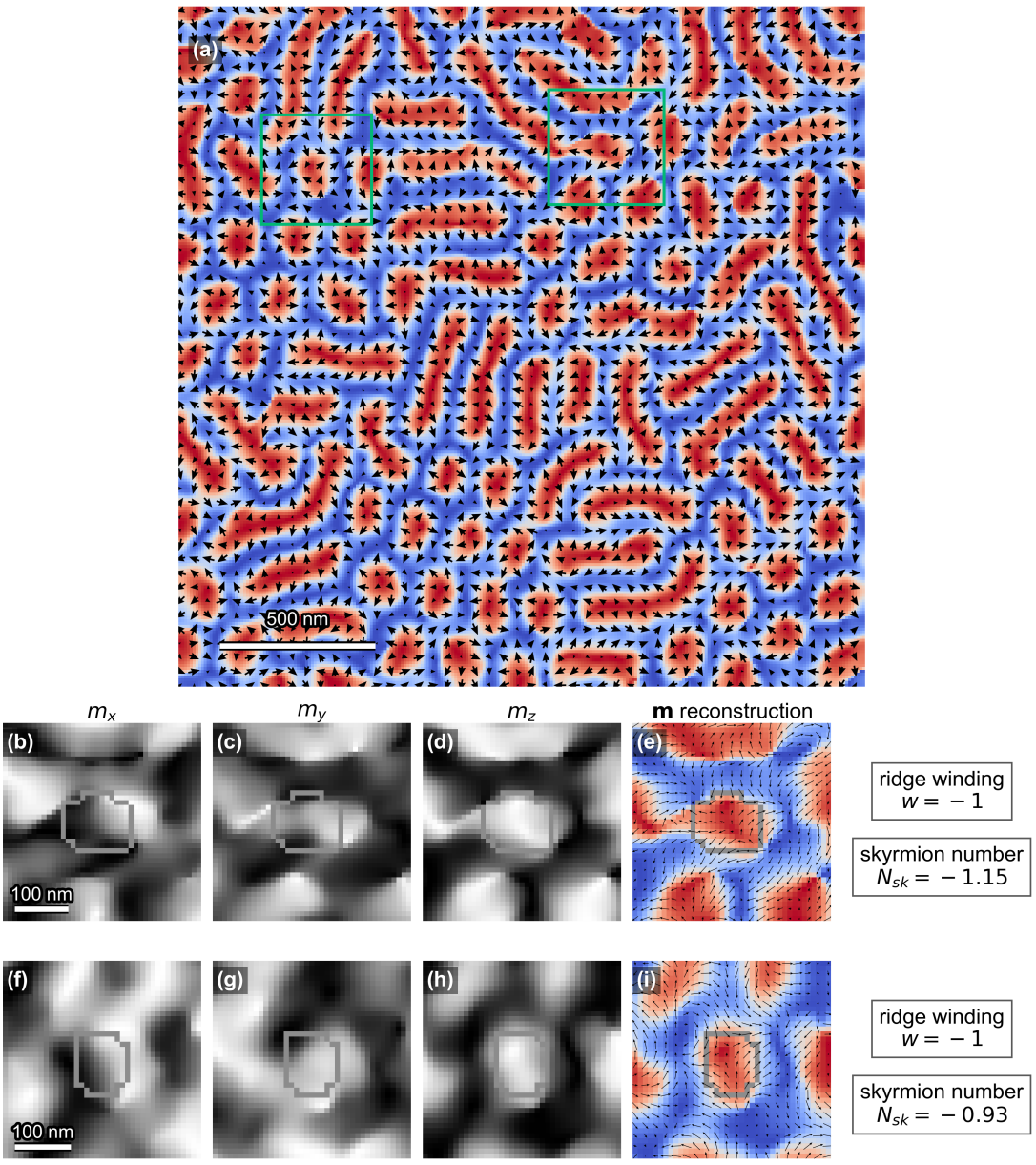

Figure 26. SEMPA vector magnetometry of antiskyrmions. (a) Reconstructed surface magnetization over a large field of view; color indicates m_z and arrows indicate the in-plane magnetization. Boxes mark domains selected for component-level inspection. (b)-(d) and (f)-(h) Cropped m_x, m_y, and m_z components for two representative domains. (e) and (i) Corresponding vector reconstructions. The component maps show a negative domain wall winding consistent with antiskyrmion topology at the sample surface.

6.3 Simulation-Supported Three-Dimensional Structure

The antiskyrmion calculations in this chapter are distinct from the time-dependent stripe-collapse simulations in Ch. V. They use $3 \times 3 \times 3$ nm^3 cubic cells, no periodic boundary conditions, and a Gilbert damping setting of $\alpha = 1$. A prepared state is relaxed with MuMax3's `relax()` energy minimizer. These are deterministic zero-temperature calculations: `relax()` does not include a stochastic thermal field. Unless a parameter is explicitly varied, the material parameters are those in Table 2. The 3-nm cell size is less than half the Fe/Gd exchange length and resolves the extended domain-wall structure, but a fixed-magnitude micromagnetic model does not resolve the atomic core of a Bloch point. Topology-changing cores are therefore mesh regularized, so the relaxed extended texture and basin membership are used here without assigning a quantitative singularity-formation barrier.

The simulations test the local stability of this structure by relaxing an isolated antiskyrmion seed across a grid of fields and material parameters. The resulting basin map is not a spontaneous-nucleation phase diagram: it identifies where a prepared seed is metastable and which competing state is reached when it is not.

Fig. 27 considers a 144-nm simulated film from the discretized thickness series; this model geometry is distinct from the nominal 134.4-nm experimental repeat stack. No depth-uniform antiskyrmion survives in the sampled range. Low DMI favors annihilation to the saturated state. Intermediate DMI occasionally converts the seed to a Néel skyrmion. Notably, it predominantly produces a hybrid topology texture with some skyrmionic and some antiskyrmionic layers. High DMI favors stripes. Field, M_s, and K_{u1} shift these boundaries, showing that the

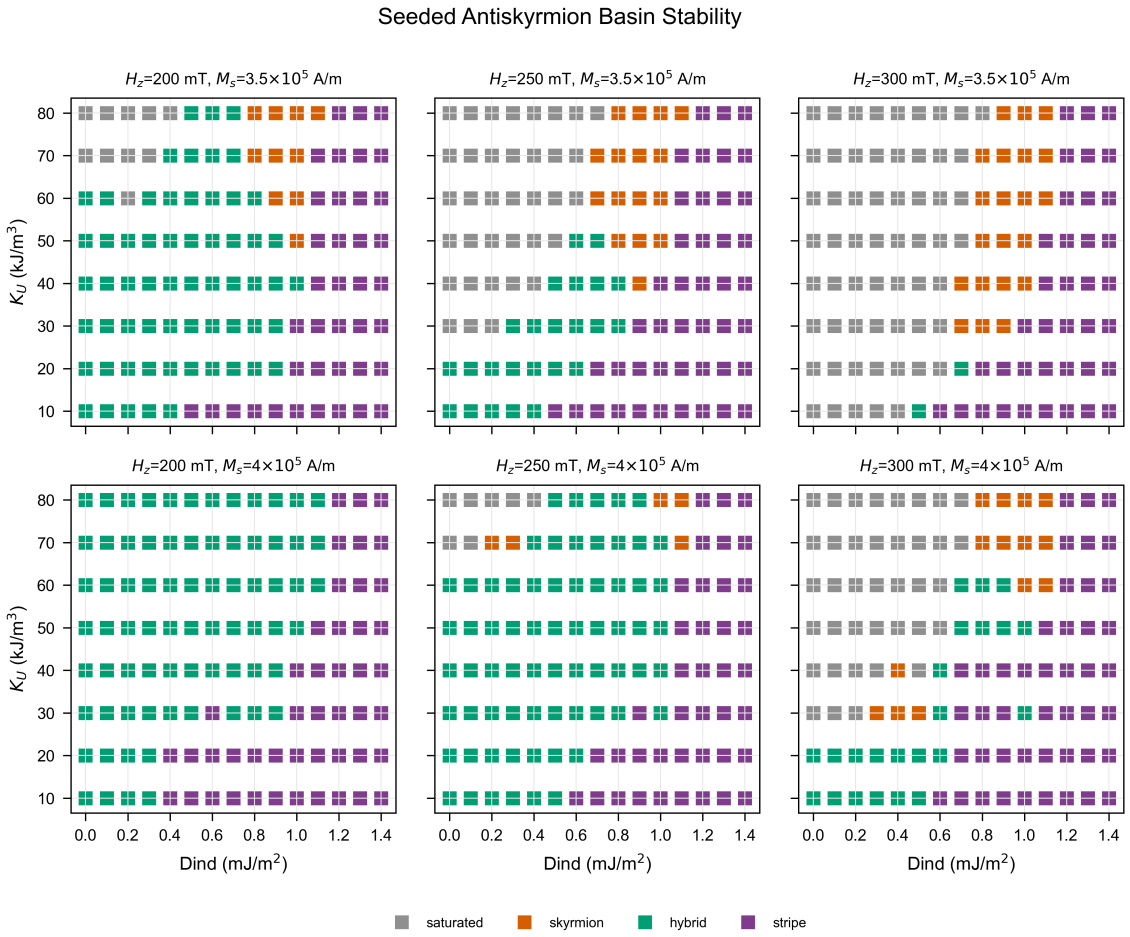

Figure 27. Seeded antiskyrmion basin stability as a function of interfacial DMI, uniaxial anisotropy, applied field, and saturation magnetization. Each colored cell records the relaxed state obtained from an antiskyrmion seed: saturated (gray), skyrmion (orange), hybrid antiskyrmion (green), or stripe (purple). The green region identifies a broad basin in which an antiskyrmion seed relaxes to a hybrid antiskyrmion; it is not a basin of depth-uniform antiskyrmion survival. This suggests experimental results may have featured a hybrid antiskyrmion.

metastability window reflects the full micromagnetic energy balance rather than DMI alone. Within the parameter ranges sampled by this model, DMI produces the largest change in layer-resolved topology; this is a model-scoped sensitivity result, not evidence that DMI is the experimentally dominant interaction or has been independently measured in this stack.

In a thick multilayer, magnetostatic flux closure can make the surface wall differ from the interior. This was shown in the hybrid skyrmion and Type-III bubble cases. It is therefore plausible that an antiskyrmion-like interior may then connect to skyrmion-like surface layers, producing a hybrid antiskyrmion whose layer topology changes along its length. In the continuum simulation, the change occurs at Bloch-point-like termini of partial Bloch lines; the extended defect is resolved, while the atomic singular core is not. An analogous Bloch-point quadrupole has been observed by electron-holographic vector-field tomography in a different material system [38]. Here, this structure remains a simulation-supported interpretation rather than an experimental reconstruction of $\mathbf{m}(x, y, z)$.

Notably, these seeded final-state maps do not show a pure antiskyrmion, yet thickness introduces a second control parameter. Figure 28 isolates its effect at fixed field and material parameters. Pure antiskyrmions occupy the low-DMI portion of the thinnest films, and that stability interval narrows toward $D_{\mathrm{ind}} = 0$ as thickness increases. Above approximately 72 nm, the low-DMI survivor is predominantly hybrid rather than pure. At larger DMI, stripe expansion replaces the compact seed, with the crossover depending strongly on thickness. Thus, reducing the film thickness suppresses the opportunity for opposing skyrmionic surface-closure regions to develop and increases the stability range of a topologically uniform antiskyrmion. At 120 nm, the depth-dependent topology

varies less with changes in DMI and the skyrmion-like surface regions can be tuned to occupy a large or small fraction of the string.

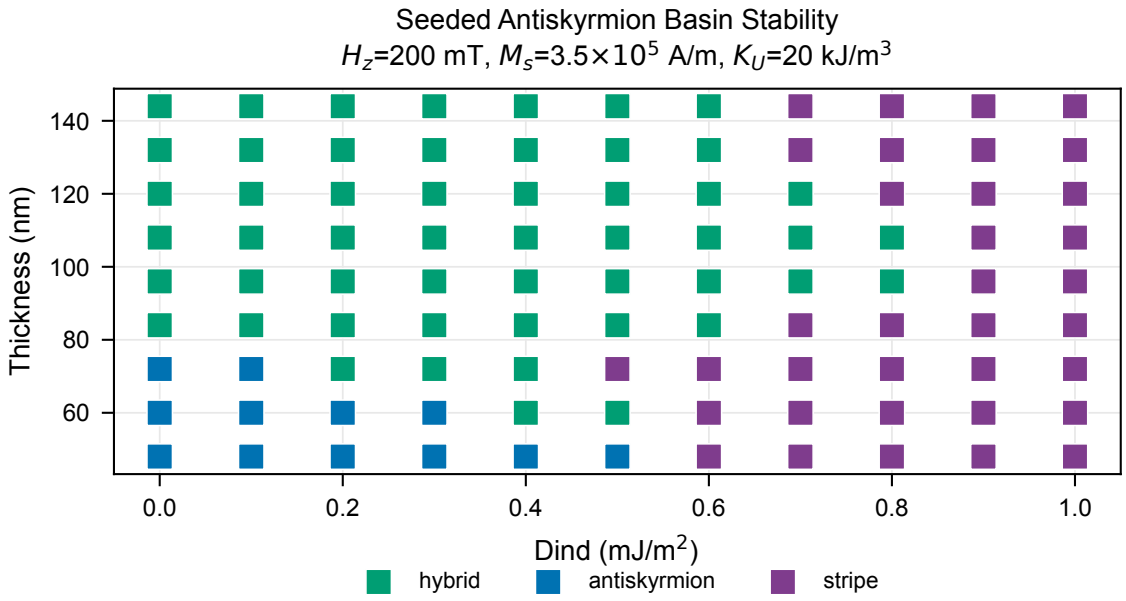

Figure 28. DMI-thickness seeded final-state map obtained by relaxing an antiskyrmion seed at $H_z = 200$ mT, $M_s = 3.5 \times 10^5$ A/m, and $K_{u1} = 20$ kJ/m^3. Blue, green, and purple symbols denote pure antiskyrmion, hybrid antiskyrmion, and stripe final states, respectively. Pure antiskyrmions are favored in thinner films and at low DMI; increasing thickness promotes hybrid reconstruction, while sufficiently large DMI drives stripe expansion.

6.3.1 Hybrid Antiskyrmions and Depth-Dependent Topology.

Figure 29 resolves the hybrid state layer by layer. Within the unhatched compact-state region, the 48-nm film remains nearly uniform with $N_{\mathrm{Sk}}(z) \simeq -1$ throughout the sampled DMI range. At 72 nm and above, skyrmion-like surface regions increasingly surround an antiskyrmion-like interior, and DMI shifts the boundary between these segments. In some cases, skyrmionic caps collapse into antiskyrmions at the surface. At higher DMI, stripe expansion occurs. Hatched columns are stripe final states and are not interpreted as compact-soliton topology.

The 120 nm energy decomposition in Fig. 30 shows the accompanying redistribution of exchange and demagnetization energy through the film. The anisotropy and Zeeman terms also change, but no single component selects the hybrid structure; the moving $N_{\mathrm{Sk}}(z)$ profile is their relaxed compromise.

This section shows that by varying multilayer thickness and DMI strength, Fe/Gd multilayers with heavy metal interfaces may support a rich new class of mixed topology textures. The domain-wall surfaces in Fig. 31 illustrate the corresponding limits: a pure antiskyrmion in a thin film, two hybrid strings, and a Néel skyrmion.

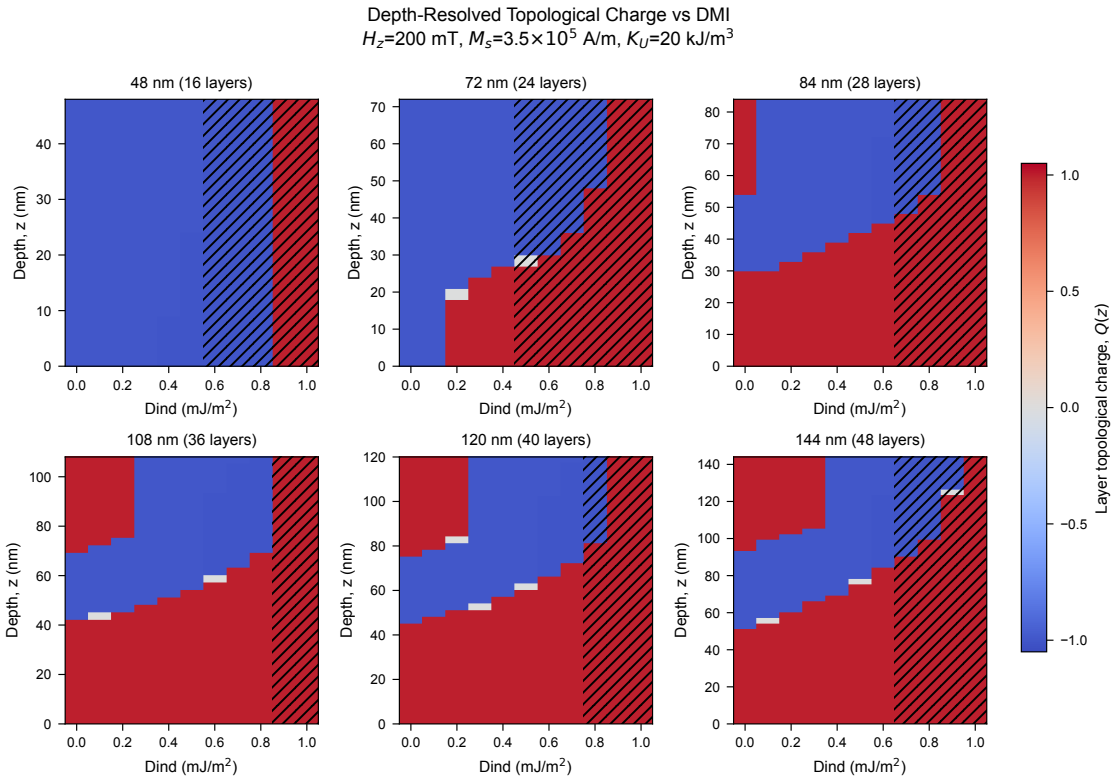

Figure 29. Layer-resolved topological charge $N_{\mathrm{Sk}}(z)$ as a function of interfacial DMI for six film thicknesses at $H_z = 200$ mT, $M_s = 3.5 \times 10^5$ A/m, and $K_{u1} = 20$ kJ/m^3. Blue and red denote antiskyrmion-like $N_{\mathrm{Sk}}(z) \simeq -1$ and skyrmion-like $N_{\mathrm{Sk}}(z) \simeq +1$ layers, respectively; near-white cells have $N_{\mathrm{Sk}}(z) \simeq 0$. Black hatching marks simulations whose final state is a stripe. Thin films favor a uniform antiskyrmion string at low DMI. With increasing thickness, skyrmion-like surface regions surround an antiskyrmion-like interior, and DMI tunes the relative lengths of the two segments.

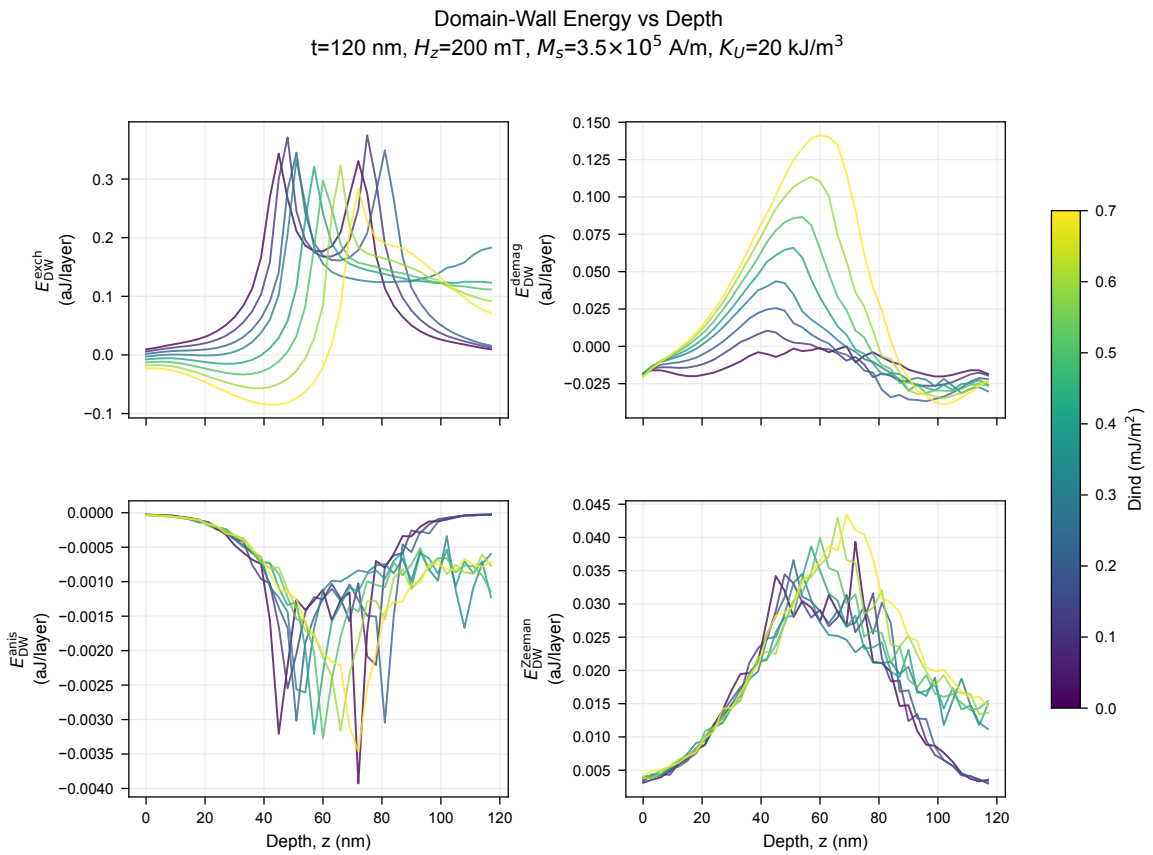

Figure 30. Layer-resolved domain-wall energy contributions for the 120-nm DMI series at $H_z = 200$ mT, $M_s = 3.5 \times 10^5$ A/m, and $K_{u1} = 20$ kJ/m^3. Curves are colored by D_{ind} and show exchange (upper left), demagnetization (upper right), anisotropy (lower left), and Zeeman (lower right) contributions. The coupled displacement of the exchange and demagnetization features tracks the DMI-driven redistribution of skyrmion-like and antiskyrmion-like segments through the thickness.

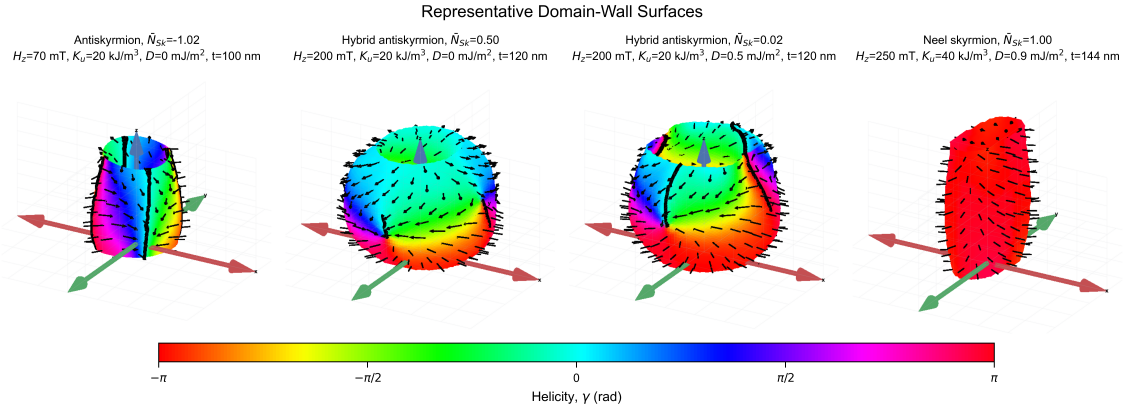

Figure 31. Representative relaxed domain-wall surfaces from the seeded simulations. Surface color gives the local helicity γ, and black arrows show the in-plane magnetization along the wall. From left to right: a pure antiskyrmion in a 100-nm film at $D_{\mathrm{ind}} = 0$; two 120-nm hybrid antiskyrmions with different thickness-averaged skyrmion number, $\bar{N}_{\mathrm{sk}} = -0.50$ and 0.02; and a Néel skyrmion in a 144-nm film at larger DMI and field. The hybrid surfaces visualize the continuous depth-dependent reconstruction hidden by any single two-dimensional slice.

6.3.2 Transport Implications of Hybrid Topology.

Beyond their scientific value as interesting magnetic textures, hybrid topologies can significantly impact transport properties. Opposite-sign $N_{\mathrm{Sk}}(z)$ segments generate opposite-sign emergent magnetic fields in an adiabatic picture. A nearly balanced hybrid string can therefore reduce the thickness-integrated topological Hall response, while DMI shifts the balance point and may tune its magnitude or sign [11, 38, 41, 42]. The same cancellation can reduce the effective gyrovector relevant to transverse skyrmion motion. Quantitative predictions require more than an arithmetic average of $N_{\mathrm{Sk}}(z)$, particularly in ferrimagnetic Fe/Gd: conductivity, spin polarization, and sublattice response can all vary through the thickness. The present simulations therefore identify a control mechanism, not yet a transport measurement. Existing Fe/Gd Hall measurements provide a natural test once the magnetic phase and depth-dependent emergent field can be modeled together [49, 50].

6.4 Outlook: Heavy-Metal Interfaces and DMI

The antiskyrmion results motivate a more deliberate program of interface engineering in Fe/Gd. Heavy-metal layers provide a practical route for varying interfacial DMI, spin-orbit coupling, magnetic anisotropy, and saturation magnetization. The experimental challenge is that all of these quantities depend on growth mode, intermixing, roughness, and magnetic coupling at the relevant interfaces. The presence of antiskyrmions in Fe/Gd/Pt/Ir multilayers is therefore not the endpoint; it is the evidence that the interface parameter space is rich enough to be worth controlling.

The seed-stability calculations should also be treated cautiously because they do not reproduce the experimental formation pathway. In separate stripe collapse simulations, an achiral stripe can form an antiskyrmion-like state,

whereas the experimental LTEM sequence begins from a chiral stripe texture. This mismatch may indicate that the present micromagnetic model omits an interface-specific ingredient. PtIr insertion likely cannot be captured by a single isotropic DMI constant: growth-induced anisotropy, local alloying, roughness, crystallographic texture, or spatially varying spin-orbit coupling could bias the parent-stripe helicity and alter its collapse. These possibilities do not invalidate the metastable basin identified here, but they limit what the model can say about nucleation.

The next step is to connect antiskyrmion stability to independently measured interface structure. Spin-polarized low energy electron microscopy (SPLEEM) offers the surface-sensitive magnetic and structural measurements needed to establish how Fe, Gd, Pt, Ir, and related heavy-metal layers form, reconstruct, and couple magnetically. Future work on the simpler Gd/Fe/W(110) bilayer system therefore serves as a baseline for future measurements on Fe/Gd/heavy-metal stacks. A controlled epitaxial model system will not reproduce every detail of an amorphous multilayer, but it can isolate the microscopic ingredients that are hidden in the full multilayer stack.

From a materials-design perspective, the target is no longer simply "make antiskyrmions." The target is to tune the balance among skyrmions, antiskyrmions, and trivial bubbles by design. LTEM can map the field and temperature range of compact textures, SEMPA or SPLEEM can measure surface winding and interface magnetism, and simulations can connect those observations to depth-dependent topology and emergent transport. This is the route toward deterministic antiskyrmion-hosting devices.

6.5 Conclusion

LTEM and SEMPA establish antiskyrmion character in reproducibly prepared ensembles under complementary temperature and field conditions, but do not reconstruct the same object through its thickness. Seeded simulations predict that thick films predominantly support hybrid strings, whereas thinner films can retain a depth-uniform antiskyrmion. Within the hybrid regime, DMI moves the boundary between opposite-sign topological segments in the sampled model, providing a possible means to reduce the thickness-integrated skyrmion Hall response.

CHAPTER VII

CONCLUSION

7.1 A Model-Informed Multimodal Probe

This dissertation developed and applied a model-informed multimodal approach to three-dimensional magnetic textures in Fe/Gd-based multilayers. Lorentz transmission electron microscopy (LTEM) measures thickness-projected magnetic induction and efficiently follows domains through changes in field and temperature. Scanning electron microscopy with polarization analysis (SEMPA) provides the complementary near-surface vector magnetization, while micromagnetic simulation supplies a depth-resolved magnetization field that can be projected into each experimental observable. Used together, these techniques distinguish structures that can appear similar in any single two-dimensional image and connect observed contrast to the competition among exchange, anisotropy, Zeeman, demagnetizing, and interfacial energies.

This approach was used first to organize the Fe/Gd domain zoo and its field-history-dependent transformations. LTEM resolved extended stripes, worms, Type-II bubbles, Type-I dipole skyrmions, and antiskyrmion-like textures, while SEMPA constrained the surface winding of selected phases. The comparison was extended from compact bubbles to worm domains, whose projected chirality reversals and surface Néel closure are consistent with walls that retain part of the depth-dependent structure of the bubbles from which they formed. In multilayers containing Pt and Ir insertion layers, LTEM and SEMPA further established antiskyrmion character in reproducibly prepared ensembles. These measurements do not image the same individual object or the same field and temperature

conditions, but their complementary sensitivities substantially narrow the set of compatible magnetic structures.

The resulting interpretation remains model informed rather than tomographic. Simulation supplies a physically compatible three-dimensional magnetization, not a unique inversion of the experimental measurements. This distinction is important because projected induction, surface magnetization, and a simulated depth profile constrain different parts of the same physical problem. The strength of the method is therefore not a claim of direct three-dimensional imaging, but its ability to combine complementary evidence rapidly across many domains and magnetic states.

7.2 Depth-Dependent Topology

The results show that topology in a thick magnetic multilayer cannot always be represented by a single two-dimensional label. Long-range demagnetizing fields favor flux-closure structures near the surfaces, while the film interior can retain Bloch-like walls and a different layer-resolved winding. This produces magnetic strings whose topology changes along the film normal and whose surface, interior, and thickness projection can consequently suggest different classifications.

The clearest example is the Type-III bubble identified in the stripe-collapse simulations. Its interior remains Type-II-like and contains a Bloch-line pair, whereas skyrmion-like Néel-cap regions form near the surfaces. Partial Bloch lines connect these regions, and their Bloch-point-like termini localize the change in layer topology. Experimental LTEM/SITIE reconstructions reveal candidate bubbles with projected-induction signatures consistent with this mixed-depth state, although the projection alone does not determine the layer-resolved topology.

The antiskyrmion simulations extend this principle to strings containing opposite signs of layer-resolved skyrmion number. Thin modeled films can retain a nearly depth-uniform antiskyrmion, whereas thicker films preferentially reconstruct into hybrid strings with an antiskyrmion-like interior and skyrmion-like surface regions. Within the sampled model, film thickness determines whether this reconstruction can develop, and interfacial Dzyaloshinskii–Moriya interaction (DMI) shifts the boundary between the skyrmion-like and antiskyrmion-like segments. The experimentally observed antiskyrmions may therefore have been hybrid objects, but LTEM and SEMPA do not directly reconstruct the required $\mathbf{m}(x, y, z)$ field. If verified, such opposite-sign topological segments would also provide a means to reduce or tune the thickness-integrated emergent field and transverse soliton motion.

Together, the worm, Type-III-bubble, and hybrid-antiskyrmion results establish depth as an active degree of freedom. Surface closure is not merely a small correction to an otherwise two-dimensional soliton; it can change the topology assigned to individual layers, create localized topological defects, and alter both transformation pathways and expected transport behavior.

7.3 Type-III Relaxation During Stripe Collapse

The central dynamical result of this dissertation is a continuous pathway from a Type-II bubble to a Type-I dipole skyrmion through a mixed-topology Type-III state. In the simulations, parallel-stripe pinch-off first creates a frustrated Type-II bubble whose Bloch-line pair is inherited from the parent stripe. The bubble then relaxes by two competing responses. Rotation of the Bloch-line pair into favorable alignment with the in-plane component of the tilted field preserves, or restores, Type-II topology. Alternatively, expansion of the surface Néel-closure

regions shortens the Bloch lines, creates a Type-III bubble, and can culminate in merger and annihilation of the partial Bloch lines to produce a Type-I dipole skyrmion. A Type-III bubble can also return to Type-II if Bloch-line rotation wins before annihilation is complete.

No direct Type-I–Type-II transition was observed in the tracked simulation ensemble; every Type-I-forming trajectory passed through a Type-III state. The depth-resolved energy profiles explain why this intermediate is accessible. Néel-cap expansion lowers the surface demagnetizing energy, while the remaining Type-II-like interior retains favorable Zeeman coupling between its Bloch lines and the tilted field. Exchange-energy peaks accompany the rapid magnetization variation near partial-Bloch-line termini. Type-III bubbles therefore occupy an energetic and topological middle ground between Bloch-line rotation and complete Bloch-line annihilation.

This competition explains why nominally similar stripe-collapse events can produce Type-I skyrmions, Type-II bubbles, or long-lived mixed-topology states. Small changes in the local demagnetizing field, disorder, pinning, and Bloch-line orientation can select different relaxation pathways. The candidate Type-III signatures observed by LTEM, their agreement with simulated projections, and the simulated pathway statistics together support mixed topology as a physical intermediate in dipole-skyrmion formation rather than as a purely numerical construction.

7.4 Future Work

The highest-priority test of these conclusions is a full three-dimensional reconstruction of the magnetization of individual domains. Vector ptycho-tomography could directly recover $\mathbf{m}(x, y, z)$, while holographic vector-field electron

tomography provides a complementary reconstruction of the magnetic induction [38, 53, 79, 80]. Applied to field-prepared Fe/Gd samples, these measurements could determine whether candidate Type-III bubbles contain a Type-II-like interior and skyrmion-like surface layers, locate the proposed partial-Bloch-line termini, and test whether experimentally observed antiskyrmions are depth uniform or hybrid. Reconstructing the full magnetization under a controlled and reproducible magnetic history would provide the most direct verification of the simulation-supported results in this dissertation.

Direct three-dimensional imaging does not eliminate the value of the multimodal method. Tomography requires many projections, careful alignment, stable magnetic states, and substantial reconstruction time. LTEM, SEMPA, and simulation remain useful when time efficiency, minimal processing, and broad sampling of a phase space are the priorities. In particular, LTEM/SITIE can screen field and temperature evolution with comparatively simple processing, and the multimodal workflow can identify the small number of states for which a resource-intensive three-dimensional reconstruction is most informative. The two approaches are therefore complementary: the multimodal probe provides throughput and discovery, while tomography provides decisive verification of selected structures.

A second direction is deliberate control of the Pt and Ir interfaces. Varying Pt and Ir thickness, insertion order, repetition frequency, and intermixing should make it possible to tune the magnitude and possibly the sign of the net interfacial DMI while independently tracking changes in anisotropy, saturation magnetization, and spin–orbit coupling. The goal is to connect measured interface structure and magnetic parameters to the stability ranges of skyrmions, antiskyrmions, and hybrid strings. Such a study should combine direct measurements of DMI

and anisotropy with LTEM phase mapping and simulations that reproduce the experimental stripe-collapse pathway, rather than representing the Pt/Ir insertion by a single unconstrained isotropic DMI parameter.

Preliminary spin-polarized low-energy electron microscopy (SPLEEM) measurements made parallel to this work provide an initial reference for that interface-engineering program, although they were not developed into a standalone dissertation chapter. Fe/W(110) shows strong in-plane magnetic contrast with nearly antiparallel domain populations; in the 4 atomic layer film, the wall structure also varies with wall orientation. Pure Gd/W(110) shows structural and ordinary-reflectivity signatures but no robust spin asymmetry in the measured energy window, a probe-selective null result that should not be interpreted as evidence that the film is nonmagnetic. When Gd is deposited on Fe/W(110), the spin-dependent reflectivity changes in amplitude, line shape, and energy dependence without the clean sign inversion expected from a separately dominant Gd channel. These initial results are consistent with an Fe- or interface-derived reflectivity channel modified by Fe–Gd coupling, although direct sensitivity to the buried Fe layer has not been excluded.

Extending this SPLEEM program to stepwise Fe/Gd/Pt/Ir model stacks would connect growth, reconstruction, spin-dependent reflectivity, and interface magnetism to the DMI-controlled textures observed in full multilayers. In combination with direct three-dimensional reconstruction and the higher-throughput multimodal workflow, these measurements offer a route from identifying mixed-topology states to selecting them through interface design.

Bibliography

[1] IEEE International Roadmap for Devices and Systems. Beyond CMOS and emerging materials integration. Technical report, Institute of Electrical and Electronics Engineers, 2023. URL `https://irds.ieee.org/beyond-cmos/`.

[2] Arman Shehabi, Alexandra Newkirk, Sarah J. Smith, Andrew Hubbard, and Nuoa Lei. 2024 United States Data Center Energy Usage Report. Technical report, Lawrence Berkeley National Laboratory, 2024. URL `https://escholarship.org/uc/item/32d6m0d1`.

[3] Stuart S. P. Parkin, Masamitsu Hayashi, and Luc Thomas. Magnetic Domain-Wall Racetrack Memory. *Science*, 320(5873):190–194, April 2008. ISSN 0036-8075, 1095-9203. doi: 10.1126/science.1145799.

[4] S. Mühlbauer, B. Binz, F. Jonietz, C. Pfleiderer, A. Rosch, A. Neubauer, R. Georgii, and P. Böni. Skyrmion Lattice in a Chiral Magnet. *Science*, 323(5916):915–919, February 2009. ISSN 0036-8075, 1095-9203. doi: 10.1126/science.1166767.

[5] X. Z. Yu, Y. Onose, N. Kanazawa, J. H. Park, J. H. Han, Y. Matsui, N. Nagaosa, and Y. Tokura. Real-space observation of a two-dimensional skyrmion crystal. *Nature*, 465(7300):901–904, June 2010. ISSN 0028-0836, 1476-4687. doi: 10.1038/nature09124.

[6] T.H.R. Skyrme. A unified field theory of mesons and baryons. *Nuclear Physics*, 31:556–569, March 1962. ISSN 00295582. doi: 10.1016/0029-5582(62)90775-7.

[7] Albert Fert, Vincent Cros, and João Sampaio. Skyrmions on the track. *Nature Nanotechnology*, 8(3):152–156, March 2013. ISSN 1748-3387, 1748-3395. doi: 10.1038/nnano.2013.29.

[8] Giovanni Finocchio, Felix Büttner, Riccardo Tomasello, Mario Carpentieri, and Mathias Kläui. Magnetic skyrmions: from fundamental to applications. *Journal of Physics D: Applied Physics*, 49(42):423001, October 2016. ISSN 0022-3727, 1361-6463. doi: 10.1088/0022-3727/49/42/423001.

[9] Albert Fert, Nicolas Reyren, and Vincent Cros. Magnetic skyrmions: advances in physics and potential applications. *Nature Reviews Materials*, 2(7):17031, June 2017. ISSN 2058-8437. doi: 10.1038/natrevmats.2017.31.

[10] Soong-Geun Je, Hee-Sung Han, Se Kwon Kim, Sergio A. Montoya, Weilun Chao, Ik-Sun Hong, Eric E. Fullerton, Ki-Suk Lee, Kyung-Jin Lee, Mi-Young Im, and Jung-Il Hong. Direct Demonstration of Topological Stability of Magnetic Skyrmions *via* Topology Manipulation. *ACS Nano*, 14(3):3251–3258, March 2020. ISSN 1936-0851, 1936-086X. doi: 10.1021/acsnano.9b08699.

[11] Naoto Nagaosa and Yoshinori Tokura. Topological properties and dynamics of magnetic skyrmions. *Nature Nanotechnology*, 8(12):899–911, December 2013. ISSN 1748-3387, 1748-3395. doi: 10.1038/nnano.2013.243.

[12] U. K. Rößler, A. N. Bogdanov, and C. Pfleiderer. Spontaneous skyrmion ground states in magnetic metals. *Nature*, 442(7104):797–801, August 2006. ISSN 0028-0836. doi: 10.1038/nature05056. 00308.

[13] C. Moreau-Luchaire, C. Moutafis, N. Reyren, J. Sampaio, C. A. F. Vaz, N. Van Horne, K. Bouzehouane, K. Garcia, C. Deranlot, P. Warnicke,

P. Wohlhüter, J.-M. George, M. Weigand, J. Raabe, V. Cros, and A. Fert. Additive interfacial chiral interaction in multilayers for stabilization of small individual skyrmions at room temperature. *Nature Nanotechnology*, 11(5): 444–448, May 2016. ISSN 1748-3387, 1748-3395. doi: 10.1038/nnano.2015.313.

[14] Wanjun Jiang, Pramey Upadhyaya, Wei Zhang, Guoqiang Yu, M. Benjamin Jungfleisch, Frank Y. Fradin, John E. Pearson, Yaroslav Tserkovnyak, Kang L. Wang, Olle Heinonen, Suzanne G. E. te Velthuis, and Axel Hoffmann. Blowing magnetic skyrmion bubbles. *Science*, 349(6245):283–286, July 2015. ISSN 0036-8075, 1095-9203. doi: 10.1126/science.aaa1442.

[15] S. A. Montoya, S. Couture, J. J. Chess, J. C. T. Lee, N. Kent, D. Henze, S. K. Sinha, M.-Y. Im, S. D. Kevan, P. Fischer, B. J. McMorran, V. Lomakin, S. Roy, and E. E. Fullerton. Tailoring magnetic energies to form dipole skyrmions and skyrmion lattices. *Physical Review B*, 95(2):024415, January 2017. ISSN 2469-9950, 2469-9969. doi: 10.1103/PhysRevB.95.024415.

[16] Ivan Lemesh and Geoffrey S. D. Beach. Twisted domain walls and skyrmions in perpendicularly magnetized multilayers. *Physical Review B*, 98(10):104402, September 2018. ISSN 2469-9950, 2469-9969. doi: 10.1103/PhysRevB.98.104402.

[17] W. S. Parker, J. Reddinger, R. Moraski, E. E. Fullerton, S. A. Montoya, and B. J. McMorran. Real space imaging of dipole-stabilized hybrid skyrmions in magnetic multilayer thin films. *Physical Review B*, 112(9):094415, September 2025. ISSN 2469-9950, 2469-9969. doi: 10.1103/zlzp-chdg.

[18] Kyung Mee Song, Jae-Seung Jeong, Biao Pan, Xichao Zhang, Jing Xia, Sun Kyung Cha, Tae-Eon Park, Kwangsu Kim, Simone Finizio, Joerg Raabe,

Joonyeon Chang, Yan Zhou, Weisheng Zhao, Wang Kang, Hyunsu Ju, and Seonghoon Woo. Magnetic skyrmion artificial synapse for neuromorphic computing, 2019. URL https://arxiv.org/abs/1907.00957.

[19] Daniele Pinna, George Bourianoff, and Karin Everschor-Sitte. Reservoir computing with random skyrmion textures, 2018. URL https://arxiv.org/abs/1811.12623.

[20] Y. B. Li, Z. R. Wang, R. Midya, Q. F. Xia, and J. J. Yang. Review of memristor devices in neuromorphic computing: materials sciences and device challenges. *Journal of Physics D-Applied Physics*, 51(50):503002, December 2018. ISSN 0022-3727. doi: 10.1088/1361-6463/aade3f.

[21] W. L. N. C. Liyanage, Nan Tang, Lizabeth Quigley, Julie A. Borchers, Alexander J. Grutter, Brian B. Maranville, Sunil K. Sinha, Nicolas Reyren, Sergio A. Montoya, Eric E. Fullerton, Lisa DeBeer-Schmitt, and Dustin A. Gilbert. Three-dimensional structure of hybrid magnetic skyrmions determined by neutron scattering. *Physical Review B*, 107(18):184412, May 2023. ISSN 2469-9950, 2469-9969. doi: 10.1103/PhysRevB.107.184412.

[22] Hendrika Johanna van Leeuwen. Problèmes de la théorie èlectronique du magnétisme. *Journal de Physique et le Radium*, 2(12):361–377, 1921. doi: 10.1051/jphysrad:01921002012036100. URL https://doi.org/10.1051/jphysrad:01921002012036100.

[23] Felix Bloch. Über die Quantenmechanik der Elektronen in Kristallgittern. *Zeitschrift für Physik*, 52:555–600, 1929. doi: 10.1007/BF01339455.

[24] Charles Kittel. *Introduction to Solid State Physics*. Wiley, Hoboken, NJ, 8th edition edition, November 2004. ISBN 978-0-471-41526-8.

[25] J. C. Slater. Theory of Ferromagnetism. Lowest Energy Levels. *Physical Review*, 52(3):198–214, 1937. doi: 10.1103/PhysRev.52.198.

[26] E. C. Stoner. Collective electron ferromagnetism. *Proceedings of the Royal Society of London. Series A, Mathematical and Physical Sciences*, 165(922): 372–414, 1938. doi: 10.1098/rspa.1938.0066.

[27] X. Qian and W. Hübner. First principles calculation of structural and magnetic properties for Fe monolayers and bilayers on W(110). *Physical Review B*, 60(23):16192–16197, 1999. doi: 10.1103/PhysRevB.60.16192.

[28] Tobias Schickling, Jörg Bünemann, Florian Gebhard, and Lilia Boeri. Quasiparticle bands and structural phase transition of iron from Gutzwiller density-functional theory. *Physical Review B*, 93(20):205151, 2016. doi: 10.1103/PhysRevB.93.205151.

[29] C. Santos, W. Nolting, and V. Eyert. Ferromagnetism and temperature-dependent electronic structure of hcp gadolinium. *Physical Review B*, 69(21): 214412, 2004. doi: 10.1103/PhysRevB.69.214412.

[30] A. V. Fedorov, T. Valla, F. Liu, P. D. Johnson, M. Weinert, and P. B. Allen. Spin-resolved photoemission study of photohole lifetimes in ferromagnetic gadolinium. *Physical Review B*, 65(21):212409, 2002. doi: 10.1103/PhysRevB.65.212409.

[31] Alex Hubert and Rudolf Schäfer. *Magnetic domains: the analysis of magnetic microstructures*. Springer, 1998. ISBN 978-3-540-64108-7.

[32] André Thiaville, José Miguel García, Rok Dittrich, Jacques Miltat, and Thomas Schrefl. Micromagnetic study of Bloch-point-mediated vortex core reversal. *Physical Review B*, 67(9):094410, March 2003. doi: 10.1103/PhysRevB.67.094410.

[33] Tôru Moriya. Anisotropic Superexchange Interaction and Weak Ferromagnetism. *Physical Review*, 120(1):91–98, October 1960. ISSN 0031-899X. doi: 10.1103/PhysRev.120.91.

[34] Tôru Moriya. New Mechanism of Anisotropic Superexchange Interaction. *Physical Review Letters*, 4(5):228–230, March 1960. ISSN 0031-9007. doi: 10.1103/PhysRevLett.4.228.

[35] Arne Vansteenkiste, Jonathan Leliaert, Mykola Dvornik, Mathias Helsen, Felipe Garcia-Sanchez, and Bartel Van Waeyenberge. The design and verification of MuMax3. *AIP Advances*, 4(10):107133, October 2014. ISSN 2158-3226. doi: 10.1063/1.4899186.

[36] M. Lakshmanan. The fascinating world of the Landau–Lifshitz–Gilbert equation: an overview. *Philosophical Transactions of the Royal Society A: Mathematical, Physical and Engineering Sciences*, 369(1939):1280–1300, March 2011. doi: 10.1098/rsta.2010.0319.

[37] F. Tejo, R. Hernández Heredero, O. Chubykalo-Fesenko, and K. Y. Guslienko. The Bloch point 3D topological charge induced by the magnetostatic interaction. *Scientific Reports*, 11(1):21714, November 2021. ISSN 2045-2322. doi: 10.1038/s41598-021-01175-9.

[38] Fehmi Sami Yasin, Jan Masell, Yoshio Takahashi, Tetsuya Akashi, Norio Baba, Kosuke Karube, Daisuke Shindo, Takahisa Arima, Yasujiro Taguchi, Yoshinori Tokura, Toshiaki Tanigaki, and Xiuzhen Yu. Bloch Point Quadrupole Constituting Hybrid Topological Strings Revealed with Electron Holographic Vector Field Tomography. *Advanced Materials*, 36(16):2311737, April 2024. ISSN 0935-9648, 1521-4095. doi: 10.1002/adma.202311737.

[39] Hans-Benjamin Braun. Topological effects in nanomagnetism: from superparamagnetism to chiral quantum solitons. *Advances in Physics*, 61(1): 1–116, February 2012. ISSN 0001-8732, 1460-6976. doi: 10.1080/00018732.2012.663070.

[40] R. Rajaraman. *Solitons and instantons: an introduction to solitons and instantons in quantum field theory*. North-Holland Pub. Co. ; sole distributors for the USA and Canada, Elsevier Science Pub. Co, Amsterdam ; New York : New York, N.Y, 1982. ISBN 978-0-444-86229-7.

[41] A. Neubauer, C. Pfleiderer, B. Binz, A. Rosch, R. Ritz, P. G. Niklowitz, and P. Böni. Topological Hall Effect in the A Phase of MnSi. *Physical Review Letters*, 102(18):186602, May 2009. doi: 10.1103/PhysRevLett.102.186602. 00228.

[42] T. Schulz, R. Ritz, A. Bauer, M. Halder, M. Wagner, C. Franz, C. Pfleiderer, K. Everschor, M. Garst, and A. Rosch. Emergent electrodynamics of skyrmions in a chiral magnet. *Nature Physics*, 8(4):301–304, April 2012. ISSN 1745-2473. doi: 10.1038/nphys2231. 00130.

[43] Kai Litzius, Ivan Lemesh, Benjamin Krüger, Pedram Bassirian, Lucas Caretta, Kornel Richter, Felix Büttner, Koji Sato, Oleg A. Tretiakov, Johannes Förster,

Robert M. Reeve, Markus Weigand, Iuliia Bykova, Hermann Stoll, Gisela Schütz, Geoffrey S. D. Beach, and Mathias Kläui. Skyrmion Hall effect revealed by direct time-resolved X-ray microscopy. *Nature Physics*, 13(2): 170–175, February 2017. ISSN 1745-2473, 1745-2481. doi: 10.1038/nphys4000.

[44] Max T. Birch, Ilya Belopolski, Yukako Fujishiro, Minoru Kawamura, Akiko Kikkawa, Yasujiro Taguchi, Max Hirschberger, Naoto Nagaosa, and Yoshinori Tokura. Dynamic transition and Galilean relativity of current-driven skyrmions. *Nature*, 633(8030):554–559, September 2024. ISSN 0028-0836, 1476-4687. doi: 10.1038/s41586-024-07859-2.

[45] Julian Hintermayr, Aladin Ullrich, and Manfred Albrecht. Structure and magnetic properties of ferrimagnetic [Gd/Fe] n multilayer and Gd x Fe100− x thin films. *AIP Advances*, 11(9):095214, September 2021. ISSN 2158-3226. doi: 10.1063/5.0057667.

[46] C. Xu, T. A. Ostler, and R. W. Chantrell. Thermally induced magnetization switching in Gd/Fe multilayers. *Physical Review B*, 93(5):054302, February 2016. ISSN 2469-9950, 2469-9969. doi: 10.1103/PhysRevB.93.054302.

[47] Sergio A. Montoya, Robert Tolley, Ian Gilbert, Soong-Geun Je, Mi-Young Im, and Eric E. Fullerton. Spin-orbit torque induced dipole skyrmion motion at room temperature. *Physical Review B*, 98(10):104432, September 2018. ISSN 2469-9950, 2469-9969. doi: 10.1103/PhysRevB.98.104432.

[48] Ryan D. Desautels, Lisa DeBeer-Schmitt, Sergio A. Montoya, Julie A. Borchers, Soong-Geun Je, Nan Tang, Mi-Young Im, Michael R. Fitzsimmons, Eric E. Fullerton, and Dustin A. Gilbert. Realization of ordered magnetic

skyrmions in thin films at ambient conditions. *Physical Review Materials*, 3 (10):104406, October 2019. ISSN 2475-9953. doi: 10.1103/PhysRevMaterials.3.104406.

[49] Ahmad Us Saleheen, Arnab Singh, David Raftrey, Mike A. Brozius, Margaret R. McCarter, Zoey Tumbleson, Mi-Young Im, Sergio A. Montoya, Eric E. Fullerton, Peter Fischer, Stephen D. Kevan, Sujoy Roy, and Sophie A. Morley. Multimodal correlative study of Hall transport and magnetic phases in Fe/Gd multilayer systems. *Applied Physics Letters*, 126(14):142401, April 2025. ISSN 0003-6951, 1077-3118. doi: 10.1063/5.0239472.

[50] Sergio A. Montoya, Marko V. Lubarda, and Vitaliy Lomakin. Transport properties of dipole skyrmions in amorphous Fe/Gd multilayers. *Communications Physics*, 5(1):293, November 2022. ISSN 2399-3650. doi: 10.1038/s42005-022-01073-0.

[51] J. C. T Lee, J. J. Chess, S. A. Montoya, X. Shi, N. Tamura, S. K. Mishra, P. Fischer, B. J. McMorran, S. K. Sinha, E. E. Fullerton, S. D. Kevan, and S. Roy. Synthesizing skyrmion bound pairs in Fe-Gd thin films. *Applied Physics Letters*, 109(2):022402, July 2016. ISSN 0003-6951, 1077-3118. doi: 10.1063/1.4955462.

[52] Andrew Ducharme, William Parker, Fehmi Sami Yasin, Xiuzhen Yu, and Benjamin McMorran. Lorentz Scanning Transmission Electron Microscopy Holography (LSTEMH) Measurement of Domain Walls in Fe/Gd Multilayers. *Microscopy and Microanalysis*, 30(Supplement_1):ozae044.510, July 2024. ISSN 1431-9276, 1435-8115. doi: 10.1093/mam/ozae044.510.

[53] I. Binnie, H. Fang, B. Shearer, A. Grafov, N. Jenkins, Y. Shao, C. O'Leary, Y. Liao, T. Feggeler, A. Oh, S. Yazdi, J. Zou, B. Wang, E-E. Cating, S. A. Montoya, D. Shapiro, J. Miao, H. C. Kapteyn, and M. M. Murnane. 3D Imaging of Complex Skyrmion and Hopf Topologies in an Extended Sample. arXiv preprint arXiv:2606.27365v1, June 2026. URL `https://arxiv.org/abs/2606.27365v1`. Submitted 25 June 2026.

[54] W. S. Parker, J. A. Reddinger, and B. J. McMorran. Hybrid skyrmions in magnetic multilayer thin films are half-integer hopfions. *Physical Review B*, 110(22):224420, December 2024. ISSN 2469-9950, 2469-9969. doi: 10.1103/PhysRevB.110.224420.

[55] Roberto Moreno, Paula G. Bercoff, Unai Atxitia, Richard F. L. Evans, and Oksana Chubykalo-Fesenko. Temperature dependence of exchange stiffness and energy barrier in compensated ferrimagnets. *Physical Review B*, 111(18): 184416, May 2025. doi: 10.1103/PhysRevB.111.184416.

[56] Se Kwon Kim and Oleg Tchernyshyov. Pinning of a Bloch point by an atomic lattice. *Physical Review B*, 88(17):174402, November 2013. doi: 10.1103/PhysRevB.88.174402.

[57] G. Chen, J. Zhu, A. Quesada, J. Li, A. T. N'Diaye, Y. Huo, T. P. Ma, Y. Chen, H. Y. Kwon, C. Won, Z. Q. Qiu, A. K. Schmid, and Y. Z. Wu. Novel Chiral Magnetic Domain Wall Structure in Fe / Ni / Cu (001) Films. *Physical Review Letters*, 110(17):177204, April 2013. ISSN 0031-9007, 1079-7114. doi: 10.1103/PhysRevLett.110.177204.

[58] Michael Heigl, Sabri Koraltan, Marek Vaňatka, Robert Kraft, Claas Abert, Christoph Vogler, Anna Semisalova, Ping Che, Aladin Ullrich, Timo Schmidt,

Julian Hintermayr, Dirk Grundler, Michael Farle, Michal Urbánek, Dieter Suess, and Manfred Albrecht. Dipolar-stabilized first and second-order antiskyrmions in ferrimagnetic multilayers. *Nature Communications*, 12(1): 2611, May 2021. ISSN 2041-1723. doi: 10.1038/s41467-021-22600-7.

[59] Jordan J. Chess, Sergio A. Montoya, Tyler R. Harvey, Colin Ophus, Simon Couture, Vitaliy Lomakin, Eric E. Fullerton, and Benjamin J. McMorran. Streamlined approach to mapping the magnetic induction of skyrmionic materials. *Ultramicroscopy*, 177:78–83, June 2017. ISSN 03043991. doi: 10.1016/j.ultramic.2017.02.004.

[60] William S. Parker. ltempy: Python tools for Lorentz transmission electron microscopy analysis and visualization, 2024. Unpublished Python software package.

[61] Jordan J. Chess, Sergio A. Montoya, Eric E. Fullerton, and Benjamin J. McMorran. Determination of domain wall chirality using *in situ* Lorentz transmission electron microscopy. *AIP Advances*, 7(5):056807, May 2017. ISSN 2158-3226. doi: 10.1063/1.4977500.

[62] M. R. Scheinfein, J. Unguris, M. H. Kelley, D. T. Pierce, and R. J. Celotta. Scanning electron microscopy with polarization analysis (SEMPA). *Review of Scientific Instruments*, 61(10):2501–2527, 1990. ISSN 00346748. doi: 10.1063/1.1141908. 00212.

[63] Teruo Kohashi. Spin-Polarized Scanning Electron Microscopy. In *Advances in Imaging and Electron Physics*, volume 187, pages 83–125. Elsevier, 2015. ISBN 978-0-12-802255-9. doi: 10.1016/bs.aiep.2014.11.001.

[64] Gary Bradski. The opencv library. *Dr. Dobb's Journal of Software Tools*, 25 (11):120–125, 2000.

[65] James C. Loudon, Alison C. Twitchett-Harrison, David Cortés-Ortuño, Max T. Birch, Luke A. Turnbull, Aleš Štefančič, Feodor Y. Ogrin, Erick O. Burgos-Parra, Nicholas Bukin, Angus Laurenson, Horia Popescu, Marijan Beg, Ondrej Hovorka, Hans Fangohr, Paul A. Midgley, Geetha Balakrishnan, and Peter D. Hatton. Do Images of Biskyrmions Show Type-II Bubbles? *Advanced Materials*, 31(16):1806598, April 2019. ISSN 0935-9648, 1521-4095. doi: 10.1002/adma.201806598.

[66] A.H. Bobeck, P.I. Bonyhard, and J.E. Geusic. Magnetic bubbles—An emerging new memory technology. *Proceedings of the IEEE*, 63(8):1176–1195, 1975. ISSN 0018-9219. doi: 10.1109/PROC.1975.9912.

[67] Tim Titze, Sabri Koraltan, Mailin Matthies, Timo Schmidt, Dieter Suess, Manfred Albrecht, Stefan Mathias, and Daniel Steil. Pathways to bubble and skyrmion lattice formation in Fe/Gd multilayers. *Physical Review B*, 112(6): 064413, August 2025. ISSN 2469-9950, 2469-9969. doi: 10.1103/wgrf-cw1t.

[68] Xiaoye Chen, Edwin Chue, Jian Feng Kong, Hui Ru Tan, Hang Khume Tan, and Anjan Soumyanarayanan. Thermal Evolution of Skyrmion Formation Mechanism in Chiral Multilayer Films. *Physical Review Applied*, 17(4):044039, April 2022. ISSN 2331-7019. doi: 10.1103/PhysRevApplied.17.044039.

[69] Xiuzhen Yu, Maxim Mostovoy, Yusuke Tokunaga, Weizhu Zhang, Koji Kimoto, Yoshio Matsui, Yoshio Kaneko, Naoto Nagaosa, and Yoshinori Tokura. Magnetic stripes and skyrmions with helicity reversals. *Proceedings of the*

National Academy of Sciences, 109(23):8856–8860, June 2012. ISSN 0027-8424, 1091-6490. doi: 10.1073/pnas.1118496109.

[70] Cheng-Jie Wang, Pengfei Wang, Yan Zhou, Wenhong Wang, Fazhan Shi, and Jiangfeng Du. Formation of magnetic biskyrmions mediated by an intrinsic emergent monopole-antimonopole pair. *npj Quantum Materials*, 7(1):78, August 2022. ISSN 2397-4648. doi: 10.1038/s41535-022-00486-y.

[71] Lingyao Kong, Jin Tang, Weiwei Wang, Yaodong Wu, Jialiang Jiang, Yihao Wang, Junbo Li, Yimin Xiong, Mingliang Tian, and Haifeng Du. Observation of hybrid magnetic skyrmion bubbles in Fe 3 Sn 2 nanodisks. *Physical Review B*, 107(17):174425, May 2023. ISSN 2469-9950, 2469-9969. doi: 10.1103/PhysRevB.107.174425.

[72] lxfhfut. Multi-scale ridge detector. `https://github.com/lxfhfut/ridge-detector`, 2024. Python implementation of a multi-scale ridge detector for curvilinear structures.

[73] Carsten Steger. An unbiased detector of curvilinear structures. *IEEE Transactions on Pattern Analysis and Machine Intelligence*, 20(2):113–125, 1998. doi: 10.1109/34.659930.

[74] Shawn D. Pollard, Joseph A. Garlow, Jiawei Yu, Zhen Wang, Yimei Zhu, and Hyunsoo Yang. Observation of stable Néel skyrmions in cobalt/palladium multilayers with Lorentz transmission electron microscopy. *Nature Communications*, 8(1):14761, March 2017. ISSN 2041-1723. doi: 10.1038/ncomms14761.

[75] H. B. Mann and D. R. Whitney. On a test of whether one of two random variables is stochastically larger than the other. *The Annals of Mathematical Statistics*, 18(1):50–60, 1947. doi: 10.1214/aoms/1177730491.

[76] Yoav Benjamini and Yosef Hochberg. Controlling the False Discovery Rate: A Practical and Powerful Approach to Multiple Testing. *Journal of the Royal Statistical Society Series B: Statistical Methodology*, 57(1):289–300, January 1995. ISSN 1369-7412, 1467-9868. doi: 10.1111/j.2517-6161.1995.tb02031.x.

[77] Gábor J. Székely and Maria L. Rizzo. Energy statistics: A class of statistics based on distances. *Journal of Statistical Planning and Inference*, 143(8):1249–1272, 2013. doi: 10.1016/j.jspi.2013.03.018.

[78] S. Zhang, A. K. Petford-Long, and C. Phatak. Creation of artificial skyrmions and antiskyrmions by anisotropy engineering. *Scientific Reports*, 6(1):31248, August 2016. ISSN 2045-2322. doi: 10.1038/srep31248.

[79] Daniel Wolf, Nicolas Biziere, Sebastian Sturm, David Reyes, Travis Wade, Tore Niermann, Jonas Krehl, Benedicte Warot-Fonrose, Bernd Büchner, Etienne Snoeck, Christophe Gatel, and Axel Lubk. Holographic vector field electron tomography of three-dimensional nanomagnets. *Communications Physics*, 2(1): 87, December 2019. ISSN 2399-3650. doi: 10.1038/s42005-019-0187-8.

[80] Daniel Wolf, Sebastian Schneider, Ulrich K. Rößler, András Kovács, Marcus Schmidt, Rafal E. Dunin-Borkowski, Bernd Büchner, Bernd Rellinghaus, and Axel Lubk. Unveiling the three-dimensional magnetic texture of skyrmion tubes. *Nature Nanotechnology*, December 2021. ISSN 1748-3387, 1748-3395. doi: 10.1038/s41565-021-01031-x.